On the morphological and kinematic intelligence in insect flapping flights

昆虫羽ばたき飛行の形態学・運動学インテリジェンスについて

August 2021

RU XU

Graduate School of Science and Engineering

CHIBA UNIVERSITY

(千葉大学審査学位論文)

On the morphological and kinematic intelligence in insect flapping flights

昆虫羽ばたき飛行の形態学・運動学インテリジェンスについて

August 2021

RU XU

Graduate School of Science and Engineering

CHIBA UNIVERSITY

Acknowledgements

Upon the completion of this thesis, I am grateful for those who have offered me encouragements and support during my Ph.D. course.

First and foremost, I would like to give my sincere gratitude to my supervisor Prof. Hao Liu. His profound insight and constant encouragements light up my way throughout my entire Ph.D. study. The chances he offered me to present my work and communicate with other researchers in international conferences contribute to my passion on research. His life attitude and great foresight would have everlasting impact on my life.

I would also give special thanks to Dr. Toshiyuki Nakata and Dr. Dmitry Kolomenskiy. Their dedication to work and the willingness to share impressed me a great deal. Dr. Toshiyuki Nakata taught me to do experiments step-by-step, and he always have wonderful ideas when I encounter an obstacle. Every insightful talk with Dr. Dmitry Kolomenskiy helped me to have deeper understanding of the research.

I appreciate the constant help of our lab secretary Tamiko Kanke in Chiba University and Jing Fang in Shanghai Jiao Tong University. And I am also grateful for having such excellent lab members. The former lab members Dr. Gen Li, Dr. Ryutsuke Noda, Dr. Di Chen, Dr. Takashi Fujiwara gave me much advice and help in research. And I would like to thank my former collaborator Xiangdong Zhang for his contribution to the thesis. Thanks to the help of the insect group students, I would not have finished any insect experiments without them. And many thanks to Xuefei Cai, Yujing Xue, Ruichen Li and Jiaxin Rong, the encouragements from you guys and the time together support me through the trough and make the life enjoyable.

I gratefully acknowledge the financial support by Japanese Government Monbukagakusho Scholarship Council.

Lastly, thanks to my family and my boyfriend for their constant care support and encouragements.

2021,

Ru Xu.

ON THE MORPHOLOGICAL AND KINEMATIC INTELLIGENCE IN INSECT FLAPPING FLIGHTS

ABSTRACT

Flying insects benefit much from their morphological and kinematic intelligence. Bio-flyers of insects, birds and bat are observed to have a broad range of wing-to-body mass ratio (WBMR), which can lead to large inertial forces and torques in fast-flapping wings, particularly in insect flights, comparable with or even greater than aerodynamic ones. We first carried out a simulation-based study of the WBMR effects on insect flapping flights with a specific focus on unraveling whether some optimal WBMR exists in balancing the flapping aerodynamics and body control in terms of body pitch oscillation and power consumption. We found that the realistic WBMRs in the three insect models can suppress the body pitch oscillation to a minimized level at a very low cost of mechanical power. Our results indicate that the WBMR plays a crucial role in optimization of flapping-wing dynamics, which may be useful as novel morphological intelligence for the biomimetic design of insect- and bird-sized flapping micro aerial vehicles. We further tackled a problem that intermittent control strategy may play a crucial role in enhancing stabilization robustness in bumblebees to stay aloft under complex natural environment. It is uncovered that the intermittent control model can achieve an angular-dominant flight control whereas the continuous control model corresponds to an angular-velocity-dominant one. Given the biological constraints in sensorimotor neurobiology and musculoskeletal mechanics, the intermittent control strategy was examined capable of enhancing the stabilization robustness in terms of sensory latency, stroke derivation, spike interval, and damping strength. Moreover, we investigated

takeoff control behaviors in green chafer and found that the insect can conduct vertical takeoff efficiently in a roll dominant way; the roll can not only orient the flight direction of target but also provide a smooth transition between the backward flight and forward flight.

KEY WORDS: Insect flight, Wing-to-Body-Mass-Ratio, Intermittent control, Takeoff flight, Aerodynamics, Stability

Contents

List of Figures

List of Tables

Chapter 1 General Introduction

This chapter introduces the general background, motivations, aims and outlines of current research.

1.1 Background

Insect flight has fascinated researchers for years due to their high maneuverability in spite of the simple wing structure. Both the kinematics and morphology of insects have long evolved to adapt to the complex environment and stabilize the flapping flight in smart ways[1-2]. They take advantage of the small body scale and high intelligent wing kinematics to perform evasive maneuvers in cluttered environment[3-5]. Even subtle change in wing kinematic can lead to bank turn of a fruit fly[6] and evasive maneuver of hummingbird[7-8]. Among the kinematic intelligence of insect flapping flight, the use of leading-edge-vortex is one of the most prominent. Insect flaps efficiently with high angle of attack which separates the flow at the leading edge and reattaches before the trailing edge, leading to a formation of a stable vortex attached to wing due to the balance of centripetal and Coriolis accelerations[9-10]. It is intriguing how insect manage to coordinate the body and wing kinematics in complex environment for stabilization and maneuver which induced plenty of studies focusing on the inner nervous and outer musculoskeletal systems[1, 8, 11-14].

1.1.1 Insect flight muscles

Wing motion is actuated by flight muscles which can be categorized into two groups, one is called the power muscles(indirect flight muscles) which takes up a large portion of thorax volume and oscillate the thorax to induce flapping motion, the other group locate near the wing hinge called steering muscles(direct flight muscles) to modulate the detailed wing kinematics cycle by cycle[11-12, 15]. The power muscles can be synchronous or asynchronous in different species. Synchronous muscle indicates a one to one correspondence between neuron spike and muscle contraction such as the power muscle of locust and hawkmoth, while asynchronous points to multiple muscle twitch after single neuron spike such as the power muscle of bumblebee and beetles[15].

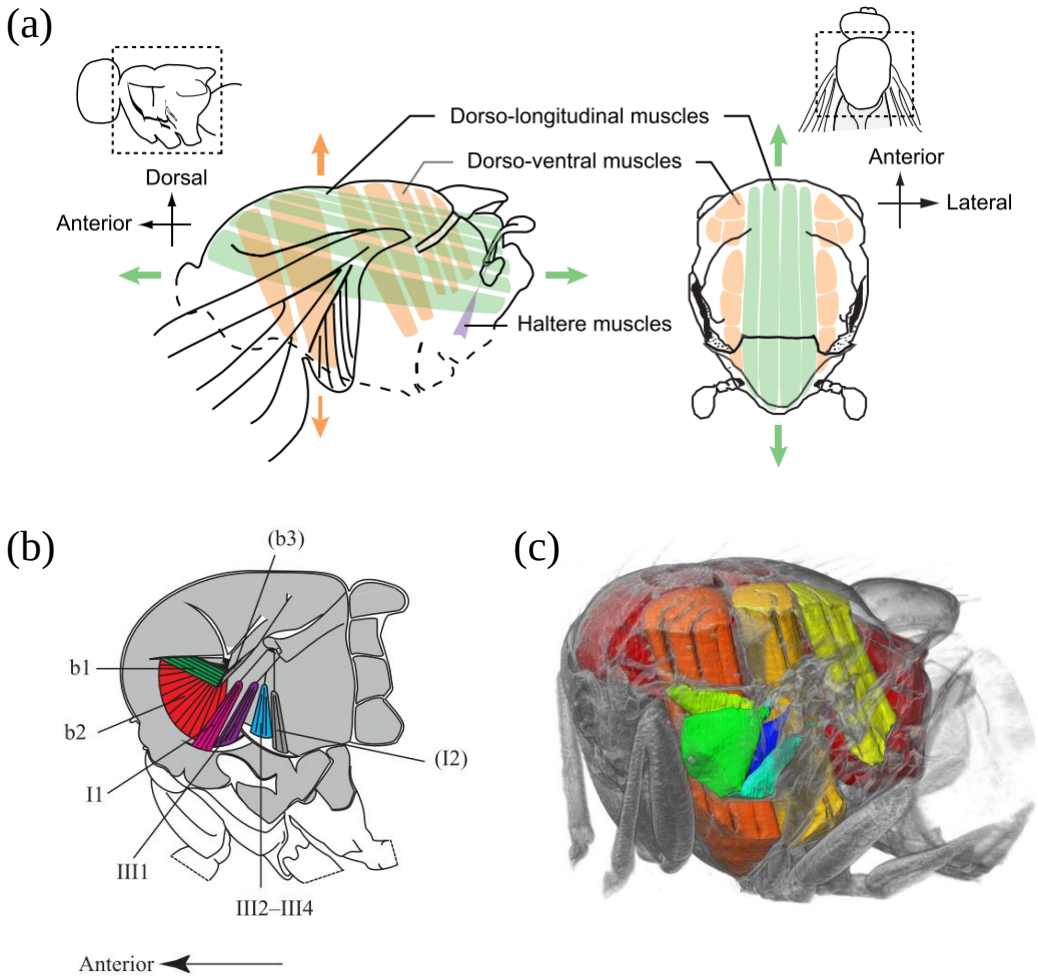

Figure 1–1 (a)The indirect flight muscles Dorsal-Ventral-Muscle and Dorsal-Longitudinal-Muscle groups, adapted from[15]. (b)The direct flight muscles in wing hinge, adapted from[11]. (c) The cutaway visualization of the combined two muscle groups, figure adapted from Simon Walker et. al.[16]

The indirect flight muscles include the dorsal-ventral muscles and dorsol-logitudinal muscles as shown in Figure 1–1. The dorsal-ventral muscle contraction leads to wing elevation while the contraction of dorsal-longitudinal muscle leads to wing depression. The indirect flight muscles mainly control the flapping frequency while the frequency does not deviate much from the resonance frequency of the thorax wing system[17-18]. The electromyographic signals can be recorded and simultaneously filming the corresponding

wing motion to clarify the muscle activity relation with wing kinematics. It is found that the activation frequency of basalare muscle b1 is almost at wingbeat frequency showing the possible necessity for maintaining the wing stroke amplitude[11-12]. And b2 is correlated with similar wing kinematic alteration where the effect of both b1 and b2 muscles decays quickly within a single wingbeat[11-12], consistent with the synchronous muscle characteristic. However, the correlation between each muscle spike and wing kinematics is not thoroughly known since multiple muscles may be spiked at the same instant which makes it complicated to decouple the effects[11-12].

1.1.2 Insect sensory system

Insect can perform excellent maneuver in complex environments, which owes much credit to the acute sensory system. The sensory input of insects is composed of visual, odor, sound, and mechanosensory sensing from compound eyes and/or ocellus[19-20], antennae[21], haltere[19] and even mechanosensory hairs[22-23]. Bumblebee can even navigate in complete darkness and in the absence of odor which may give some hint for a internal magnetic compass[20]. Therefore, the information of current body posture, body translational velocity as well as angular velocities can be obtained as the feedback information which can be applied for control. Whereas, the sensory delay is disastrous for the flight performance.The sensory delay is composed of the afferent and efferent delays. The sensory delay of visual feedback is substantially larger than that of mechanosensory information[24], and the sensory delay length are summarized in Table 1–1. Mechanosensory delay is estimated to be around 0.5 wingbeat cycles, while the visual feedback is longer, around $2 \sim 5$ wingbeat cycles. There exist a fundamental trade-off between the permissible control gain and the sensory delay length according to the research on *Drosophila* yaw control[25]. For insects like fruit flies, the underlying limiting factor of manuverbility is neural delays, while hummingbird is also affected by the muscle mechanical power other than neural delay[26].

1.1.3 Flapping-wing Micro-Air-Vehicle

Micro-air-vehicle is one of the application fields that insect flight intelligence can be applied to. Nowadays, flapping wing MAVs posses the miniature size of insects or birds with certain maneuverability[35]. Early fMAVs possess larger size and poorer autonomy such as the Delfly at the scale of 33cm and the hummingbird inspired Nano Air

insect	delay length	reference
housefly (visual to motor)	$30ms$	Land, M. F.& Collett, T. S. (1974)[27]
fruit fly (visual)	$\sim 60ms$	Muijres et. al. (2014)[6]
fruit fly *Drosophila* (roll)	$4.6ms$	Tsevi Beatus et. al. (2015)[28]
fruit fly *Drosophila* (yaw)	$9.0 \sim 22.5ms$	Leif Ristroph et. al. (2009)[29]
fruit fly *Drosophila*(pitch)	$13ms$	Leif Ristroph et. al.(2013)[30]
hawkmoth *Manduca sexta* (pitch)	$\sim 51ms$	Bo Cheng et. al. (2011)[31]
hawkmoth *Manduca sexta* (pitch angular)	$\sim 17ms$	Bo Cheng et. al. (2011)[31]
hawkmoth *Manduca sexta* (gyroscopic sensor)	$< 10ms$	T. L. Hedrick et. al.[32]

Table 1–1 The sensory delay summarization

Vehicle (15cm) (Figure 1–2). Delfly has two set of wings which flaps antiphase and take advantage of clap-and-fling mechanism to augment aerodynamic force. The Robobee developed in 2013, is at scale of a few centimeters with total mass of 80mg powered by external power source[33]. The Robobee adopts high-power-density piezoelectric actuators as flight muscles which achieved stable hovering and even able to realize basic controlled flight maneuver. There are even fMAVs powered by soft artificial muscles(dielectric elastomer actuatora(DEAs)) in 2019 mimiking the actuation system of insects at scale of 20mm which is resilient to external impact due to the flexible actuation system[34] compared with the state-of-the-art fMAVs actuated by rigid actuators. While current DEAs model consumes 15 times more energy than piezoelectric actuator driven models which remains to be modified for future application.

Still, the main difficulties lies in miniaturization, developing high energy density power source as well as achieving high autonomous/controlled flight. To achieve desired flight state, the certain degrees of control design adds to the complexity of hinge design as well as the body weight. Meanwhile the feedback information required for the stabilization process is obtained by an off-board motion capture system.

1.2 Approaches to investigate insect flight

1.2.1 Insect experiments& kinematics reconstruction

To resolve the aerodynamic of a flapping wing insect, the body wing kinematics are the essential part of the fluid structure interaction. High speed cameras provide a perfect tool to capture the details of high flapping frequency insects. Tethering the insects or

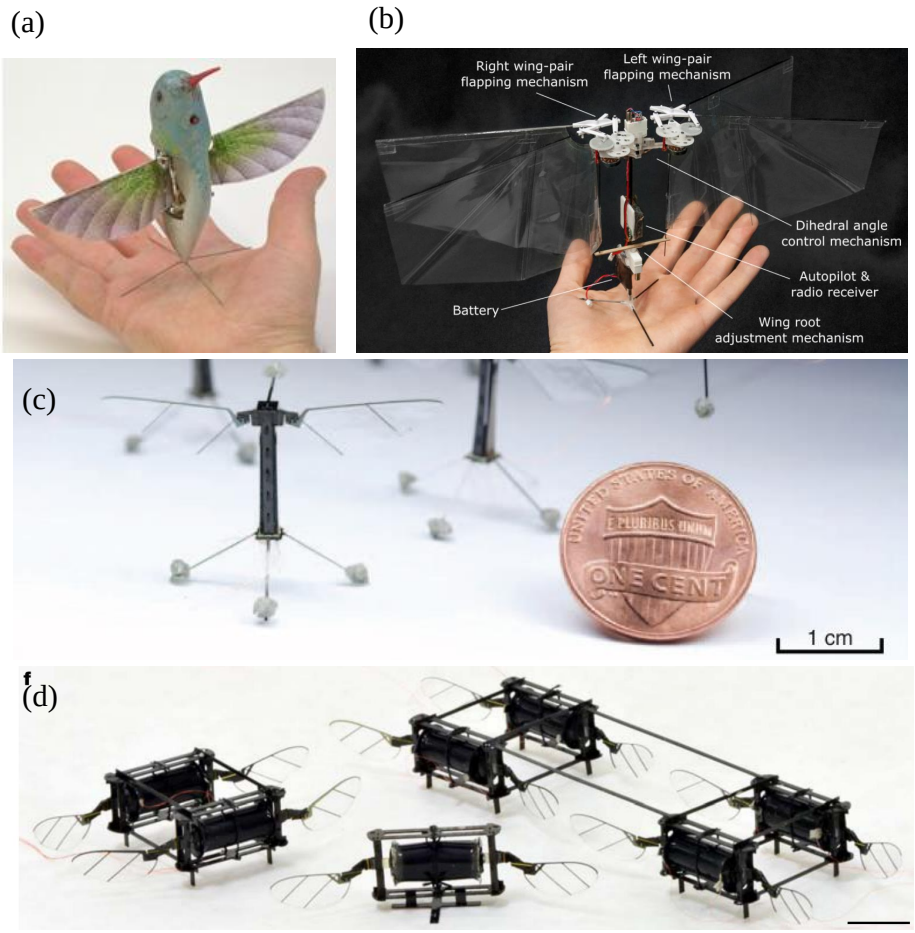

Figure 1–2 (a)hummingbird-inspired robotic Nano Air Vehicle (https://spectrum.ieee.org/automaton/robotics/military-robots/darpa-concludes-nano-air-vehicle-program-we-wonder-whats-next) (b) The Delfly model with onboard battery.(http://www.delfly.nl/?site=diii&menu=home&lang=en) (c) The Robobee[33] (d) Image of flapping-wing microrobots driven by DEA[34]

restrict some degrees of freedom can effectively contain the insect in camera view, which however hinders the insects from performing natural flights. Free flight is preferable with proper scent for foraging behavior[36-37] or sensory stimuli[28-29, 38].

The wing& body kinematics reconstruction involves substantial human work in digitizing. Auto-tracking based on multi-silhouette reconstruction (model-based hull reconstruction)[41-43] can extract the wing body kinematics, while the roll cannot be well resolved with axial symmetric body shape and this method requires a clean background. Hull reconstruction combined with artificial markers may help to determine the roll angle. Florescent markers are applied to the wing and body in housefly for automated visual

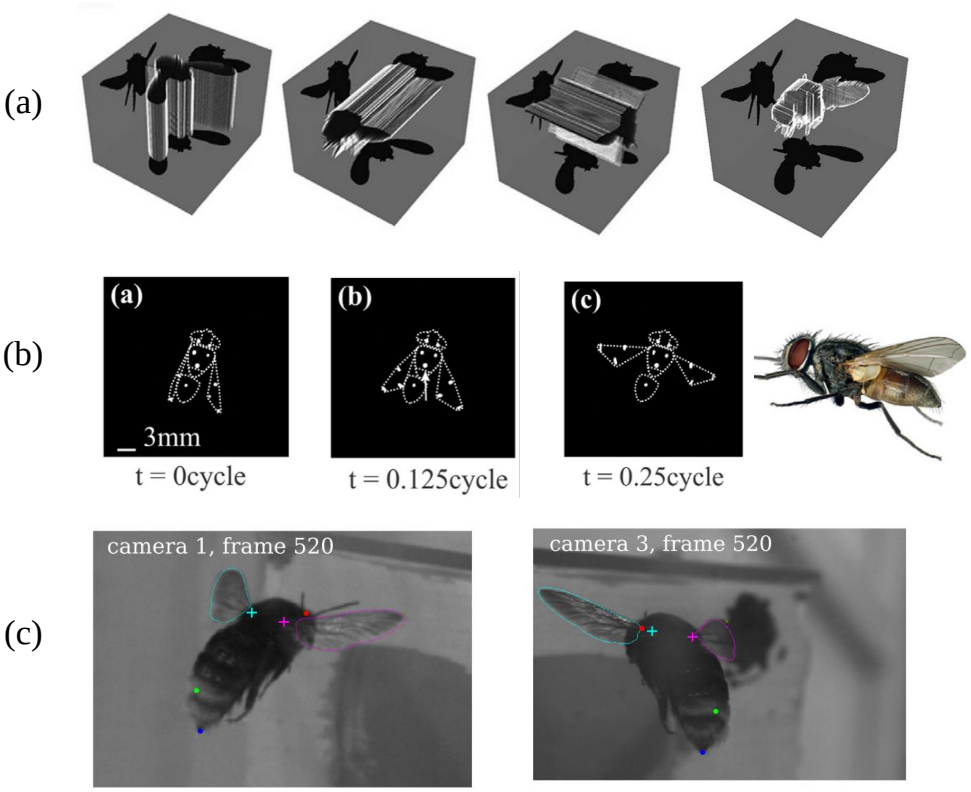

Figure 1–3 The insect kinematics reconstruction methods, figure adapted from[29, 39-40] (a) hull reconstruction from aligned sihouettes of a fruit fly (b)floresence marker based reconstruction of a house fly (c) shape fitting reconstruction of the bumblebee wing kinematics

tracking[40], but markers will inevitably lead to mass change for wing or body. The natural characteristic points can serve as markers during tracking such as the abdominal color bands on hawkmoth[44] and bumblebee[39]. Shape fitting adopted in the bumblebee free flight wing kinematics reconstruction[39] requires the shape to be known beforehand, but can obtain the wing kinematics without the requirement for many markers (Figure 1–3). Deep learning method based on a large training data-set is becoming a new trend for markerless pose recognition[45-46], and may be able to provide a large amount of data in short time.

1.2.2 The in-house flight solver

To quantify the aerodynamic force & torque generated during flapping flight, experiments have been done using model wings flapping in air/oil/water[47-48] with load cell at the wing hinge to measure the resultant torque or force[49-50]. Analytical methods provide a simplified tool to obtain the aerodynamic force/torque. The blade-element model is often applied in the aerodynamic force torque analysis with a quasi-steady assumption for simplification which only requires for the geometric shape and wing kinematics information and not time consuming. The aerodynamic force is mainly contributed by the wing translational, rotational, the coupling terms of translational and rotational motion, the added mass effect[47-48, 51]. Yet, the quasi-steady model cannot provide a straightforward impression of the flow structure.

Apart from quasi-steady model which can approximate the aerodynamic force & torques, CFD tools are often for direct illustration of the flow structure around wing and body, in this thesis, the solver we adopted is an in-house fluid solver developed by Liu[52-53]. The solver is a fortified Finite Volume Method-based Navier Stokes solver for dynamically moving multi-blocked, overset-grid systems which is developed and verified to be self-consistent by a variety of benchmark tests. The fluid solver is loosely coupled with the dynamic block with a 4^{th}-order Runge-Kutta scheme. The governing equations are in-compressible Navier-Stokes equation in strong conservation form for momentum and mass shown as Equation (1–1). And a pseudo time derivative of pressure is added in the continuity equation to introduce an artificial compressibility method. The t and τ are the physical time and pseudo time separately, u, v, w are the velocities in Cartisian coordinate system. p represents the pressure,

$$\int_{V(t)} (\frac{\partial \mathbf{Q}}{\partial t} + \frac{\partial \mathbf{q}}{\partial \tau}) dV + \int_{V(t)} (\frac{\partial \mathbf{F}}{\partial x} + \frac{\partial \mathbf{G}}{\partial y} + \frac{\partial \mathbf{H}}{\partial z} + \frac{\partial \mathbf{F}_v}{\partial x} + \frac{\partial \mathbf{G}_v}{\partial y} + \frac{\partial \mathbf{H}_v}{\partial z}) dV = 0 \qquad (1\text{–}1)$$

where

$$\mathbf{Q} = \begin{Bmatrix} u \\ v \\ w \\ 0 \end{Bmatrix}, \mathbf{q} = \begin{Bmatrix} u \\ v \\ w \\ q \end{Bmatrix}, \mathbf{F} = \begin{Bmatrix} u^2 + p \\ uv \\ uw \\ \lambda u \end{Bmatrix}, \mathbf{G} = \begin{Bmatrix} vu \\ v^2 + p \\ vw \\ \lambda v \end{Bmatrix}, \mathbf{H} = \begin{Bmatrix} wu \\ wv \\ w^2 + p \\ \lambda w \end{Bmatrix}$$

$$\mathbf{F}_v = -\frac{1}{Re}\begin{Bmatrix} 2u_x \\ u_y + v_x \\ u_z + w_x \\ 0 \end{Bmatrix}, \mathbf{G}_v = -\frac{1}{Re}\begin{Bmatrix} v_x + u_y \\ 2v_y \\ v_z + w_y \\ 0 \end{Bmatrix}, \mathbf{H}_v = -\frac{1}{Re}\begin{Bmatrix} w_x + u_z \\ w_y + v_z \\ 2w_z \\ 0 \end{Bmatrix}$$

By introducing the generalized Reynolds transport theorem, and employ the Gaussian integration theorem, the integration form of the former Equation 1–1 can be obtained as Equation (1–2) in general curvilinear coordinate system as:

$$\int_{V(t)} \frac{\partial \mathbf{q}}{\partial \tau} dV + \frac{\partial}{\partial t}\int_{V(t)} \mathbf{Q} dV + \oint_{S(t)} (\mathbf{f} - \mathbf{Q}\mathbf{u}_g) \cdot \mathbf{n} dS = 0 \tag{1–2}$$

here $\mathbf{f} = (\mathbf{F} + \mathbf{F}_v), \mathbf{G} + \mathbf{G}_v, \mathbf{H} + \mathbf{H}_v))$, and the $S(t)$ is the surface of the control volume $V(t)$,$\mathbf{n} = (n_x, n_y, n_z)$ denotes the normal vector perpendicular to the surface of control volume, and $\mathbf{u}_g$ is the local velocity of the moving cell surface.

The boundary condition on the inner grid of body surface is the no-slip condition for velocity components, and the inflow condition specifies the inflow velocity and zero pressure while at the downstream, zero gradient condition is chosen for both velocity and pressure.

1.3 Motive and aim

Bio-flyers of insects, birds, and bats are observed to have a broad range of wing-to-body mass ratio (WBMR) from 0.1% to 15%. The WBMR and wing mass distribution can lead to large inertial forces and torques in fast-flapping wings, particularly in insect flights, comparable with or even greater than aerodynamic ones, which may greatly affect the aerodynamic performance, flight stability, and control, but still remain poorly understood.

On the other hand, active flight control plays a crucial role in stabilizing the body posture of insects to stay aloft under a complex natural environment. Insects can achieve a closed-loop flight control by integrating the external mechanical system and the internal working system through manipulating wing kinematics according to feedback information from multiple sensors. While studies of proportional derivative/proportional integral derivative-based algorithms are the main subject to explore the continuous flight control mechanisms associated with insect flights, it is normally observed that insects achieve an intermittent spike firing in steering muscles to manipulate wings in flight control discontinuously. Whether muscle spiking pattern posses some kinematic intelligence or disrupt the stabilization robustness remains to be unveiled. Active control is able to stabilize

flight and maneuver to a desired position/state such as the beetle voluntary takeoff maneuver. It is found that green chafer is capable of conducting swift vertical takeoff flight which is seldomly investigated. Whether there exist some smart takeoff strategies or not is quite worthwhile to explore.

1.4 Thesis outline

Chapter 1 gives a brief introduction of the research background and the general research methods for analyzing insect flight behavior and the author's motivation of this work.

Chapter 2 focus on the morphological intelligence of insect wings especially regarding the wing inertia effect based on a simulation results. The wing-to-body-mass-ratio's effect on aerodynamic force torque as well as the power expenditure are examined with three insect models ranging

Chapter 3 and 4 focus on the kinematic intelligence of insect control. Chapter 3 introduces a novel intermittent control mechanism for pitch stabilization of bumblebee model based on insect biological constraint, and compare the intermittent model with conventional continuous Proportional Derivative control model to investigate the stabilization robustness. Chapter 4 examined the voluntary takeoff kinematic behavior of beetles based on experimental results, and carried out simulation comparison for an in-depth understanding of the kinematic intelligence of the flight sequences.

Chapter 2 The morphological intelligence of insects Wing-to-Body Mass Ratio

2.1 Introduction

Aerobatic animals varies in size from millimeter scale of thrips to meter scale of birds as well as the body & wing mass. From Figure 2–1, it can be found that there exist an obvious trend of decreasing in wing beat frequency with the increase of wing-body-mass-ratio (WBMR) which is defined as the ratio of wing pair mass and total mass ($\varepsilon = \frac{m_w}{m_t}$). And the decreasing rate is in log scale, indicating a significant decrease in wing beat frequency for high WBMR. One possible explanation is that limited power output from the muscles within thorax/hinge restrains the allowable wing mass under high flapping frequency, and vice the versa, i.e. $P \sim f^2\varepsilon$. However, the actual muscle power depends on the amount of muscle and the corresponding body scale, what determines the WBMR is not yet very clear. Furthermore, whether the realistic WBMR is an optimal choice or not is unknown yet. Wing mass not only affects the power consumption during

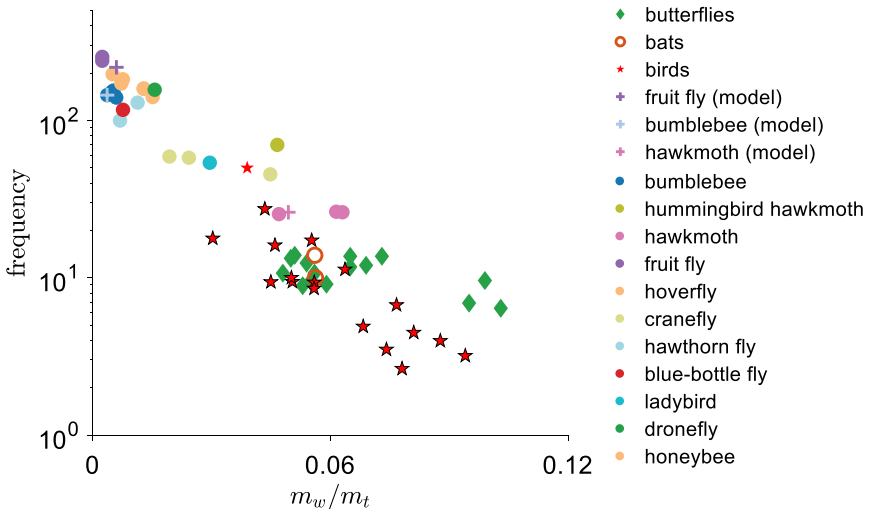

Figure 2–1 The relationship between WBMR and frequency for different species. The data are obtained from[2, 54-59], and summarized in Table A–1 in supplementary material. Note the logarithmic scale in frequency axis.

flapping, but also determines the body dynamics. High WBMR in butterfly dominants

the body oscillation in flight, leading to a change of 30 degrees in each wing beat cycle in *Kallima inachus*[60] with $\varepsilon = 7\%$, while this oscillation is proved to be beneficial for thrust generation during flight. Suzuki et. al.[61] also proved that WBMR has a dominant effect on the body pitch oscillation, but they pointed out that the WBMR and aerodynamic performance is inversely correlated.

Moreover, the mass increase of the wing is accompanied with the increase of body mass (body scale) (Figure A–1), which is mainly due to the requirement of larger wing loading[62] hence larger wing stiffness. Birds& bats wings contains feather or skeleton structure to increase the wing stiffness to support heavy body, while insects developed smart vein structures to elevate the wing stiffness without increasing too much of the wing mass[63] to avoid large inertial power consumption. And the micro-fluid[64] within veins helps enhancing the vein stiffness. Wing stiffness and wing loading(comprised of inertial loading as well as aerodynamic loading) dominant the wing deformation. And wing deformation has an important effect in the aerodynamic force generation where favorable wing deformation can elevate the aerodynamic efficiency according to the two-dimensional analysis of Yin et.al.[65] and the three-dimensional analysis on haw moth[66].

Table 2–1 The morphological parameters and kinematic parameters of three insect models.

Species	$c_m(mm)$	$R(mm)$	$f(Hz)$	$\Phi(^\circ)$	Re	$\xi(^\circ)$	$\beta(^\circ)$	$\varepsilon(\%)$
Fruit fly	0.78	2.39	218	140	134	45	0	0.60
Bumblebee	4.10	15.0	145.1	139.4	1617	45	0	0.36
Hawkmoth	18.3	48.3	26.1	114.6	6300	40	15	4.94

Wing mass affects both the aerodynamics and body dynamics, large wing inertial force/torque may lead to imbalance in between, while trade-off should be resolved through the long evolution of insects. Thus in this study, we investigated three types of insects: fruit fly, bumblebee, hawkmoth, studied the WBMR effect on aerodynamics and body dynamics. And further derived a scaling law correlating the wing dynamics with the WBMR, which provides a discipline for the designing of fMAVs(flapping Micro-Air-Vehicles).

2.2 Methods

2.2.1 Three insect models

Three insect models are adopted from previous researches: fruit fly(*Drosophila melanogaster*), bumblebee(*Bombus ignitus*), hawkmoth(*Agrius convolvuli*), with Reynolds number ranging from hundreds in fruit fly to thousands in hawkmoth. Moreover, the WBMR covers a broad range from 0.3% to 5%. The geometric and wing kinematic models are established as in Figure 2–3. The morphological parameters of three insect models are listed in Table 2–1, Table 2–2 and Table 2–3.

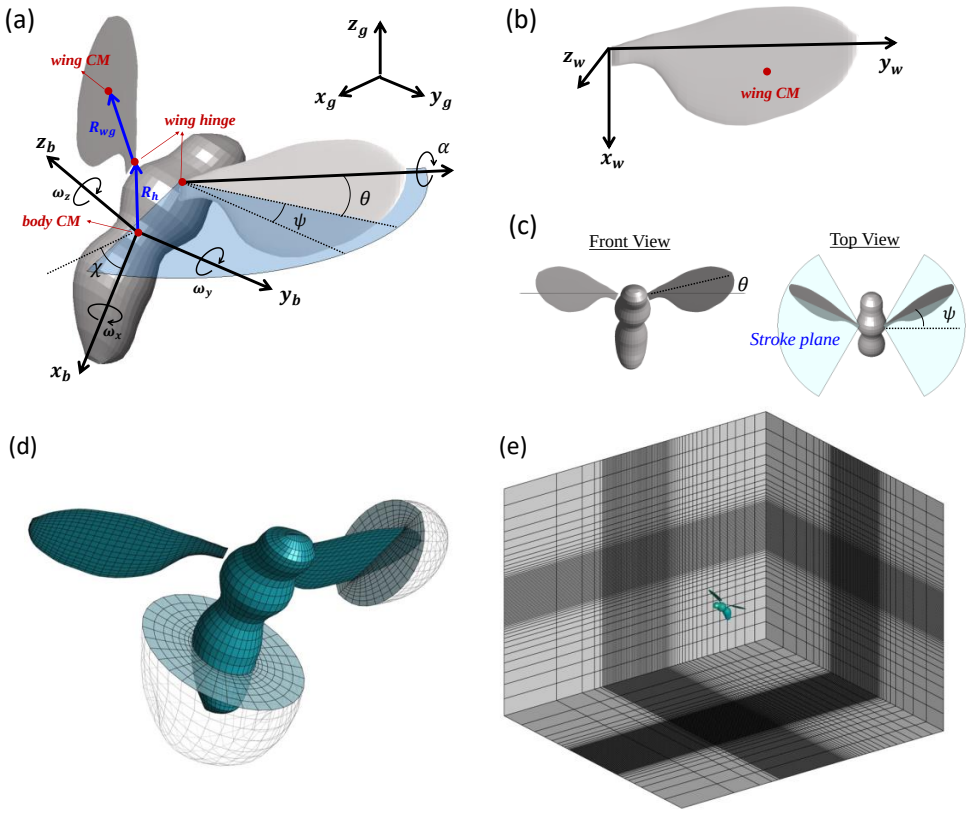

Figure 2–2 (a)The ground frame coordinates $x_g y_g z_g$ and the body-fixed coordinates $x_b y_b z_b$. The vector from body CM to wing pivot is defined as $\vec{R}_h$, and the vector from wing pivot to wing CM is defined as $\vec{R}_{wg}$ (b)The wing fitted coordinates $x_w y_w z_w$. (c) Wing kinematics is defined by three angles: ψ (the sweeping angle in stroke plane), θ the wing elevation from the stroke plane, α the wing feathering around y_w axis. (d-e)The wing/body fitted grid and the background grid

The geometric model of three insects are established by extracting the real shape of body and wing[66-68]. And the wing kinematic models are obtained from Liu et.al.[2].

Three angles are used to describe the wing kinematics as illustrated in Figure 2–2(a)(c), the details of the kinematics are shown in Figure 2–3 (d-f) where the ψ represents the wing sweeping angle around the x_b axis, θ is the wing elevation (around z_w axis) and α is the wing rotation around y_w axis. The three angles are defined relative to the stroke plane(SP) which is constituted by the wingtip trajectory during a full cycle. The stroke plane angles (SPA) for bumblebee and fruit fly are 0°[39, 68] and 15° in hawkmoth[2]. To obtain the vector from the body CM to wing pivot, a uniform density distribution is applied for insect bodies, and the corresponding $\vec{R}_h$ are listed in Table 2–2. And the CM of insect wings are also calculated by assuming uniform density distribution. However, it is known that due to the nonuniform vein distribution of insect wings[69], the majority of wing mass centers around the wing base, therefore resulting in smaller $\vec{R}_{wg}$ and MoI (I^{wing}) around wing pivot compared with uniform assumption. To see how much difference the uniform assumption may cause, two wing models are compared labeled as bumblebee[1] representing wing with actual distribution and bumblebee[2] (Table 2–3) representing uniform distribution. The effect of wing mass distribution is compared in result section.

Table 2–2 The position vector, moment of inertia and mass of insect bodies

Species	$m_b(mg)$	$R_{hx}(mm)$	$R_{hy}(mm)$	$R_{hz}(mm)$	$I_{yy}^{body}(mgmm^2)$
Fruit fly	0.96	-0.482	-0.362	0.4	0.488
Bumblebee	416.5	-6.50	2.96	2.76	14192
Hawkmoth	1540	-15.3	-6.6	6.82	4.54×10^5

Table 2–3 The position vector, moment of inertia and mass of insect wings Here the superscript [1], [2] represents the wing with actual mass distribution and with uniform mass distribution respectively.

Species	Fruit fly	Bumblebee[1]	Bumblebee[2]	Hawkmoth
$m_w(mg)$	2.88×10^{-3}	0.759	0.759	40
$R_{wx}(mm)$	0.059	0.287	1.072	2.792
$R_{wy}(mm)$	1.39	5.723	7.793	23.2
$I_{xx}^{wing}(mgmm^2)$	6.54×10^{-3}	33.442	56.05	28 741
$I_{yy}^{wing}(mgmm^2)$	2.5×10^{-4}	1.099	2.468	1916
$I_{zz}^{wing}(mgmm^2)$	6.79×10^{-3}	34.541	58.516	30657
$I_{xy}^{wing}(mgmm^2)$	1.96×10^{-4}	0.785	5.601	1490

It should be notified that insects possess thin wings (less than 5 percent of the mean

chord length). The wing mass ratio of bumblebee is 0.36% from measurement[69], and the wing thickness is $1\%c_m$ according to Kolomenskiy et. al[69]. that the vein thickness of bumblebee ranges from $0.4\% \sim 2.7\%c_m$. As described by Usherwood et al.[70] that the hawkmoth wing thickness is normally less than $1.6\%c_m$, thus it is assumed to be $1.4\%c_m$ in our model. The wing thickness of fruit fly is $0.8\%c_m$, which is thicker than the experimental value $0.17\%c_m$, but it is proved by an extra case validation in supplementary material (Figure A–2 and Figure A–3) that a slightly thicker fruit fly wing have negligible effect on the aerodynamic performance.

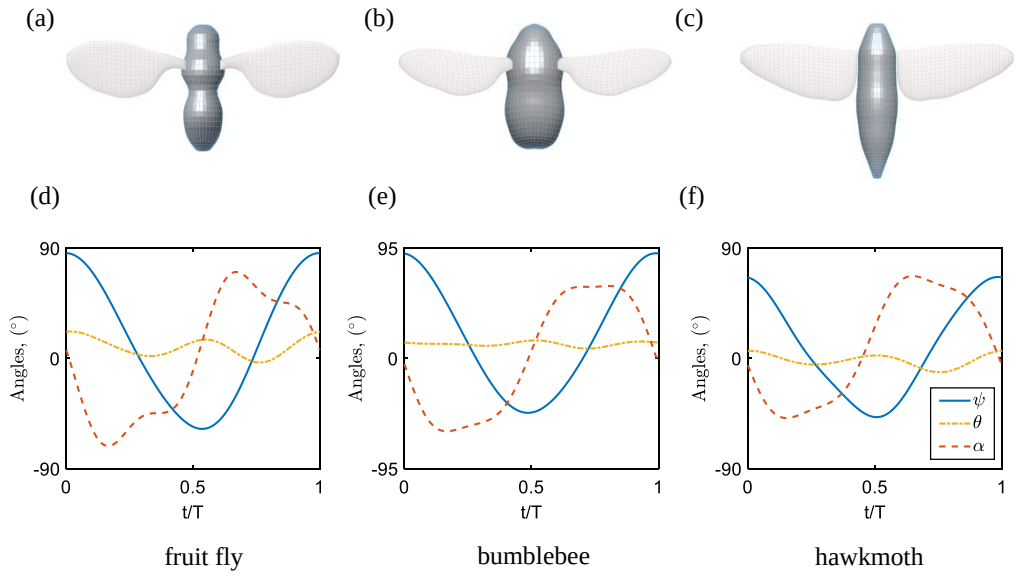

Figure 2–3 (a-c)The geometric models of fruit fly, bumblebee, hawkmoth separately. (d-f)The wing kinematics of three insects, with blue-solid line, red-dashed line, yellow-dotted dash representing wing stroke angle ψ, wing rotation angle α and wing elevation angle θ respectively.

2.2.2 The dynamic equations

Due to the symmetric flapping wings, the body dynamic equation can be simplified to 3DoFs, with body translation degree of freedom (v_x, v_z), and body rotation around y_b axis (ω_b). Different from the traditional studies that averaged the wing inertia effect or ignored the wing inertia[71], our study take into consideration the wing inertia and the

equation is shown as bellow (Equation 2–1):

$$m_b \frac{d\vec{v}_b^{CM}}{dt} + m_b \vec{\omega}_b \times \vec{v}_b^{CM} + \vec{a}_1 + \vec{b}_1 = \vec{F}_a + m_t \vec{g} \tag{2–1a}$$

$$\vec{\omega}_b \times I_b \vec{\omega}_b + I_{yy}^{body} \frac{d\vec{\omega}_b}{dt} + \vec{a}_2 + \vec{b}_2 = \vec{M}_a \tag{2–1b}$$

The $\vec{v}_b^{CM}$ represents the body CM velocity in body frame, and $\vec{\omega}_b$ is the body pitch angular velocity. $\vec{F}_a$ and $\vec{M}_a$ represent the total aerodynamic force and torque respectively. The terms $\vec{a}_1$, $\vec{a}_2$, $\vec{b}_1$, $\vec{b}_2$ includes the terms caused by wing inertia effect and the coupling term between the wing and body motion. Detailed expression can be found in Sun[71]. Since we only consider 3DoFs system, the Equation 2–1 can be simplified to the Equation 2–2, thus can be solved through 4^{th} order Runge-Kutta method at each physical time step.

$$\mathbf{A} \begin{bmatrix} \frac{dv_x}{dt} \\ \frac{dv_z}{dt} \\ \frac{d\omega_y}{dt} \end{bmatrix} = \mathbf{B} \tag{2–2}$$

2.3 Results & Discussion

2.3.1 Trim hovering flight

Before laying eyes on the wing inertia effect, it is necessary to achieve a trimmed hovering state for all three models. Thus $\bar{F}_x$ and $\bar{T}_y$ should be minor compared with the body weight and reference torque, while $\bar{F}_z$ should be comparable to body weight to achieve a force balance. Though body is assumed to have uniform density distribution, it is not necessarily able to meet the torque balance requirement. Thus we slightly shift the CM position along body axis to achieve torque balance.

A representative trimmed hovering state of bumblebee is illustrated in Figure 2–4. And it can be seen that the body translation velocities & body angular velocity changed very little during three wing beat cycles, indicating a stable hovering state.

2.3.2 The WBMR effect on body dynamics

To study the WBMR effect on the aerodynamics and body dynamics, the wing mass ratio is changed from 0 to twice the original ratio (ε_r) with an interval of $0.5\varepsilon_r$, while keeping the total mass m_t unchanged. The oscillation amplitude of velocity and angular velocity are calculated and plotted for three species in Figure 2–5.

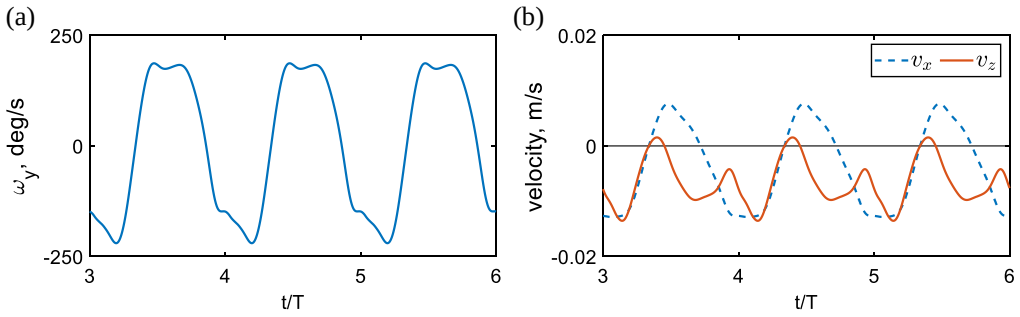

Figure 2–4 Time courses of body motion in trimmed hovering of bumblebee with zero-wing mass (from third to sixth strokes): (a) angular velocity xy and (b) velocities v_x, v_y,and v_z.

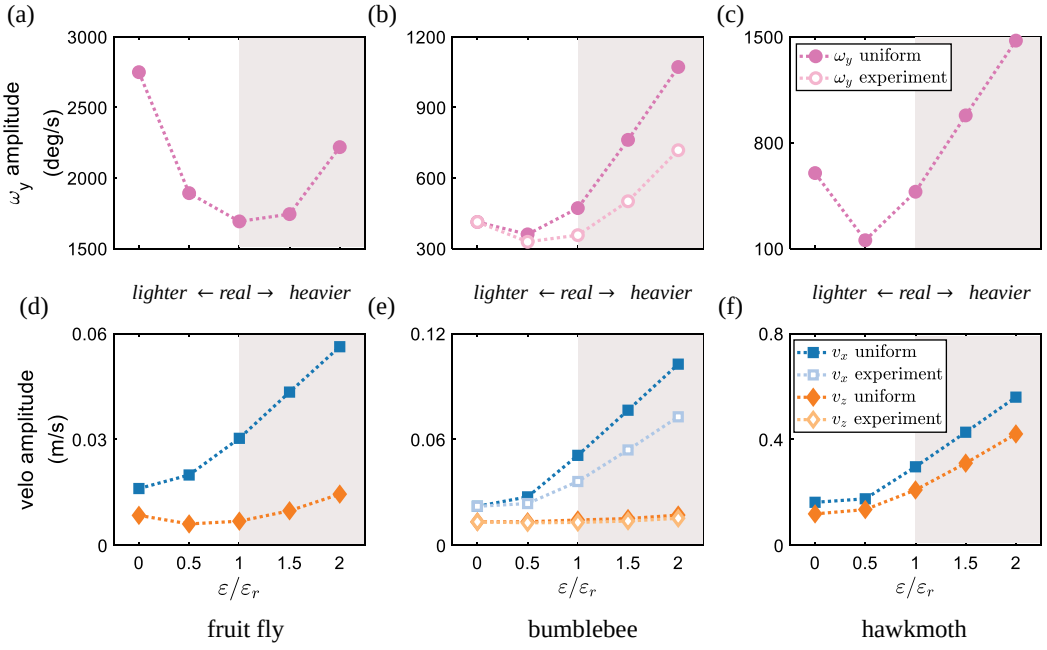

Figure 2–5 Oscillation amplitude of body pitch (angular velocity ω_y) and velocity (v_x, v_z) vs wing-to-body mass ratio $\varepsilon/\varepsilon_r$ in hovering flights: [(a) and (d)] fruit fly, [(b) and (e)] bumblebee, and [(c) and (f)] hawkmoth. Filled symbols: wings with uniform mass distribution; unfilled symbols: the wing with realistic mass distribution.

It can be found in Figure 2–5 that the angular velocity oscillation amplitude exist an optimum around the actual wing mass point($\varepsilon/\varepsilon_r = 1$), while the oscillation amplitude of translation velocity seems to increase monotonically. Though for bumblebee and/or hawkmoth, the optimum doesn't locate exactly at ε_r, but it locates very close to the realistic value. Especially for bumblebee model with realistic wing mass distribution, the optimum shifts towards the ε_r compared with uniform wing mass distribution case. From the two mass distribution cases in bumblebee, we can find that the uniform wing mass distribution wouldn't affect the body dynamic results very significantly. It should be notified that the significant decrease in pitch angular velocity when WBMR is close to realistic value, even compared with zero-wing-mass cases indicates that the insects can hover with a stabilized vision, which should be important for control with mechanosensory /visual feedback information since pitch oscillation will induce certain noise to the feedback information.

Although it is known that realistic WBMR seems to be beneficial for body pitch dynamics from previous result, what caused this phenomenon requires further analysis regarding the torque. The total torque that causes body rotation is composed of two parts: the inertial torque as well as the aerodynamic torque during flapping. The transient aerodynamic torque and inertial torque of three insects in one cycle are plotted in Figure 2–6. It can be seen that, for the majority of the time, the aerodynamic torque (blue-dash dot-line) is in anti-phase with the inertial torque(red-solid line), and the two torques are with comparable magnitude, hence cancels out a large part resulting in small amplitude total aerodynamic torque (orange-dotted line). And the small amplitude total torque therefore results in small pitch angular velocity oscillation.

2.3.3 The scaling between WBMR and wing kinematics

The cancellation between the aerodynamic torque and inertial torque gives us a hint that realistic WBMR may induce an inertial torque which is comparable with the aerodynamic torque and stabilize the body pitch. Thus, a dimensional analysis is conducted as follows: the aerodynamic torque corresponds to the multiplication of aerodynamic force and the arm length that force acts on. $\vec{M}_a = \vec{r} \times \vec{F}_a$. The aerodynamic force is of similar order with the gravity force $m_t\vec{g}$ (Equation 2–3). As for the arm length, a reference length wing length (R) is chosen for the dimensional analysis. The inertial torque is correlated

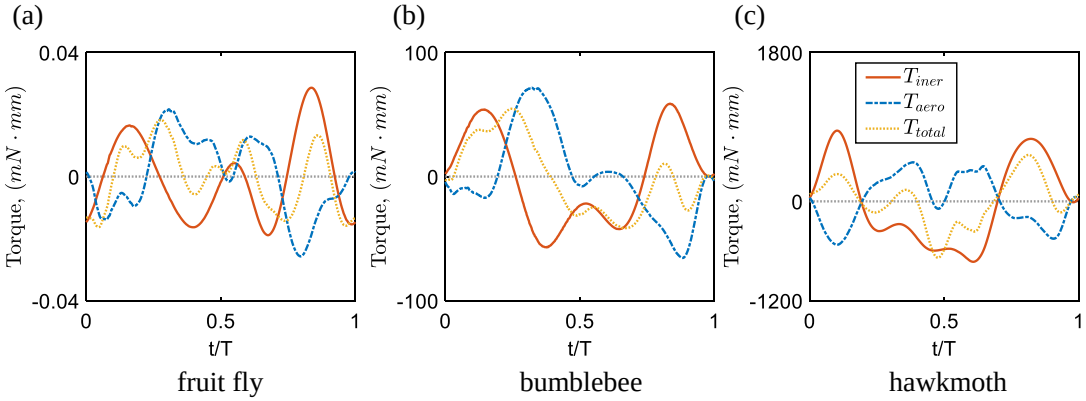

Figure 2–6 Time courses of aerodynamic and inertial pitch torques in hovering: (a) fruit fly, (b) bumblebee, and (c) hawkmoth. Red solid lines denote the inertial torque generated by wings. The blue dashed-dotted line represents aerodynamic torque. The summation of the two torques is represented as the yellow dashed line.

with the MoI of wing and the change of angular velocity as in Equation 2–4.

$$T_a \sim m_t g R \tag{2–3}$$

$$T_i \sim I^{wing} \frac{d\omega}{dt} \sim m_w R^2 \Phi f^2 \tag{2–4}$$

Based on the assumption that inertial torque is of similar order with aerodynamic torque, we have the following Equation 2–5. And we can further deduce the correlation between the WBMR and the wing morphology and kinematics as Equation 2–6 where C_ε is the combination of all the constant factors including gravity acceleration.

$$\frac{T_i}{T_a} = K \tag{2–5}$$

$$\varepsilon = \frac{m_w}{m_t} = \frac{C_\varepsilon}{\Phi R f^2} \tag{2–6}$$

To prove that the scaling is correct in different species, the morphological data of wing as well as the wing kinematic data are accumulated. And Figure 2–7 is plotted with data from literature. Thirteen different species are plotted in the figure with the horizontal axis representing the WBMR and vertical axis being the RHS of Equation 2–6. It is found that the correlation between ε and $(\Phi R f^2)$ resembles a linear relation, thus a straight is fitted for all the data and found a fitting goodness of $R^2 = 0.74$ with

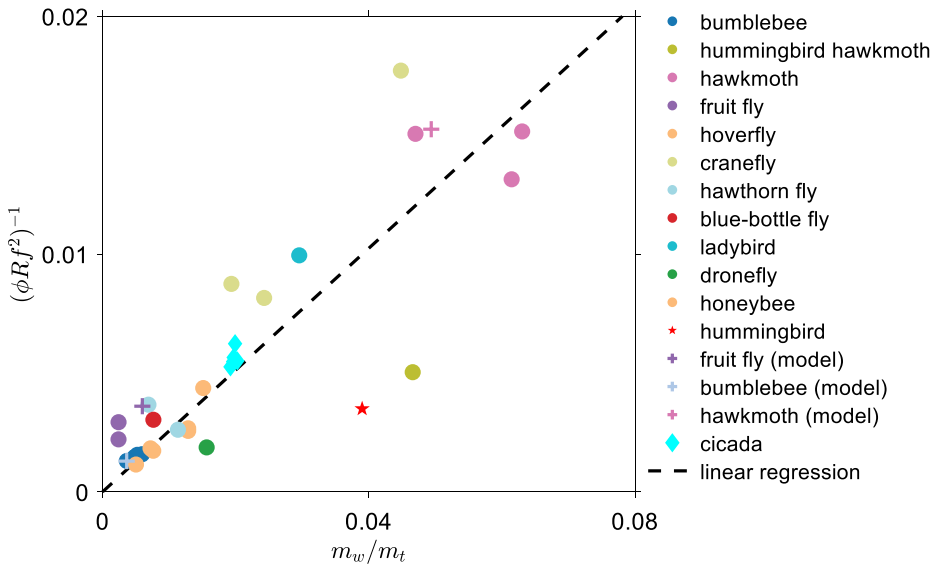

Figure 2–7 The relationship between wing-to-body-mass-ratio and $(\Phi R f^2)^{-1}$ (kinematic & morphological parameters of wing) of different insect species even includes humming bird. The data are obtained from[2, 54-56, 58], and summarized in Table A–2 in supplementary material. A linear regression of all the data is plotted on the bottom layer with the inverse of slope $C_\varepsilon = 3.9448 ms^{-2}$ with $R^2 = 0.74$ for comparison

the slope being $\varepsilon = 3.9448 ms^{-2}$. The reason why the R^2 is not high enough is that: the mass of the species considered ranges over several orders of magnitude from $1mg$ (fruit fly) to $5 \times 10^3 mg$ (hummingbird). Different from insects, birds have skeletons and feathers covering the wing hence leading to larger WBMR which deviates from the linear regression most. Moreover, as the size increases there are different factors that dominants the wing mass thus easily leading to distortion from the linear relationship that we found. With the data of hummingbird and hummingbird hawkmoth which mimics hummingbird being eliminated in the fitting, we obtained a much better goodness of fit $R^2 = 0.88$ and the fitting parameter $C_\varepsilon = 3.5014$. Therefore, we can conclude that insects WBMR correlates with wing morphology and kinematics in a linear relationship of $\varepsilon \sim (\Phi R f^2)^{-1}$, and that insects WBMR is evolved to minimize the body pitching oscillation.

It should also be notified that, in the assumption of Equation 2–3 and 2–4, there exist a preliminary assumption that the body-wing coupling terms are not significant, i.e. the body velocity and angular rotation are small. The $\vec{a}_2$, $\vec{b}_2$ (Equation 2–1(b)) included the

coupling between $\vec{\omega}_b$, $\vec{v}_{CM}$ as well as the wing motion ω_{wing}, while in Equation 2–4 only the wing motion is considered. Thus insects with large body oscillation as butterfly is not included in our fitting.

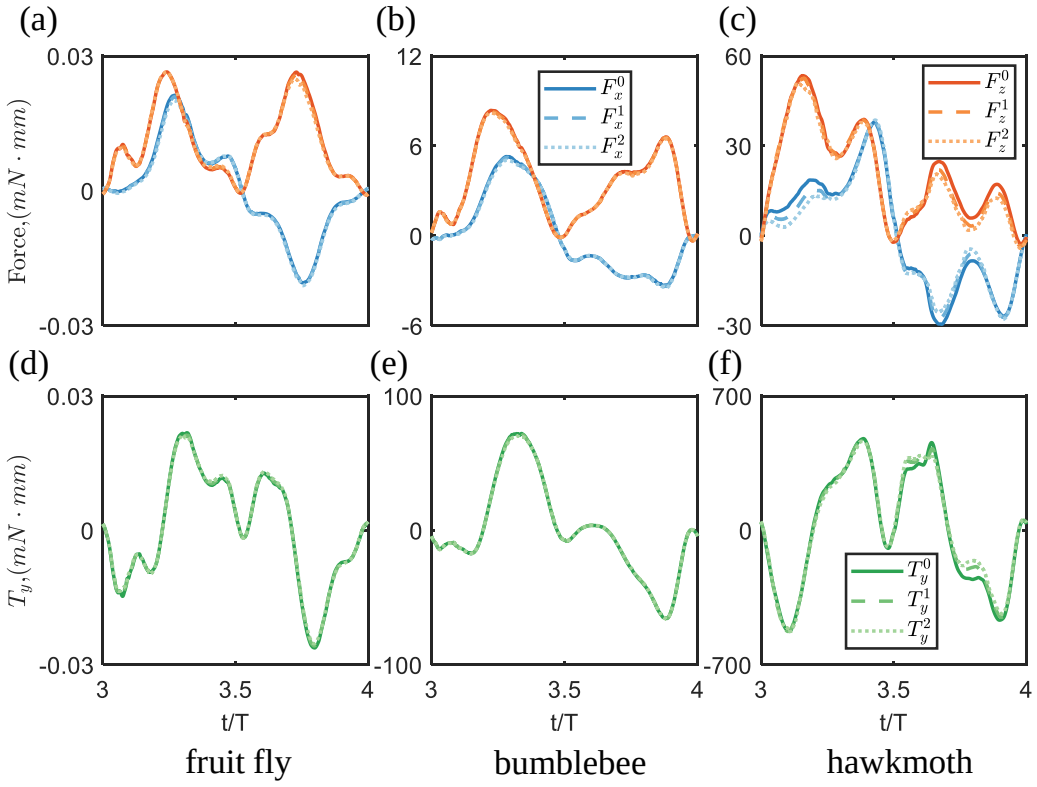

Figure 2–8 Time-varying aerodynamic forces (three components in x, y, and z directions) and pitch torques in a wingbeat stroke with different WBMRs for [(a) and (d)] fruit fly, [(b) and (e)] bumblebee, and [(c) and (f)] hawkmoth. Superscripts (0, 1, 2) correspond to WBMRs ($\varepsilon = [0, 1, 2]\varepsilon_r$).

2.3.4 The WBMR effect on aerodynamic force

The WBMR affects the body directly and the aerodynamics would also be affected due to the fluid-structure-interaction. The aerodynamic force in horizontal and vertical directions with different ε are plotted in Figure 2–8, as well as the aerodynamic torque. The average vertical forces are calculated and plotted in Figure 2–9. It can be found that the average vertical force decrease with the increase of WBMR. The $\bar{F}_z$ decreased 0.82% and 1.51% for bumblebee model(realistic mass distribution) with $\varepsilon = \varepsilon_r$ and $\varepsilon =$

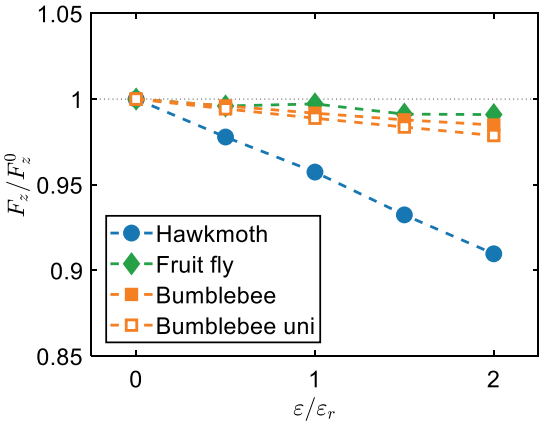

Figure 2–9 Mean vertical forces of fruit fly, bumblebee, and hawkmoth with different WBMRs, which are unified by the vertical force of the zero-wing-mass wing.

$2\varepsilon_r$ compared with $\varepsilon = 0$ case. The F_z reduction in uniform density distribution case of bumblebee is a bit larger due to the larger body oscillation (Figure 2–5(b)(e)). And for fruit fly model, the decrease in $\bar{F}_z$ are 0.28% and 0.91% for ε_r and $2\varepsilon_r$ respectively. The changes in hawkmoth are more significant compared with bumblebee and fruit fly probably due to the large ε_r of around 5% of total mass. The $\bar{F}_z$ reduction is around 4.33% for ε_r and around 10% with $2\varepsilon_r$.

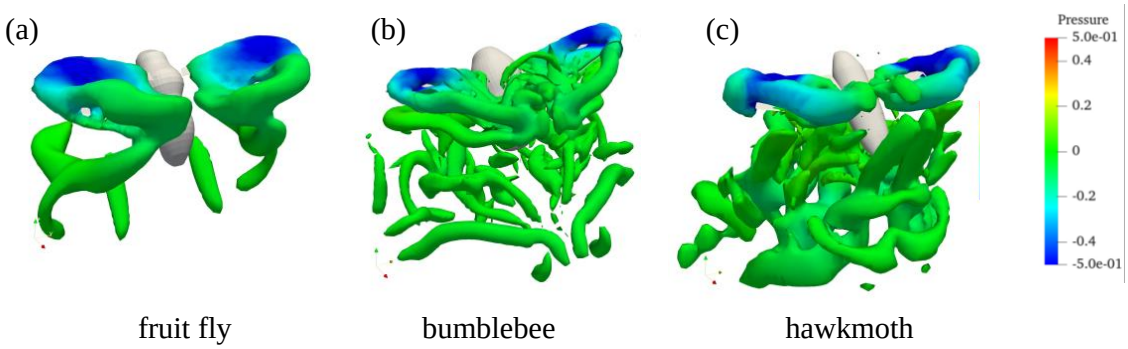

Figure 2–10 Vortex structures about three hovering insect models with realistic WBMRs.

The vortex structure for three models are plotted in Figure 2–10, and the wing surface pressure & streamline distribution are plotted in Figure 2–11 to show how WBMR affect the aerodynamics in detail. It can be found that high WBMR is destructive for the lift force generation.

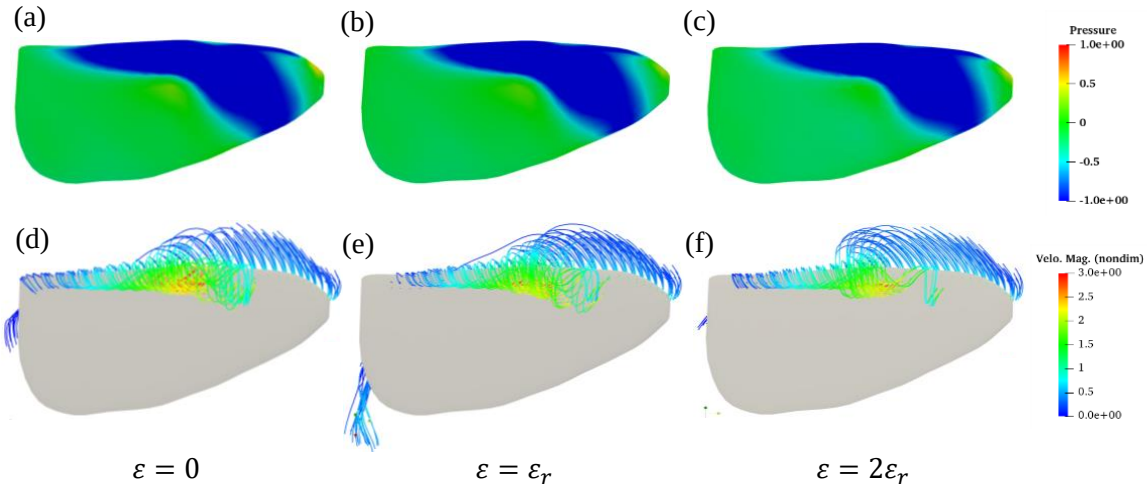

Figure 2–11 Pressure distributions on hawkmoth's wing surfaces and instantaneous streamlines at mid-downstroke, $t = 3.25T$ with [(a) and (d)] zero-wing mass; [(b) and (e)] realistic wing mass; and [(c) and (f)] doubled wing mass.

2.3.5 The WBMR effect on power consumption

Insect flapping power consumption contains two sources of consumption: the inertial power and aerodynamic power(Equation 2–7).High WBMR is usually accompanied with large power consumption especially for insects with high flapping frequency. Hence limited muscle power restrict the allowable flapping frequency in low region when WBMR is large (Figure 2–1). How WBMR affect the power consumption in detail is studied in this section.

$$P_{total} = P_{aero} + P_{iner} \tag{2–7}$$

The average aerodynamic consumption is plotted in Figure 2–13 and compared with former researches. We resulted in the aerodynamic power consumption of $24.6WKg^{-1}$ for fruit fly, $50.8WKg^{-1}$ for bumblebee and $43.3WKg^{-1}$ for hawkmoth. And From Figure 2–13 it can be found that the values are very close to the estimation of previous research.

The transient power consumption of three species are plotted in Figure 2–12. There are two typical peaks of aerodynamic power consumption, mainly locating in the wing translating phase during upstroke/down stroke when lift and drag appears to be maximized. In the majority of the time in a wing beat cycle, the inertial power is positive. But the inertial power consumption may become negative during wing de-acceleration

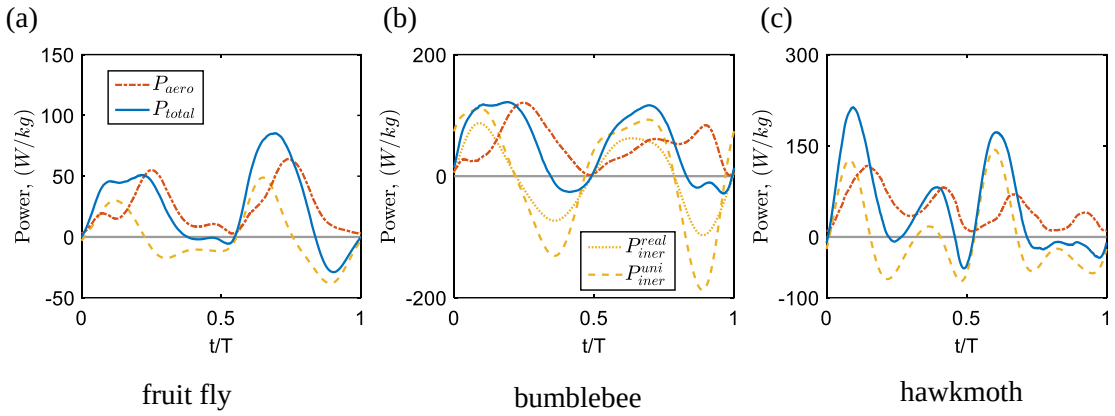

Figure 2–12 Time courses of aerodynamic, inertial, and total powers: (a) fruit fly, (b) bumblebee, and (c) hawkmoth. Red, orange, and blue lines represent the aerodynamic, inertial, and total powers, respectively. Note that in the graph of bumblebee model, P_{real} distribution, respectively, and P_{total} is calculated for the realistic wing.

phase for all three species. How the negative power fits into the energy budget depends on whether elastic storage exists in wing-hinge or musculoskeletal structure. If no elastic storage is existent, a part of the negative inertial power can be transformed into instantaneous aerodynamic power consumption since wing inertial energy during de-acceleration can be dissipated by aerodynamic drag, and the excessive negative power would not be stored, i.e. the negative part of total power P_{total} vanish. Whereas, if perfect elastic storage is assumed, then the negative power can be stored and released when needed, and the total power expenditure would certainly decrease. Therefore, the power expenditure of real insects with dissipation in hinge structure should lie somewhere in between the no storage case and perfect elastic storage case.

The average of total power for different WBMRs are plotted in Figure 2–14. There shows a trend of monotonic increase relationship between WBMR and power. However, for zero-elastic case, there exist a slow growing zone when $\varepsilon < \varepsilon_r$. Taking Figure 2–14(c) as an example, the increment of power with the increase of ε from 0 to ε_r is represented as $\Delta 1$, and the increment of power consumption when WBMR changes from ε_r to $2\varepsilon_r$ is $\Delta 2$. $\Delta 2 \gg \Delta 1$ holds for all three insects, hence it can be concluded that though wing mass lead to increased power consumption, realistic wing mass corresponds to an energy optima with certain requirement for wing stiffness.

Apart from CFD simulation methods to obtain energy consumption, it is mentioned

by Sun[72] that the power can also be predicted through simple dimensional analysis.

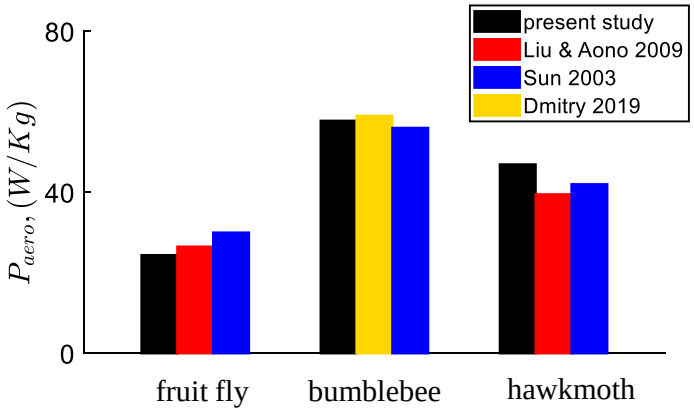

Figure 2–13 Comparison of hovering aerodynamic powers in fruit fly, bumblebee, and hawkmoth[2, 39, 72].

Through similar analysis as inertial torque, the inertial power can be simplified as Equation 2–8 where the C_{pi} is the coefficient of inertial power. C_{pi} is obtained by fitting the $(\varepsilon_r, 2\varepsilon_r)$ with a straight line.

$$P_{iner} = C_{pi} m_w \Phi^2 f^3 R^2 \tag{2–8}$$

The aerodynamic power can be estimated by Equation 2–9 where the C_{pa} is the aerodynamic power coefficient that needs to be calculated from the average aerodynamic power divided by $m_t \Phi f R$.

$$P_{aero} = C_{pa} m_t \Phi f R \tag{2–9}$$

The power prediction according to Equation 2–8 and 2–9 give a quick upper bound for the power consumption, since C_{pi} overestimates the inertial power in the $(0, \varepsilon_r)$ range. The inertial and aerodynamic power coefficients are listed as follows(Table 2–4).

Table 2–4 The aerodynamic and inertial power coefficients for three insect models

Species	C_{pa}	C_{pi}
fruit fly	19.32	10.73
bumblebee[1]	9.59	3.34
bumblebee[2]	9.59	5.46
hawkmoth	17.17	8.11

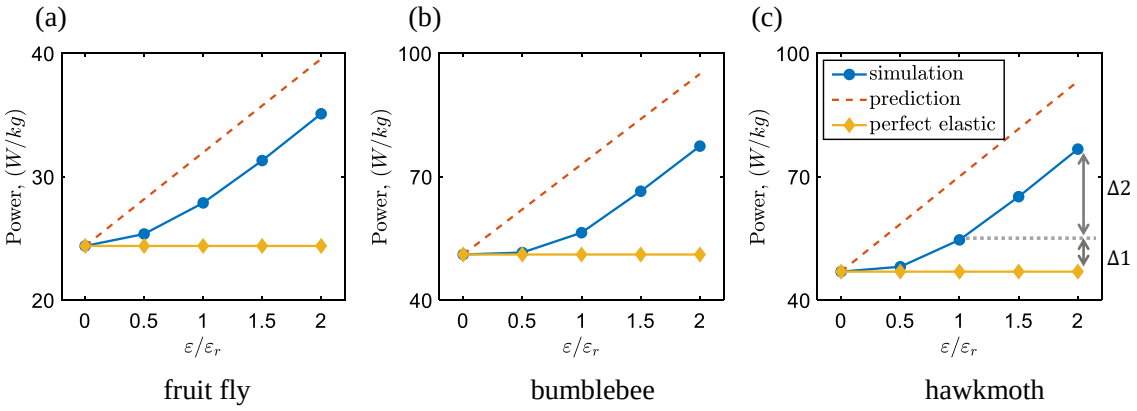

Figure 2–14 Period-averaged total power vs wing-to-body mass ratio: (a) fruit fly, (b) bumblebee, and (c) hawkmoth. Dotted lines: simulation; dashed lines: scaling law-based prediction; blue dotted lines: perfect elastic storage; $\Delta 1$, $\Delta 2$: extra power consumptions of slow- and fast-increase regions

2.4 Conclusions

The effects of wing-to-body mass ratio (WBMR) on insect flapping flights are studied by a versatile, integrated computational model of hovering flight that couples wing-and-body aerodynamics and 3DoF (degree of freedom) body dynamics, with a specific focus on the analysis of free-hovering body dynamics, flapping aerodynamics, and power consumption with three typical insect models such as fruit fly (*Drosophila melanogaster*), bumblebee (*Bombus ignitus*), and hawkmoth (*Agrius convolvuli*), over a broad range of Reynolds numbers $O(10^2) \sim O(10^3)$ and WBMRs [ε_r, with a relative WBMR ($\varepsilon/\varepsilon_r$) from 0%, 50%, 100%, and 150% up to 200%, where realistic ε_r are 0.60% (fruit fly), 0.36% (bumblebee), and 4.94% (hawkmoth)]. The hovering body dynamics are found to be highly correlated with the WBMR, demonstrating that the angular velocity (ω_y) of body pitch approaches a minimized level around the realistic WBMR ($\varepsilon/\varepsilon_r = 1.0$), while the body's translational motion in terms of velocity components (v_x and v_z) presents a monotonic increase in the oscillation amplitude. Investigation on time-varying inertial and aerodynamic torques in a wing-beat stroke reveals that, at most portions of the wing-beat stroke, the three insect models with realistic WBMRs share a novel feature that the wing inertia torques are out of phase with the aerodynamic torques but with comparable amplitude, which leads to much smaller pitch torques in *toto*, hence suppressing the body pitch motions. A scaling law that correlates the WBMR and flapping-wing kinematics is further derived based on 11 different species of insects, demonstrating an approximately

linear relationship between WBMR and $(\Phi f^2 R)^{-1}$, which matches well with measurements and, thus, implies that the WBMR-based body pitch minimization may be a universal mechanism in hovering insects. The WBMR effect on aerodynamic force and torque turns out to be marginal in the three insect models, while a relatively pronounced reduction is observed in hawkmoth with a comparatively larger WBMR ($\varepsilon_r = 4.9\%$) likely due to a body-oscillation induced reduction in the feathering angle. The power consumption is also observed to be highly correlated with the WBMR in a monotonically increasing manner while showing a slow-increase region ($\varepsilon/\varepsilon_r < 1.0$) and a fast-increase region ($\varepsilon/\varepsilon_r > 1.0$) dependent on the interplay between time-varying inertial and aerodynamic powers. While the realistic WBMRs do not correspond to a minimum power consumption, the realistic insect wings are obviously capable of achieving a low-level power cost. Therefore, the realistic WBMR likely offers a novel solution to resolve the trade-off between body-dynamics-based aerodynamic performance and energetic cost. Our results indicate that the WBMR plays a crucial role in the optimization of flapping-wing dynamics, which may be useful as novel morphological intelligence for the biomimetic design of insect- and bird-sized flapping micro-aerial vehicles.

Chapter 3 The kinematic intelligence of intermittent control in stabilizing bumblebee hovering flight

Apart from the wing morphological intelligence which passively stabilizes pitch view during hovering, active control plays a rather important role in stabilization under complex natural environment. Insects control system integrate the inner working system with mechanical system through the feedback information obtained from sensory-motors. Whereas, multiple biological constraints may affect the performance of the control system, such as the limitation of the maximum power output, sensory delay, limited sampling frequency of the sensory-motor, as well as the constraint on the rate of muscle contraction and relaxation. Given multiple constraints on a biology control system, whether insects adopt a smart way for stabilized control remains to be uncovered in this chapter.

3.1 Introduction

Insects are masters of hovering and acrobatic flights, achieving precise,agile,and robust maneuvering through wing kinematics modulation under complex natural environments, which provides a bio-mimetic venture for the design of flapping-wing micro air vehicles[73]. Given the complexities in the musculoskeletal mechanics in association with wing hinge and multiple muscles, the sensorimotor neurobiology, and the flapping-wing and body dynamics, it is intriguing how insects can achieve a closed-loop flight control by integrating external mechanical system and the inner working system[74]. Wing kinematics modulation plays a crucial role in active flight control in insects, which is normally manipulated by steering muscles as illustrated in Figure 3–1. It is observed that there exists a specific correlation between the variations in the wing kinematics in controlled flights and the electromyography (EMG) currents in some steering muscles[11-12, 75], and many conventional proportional derivative (PD)/proportional integral derivative (PID) based feedback control models have been proposed. For instance, yaw control in fruit fly was studied with a time delayed PD control model through the modulation of wing pitch angle difference[29, 76-77]; also, pitch control is observed to be consistent with a PD control policy through altering the front most position of wing[30, 78], and roll control by modulation of bilateral stroke amplitude[28]. Pitch control in hawk moth was also inves-

tigated by coupling the PD control model with some translational velocity feedback[31]. However, it should be notified that different angle controls may not be independent and exclusive. For instance, the yaw control in fruit fly can also be realized through altering stroking amplitude asymmetrically[77], indicating multiple ways to realize control. The conventional PD/PID control-based methodology however is, in general, implemented in a manner of continuous way.

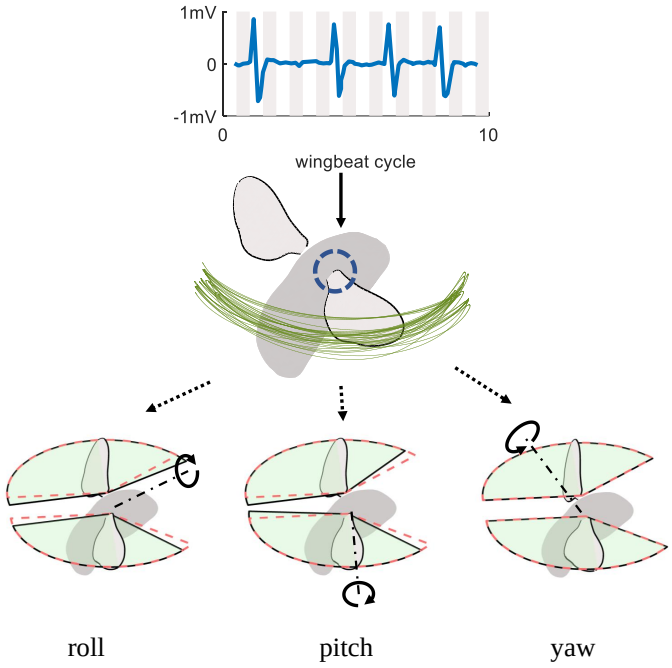

Figure 3–1 Sketch diagram of intermittent spike firing in steering muscle inside wing hinge in body-posture control. The typical EMG of steering muscle is plotted on the top[79], where the spike is fired every several wingbeat cycles, leading to subtle variations in wing kinematics. Here for each angle control a candidate control method is illustrated in terms of mean stroke angle for pitch control[78], bilateral stroke amplitude difference for roll control[28], and wing pitch angle difference for yaw control[29]

Insect flight execution is mainly realized by two groups of flight muscles: indirect flight muscles (IFMs) which fill in most of the volume in the thorax and generate mechanical power required for flight, steering muscles which directly insert within the wing base which ensures rapid control during maneuver[11, 80-81]. Many of the high wing beat frequency insects, their IFMs are asynchronous, referring to an absence of 1:1 correspondence of neuron spike and muscle twitch[80]. The timing of contraction is determined by the mechanical oscillation of the thorax. The asynchronous flight muscles may affect

flapping frequency, yet not involved in the fine control of turning as pointed out by Tu & Dickinson[82]. However, the steering muscles are synchronous for the sake of rapid modulation of wing kinematics in each stroke, i.e. one neuron spike will result in a muscle twitch. In insect flights, it is observed that various EMG measurements associated with steering muscles display an intermittent spike firing in steering muscle inside wing hinge in body-posture control[11-12, 75]. In association with blowfly steering muscles, for instance, an intermittent spike firing is observed characterized by two largest basalare muscles (b1,b2), in which muscle b1 is spiked mostly once per wingbeat while the spike of muscle b2 happens every several cycles[11, 81]. b1, b2 together shapes the shape and amplitude of wingtip trajectory[81], and a single spike in b2 is correlated with large transient increase in amplitude which typically lasts for only one cycle in *Calliphora*[81]. The steering muscles b1, b2 are synchronous ones[82-83], thus have a clear correspondence between neuron spike and twitch force generation. It should be notified that the intermittent spiking in steering muscle is different from the asynchronous IFMs which also seems to spike intermittently, the intermittency of the steering muscle b2 is directly correlated with transient stroke amplitude change which lasts for one cycle, while one spike in IFMs may results in several muscle twitch that lasts for several cycles[80-81]. A similar intermittent feature of spike firing is also found in fruit fly basalare muscle[79]. A limited spike rate in steering muscle b1 is observed corresponding to a clock-driven control[84] for the wing schematic modulation rate [19]. On the other hand, the steering muscle b2 presents a nonperiodic spike pattern punctuated by empty cycles in correspondence to an event driven control[84], pointing to the existence of a threshold for feedback signal, only if the signal cross beyond the threshold will the control starts. While these flight controls are of the intermittent characteristics, only the clockdriven control is taken into consideration in previous studies[26, 85]. The event-driven intermittent control remains untouched, leaving an open question whether the intermittent control strategy can provide benefits for flight-control stabilization in insects. Though steering muscles may couple with each other during control, and may be able to control multiple directions of wing rotation, which might be more complicated than what is assumed in this paper, here we intend to propose a simplified model for the flight control strategy which possess the intermittent feature of basalare muscles rather than establishing a direct model of real insect flight.

Flight control in insects requires complicated motor systems in response to multimodal sensory inputs[73-74], which are normally based on the visual system and/or

mechanosensory system such as gyroscopic halteres in flies[80]. Such inner working system will lead to some sensory delay, which comprises afferent and efferent delays, thus dominate control stabilization robustness. A proportional controller working at high gain with substantial sensory delay often leads to somehow overshooting and hence unstable oscillation[31, 76]. It is reported that in fruit flies, the sensory delay in terms of roll control is around 1–1.5 wingbeats[28] but 2–5 wingbeats in yaw control[29]. For hawkmoth, a large insect with a lower flapping frequency, the delay is shortened to one wingbeat, e.g. in pitch control[30]. For bumblebee, Bombus terrestris, it is observed of a photoreceptors response within 8–12 ms under light stimuli[86], corresponding mostly to one wing-beat, and of a delay of visual attitude control of approximately 20 ms, i.e. two wing-beats[87], and thus the sensory delay in the active-flight control of bumblebee is 1–2 wingbeats.

Turbulent-rejection capability is another key factor in terms of stabilization robustness for insects to remain stable in unsteady winds and be maneuverable enough to avoid obstacles[74], which can be dealt with as a problem of dynamic flight stability under external disturbances[28, 78]. However, it is yet poorly understood whether the intermittent spike firing would bring benefits or not compared to the conventional continuous control. A recent study of control parameter sensitivity analysis with a PD model of flight control in bumblebee hovering demonstrated that the PD continuous control model is highly sensitive to control parameters, easily leading to oscillation and even divergence even under slight variations in control parameters[85]. It is thus argued that while the continuous control strategy is simple enough to model flight controls in a straightforward way, it would likely degrade the control stability due to the sensory delay[26, 88].

In this study, we proposed a novel intermittent control strategy for a 3DoF pitch-control and explored its stabilization robustness in bumblebee hovering. We developed an integrated computational model with a combination of clock-driven and event-driven assumption of control strategy, which comprises an insect-inspired dynamic flight simulator and a novel discrete feedback controller as well as a simplified free-flight dynamic model. We examined whether the flight stabilization can be improved in terms of sensory delay, initial perturbation amplitude, and spike interval as well as damping strength. We first give a description of an insect-inspired dynamic flight simulator and modeling of free-flight dynamics as well as the intermittent control model and the simplified model for intermittent and continuous controls. We then describe the simulation results and give an extensive discussion on how the novel intermittent control strategy can enhance flight

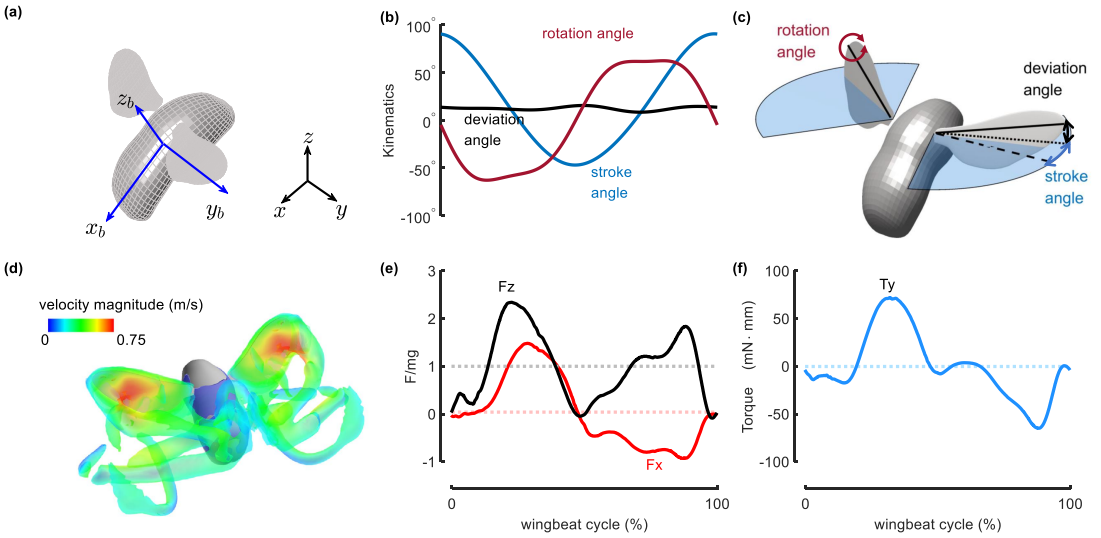

Figure 3–2 (a) CFD model of a hovering bumblebee in two coordinate systems: a global coordinate system, xyz and a body-fitted coordinate system, $x_b y_b z_b$. (b) Time courses of stroke angle, rotational angle, and deviation angle relative to stroke plane in hovering. (c) Definitions of three angles and stroke plane. (d) Flow structures around a hovering bumblebee in terms of vorticity iso-surface with a colormap of velocity magnitude. (e) Time courses of aerodynamic forces in a wingbeat stroke: horizontal force, F_x (red solid) and vertical force, F_z (back solid) with period-averaged $\bar{F}_z = 1.0Mg$ (black dotted) and $\bar{F}_z = 0.039Mg$(red dotted), respectively. (f) Aerodynamic torque (blue solid) around y-axis with period-averaged $\bar{T}_y = -0.0129Mgc_m$ (blue dotted).

stabilization robustness.

Table 3–1 Model parameters of bumblebee.

Model Parameters	Value/Equations	Measurement Units	Descriptions
Morphological Parameters			
c_m	4.1	mm	mean chord length
R_{wing}	15.2	mm	wing length
L	21.0	mm	body length
$\vec{r}_{pivot2CoM}$	vector from wing pivot to wing center of mass with components $(r_x, 0, r_z)$		
Kinematic Parameters			
M_b	391.0	mg	mass of bumblebee
g	9.8	ms^{-2}	gravitational acceleration
f	136.0	Hz	flapping frequency
I_{yy}	1.4192×10^{-8}	kgm^2	moment of inertial around y axis
ν	1.5×10^{-5}	m^2	kinematic viscosity of air

Continuation of Table 3–1

Model Parameters	Value/Equations	Measurement Units	Descriptions
ρ_{fluid}	1.225	kgm^{-3}	density of air
ϕ			wing stroke angle
ϕ_{amp}	139.4	°	wing stroke amplitude
$\Delta\phi_{mean}$			mean stroke deviation
Re	2750		Reynolds number
u_{ref}	$2\phi_{amp}R_{wing}f$		average wingtip velocity
Time Parameter			
T	$1/f$	s^{-1}	time of one wing beat cycle
Torques			
T_y	total aerodynamic torque around y axis around CoM		
$\bar{T}_y$	time average of T_y		
$\bar{T}_{hinge}$	average aerodynamic torque around wing hinge		
T_{action}	action torque induced by wing kinematics alteration		
T_{damp}	damping torque induced by body rotation		
T_{cylic}	cyclic aerodynamic torque induced by wing flapping		
Forces			
F_x^b	aerodynamic force x component in body frame		
$\bar{F}_x^b$	time average of F_x^b		
F_z^b	aerodynamic force z component in body frame		
$\bar{F}_z^b$	time average of F_z^b		
State Variables			
θ	pitch angle		
θ_{equi}	pitch angle in trim hovering state		
$\Delta\theta$	$\theta - \theta_{equi}$		pitch angle deviation
$\theta(t - nT)$	sensor perceived pitch angle with nT delay		
ω	pitch angular velocity		
ω_{equi}	pitch angular velocity in trim hovering state		
$\Delta\omega$	$\omega - \omega_{equi}$		pitch angular velocity deviation
$\omega(t - nT)$	sensor perceived pitch angular velocity with nT delay		
v_x^b, v_z^b	velocity component in body fixed frame		
Control Parameters			
P	proportional gain in feedback control		
P_{ref}	reference proportional gain		
D	derivative gain in feedback control		
D_{ref}	reference derivative gain		

Continuation of Table 3–1

Model Parameters	Value/Equations Measurement Units Descriptions
α	empirical parameter which decides the 'ON','OFF' control action
Fitting Parameters	
K_{action}, C_{action}	the fitted conversion coefficient between $\Delta\phi_{mean}$ and torque
K_{damp}	the conversion coefficient between ω_y and T_{damp}
A_{amp}, k, A_0, ψ	parameters of the fitting equation3–21
λ	convergence ratio of a pitching curve
k_0	the slope of the intersection point from origin in figure 3–9
Coordinate Systems	
xyz	ground frame
$x_b y_b z_b$	body fixed frame

3.2 Methods

3.2.1 Computational Fluid Dynamic simulator

An insect-inspired in-house flight solver[52] is adopted in this study. A Fortified-Finite-Volume-method-based Navier-Stoke solver is developed for dynamically moving multi-blocked overset-grid system. Details of the governing equation can be found in the Introduction chapter. There are four blocks of grids in total, two of them are wing grids, one is the body grid, and another is called background grid. The simulator is validated and verified through some benchmark tests. In this paper, a 3DoFs body dynamic equations (Equation 3–1$\sim$ 3–3) are loosely coupled with the NS flow solver at each physical time step.

3.2.2 Modeling of free dynamics

In this study, we investigate the intermittent control stabilization robustness during hovering with a specific focus on pitch control. Due to that pitch control can be decoupled from other angles such as roll and yaw, which is realized through bilateral symmetric change in wing kinematics (Figure 3–1). Another reason why we choose pitch instead of the other two angles is that, different from body roll and yaw which benefit from damping effect such as the flapping counter torque[89-90]. Pitch angle is sensitive towards perturbation corresponding to intrinsically unstable oscillatory mode[90]. Hence, pitch control can better reflect the control robustness, providing a perfect circumstance for the comparison of continuous control and intermittent control. While only pitch control is studied in

present work, the application intermittent model is not limited to pitch control since they share the same hinge muscle actuation system.

The governing equation of rigid body regarding pitching is with three degree of freedom in body fixed frame as shown in the following (Equation 3–1, 3–2, 3–3)[68, 90].

$$\frac{dv_x}{dt} = \frac{F_x^b}{M} - gsin\Delta\theta \tag{3–1}$$

$$\frac{dv_z}{dt} = \frac{F_z^b}{M} + gcos\Delta\theta \tag{3–2}$$

$$I_{yy}\frac{d\omega_y}{dt} = T_y \tag{3–3}$$

Here the v_x^b, v_z^b represents the CM velocity components, ω_y represents the body pitch angular velocity. $\Delta\theta$ is the pitch deviation angle from equilibrium state. F_x^b, F_z^b, T_y represent the corresponding force and torque components, and I_{yy} represents the moment of inertial around body CM, m the body mass, g the gravity acceleration. Note that the I_{yy} calculation is based on realistic body mass with a body shape approximating the real body shape, and further with uniform density distribution assumption. It can be seen from the dynamic equations that the wing inertia effect is neglected, because the wing mass takes less than 0.2% of total mass, also that, our control perturbation is small hence wing kinematics alteration would be small enough to neglect the wing inertia. The body rigid dynamic equation is loosely coupled with the NS solver and solved in a manner of 4th order Runge-Kutta[68]. The aerodynamic torque and force are the resultant force/-torque obtained from our CFD solver with body translation/rotational effect taken into consideration.

3.2.3 Morphological and kinematic models of bumblebee

A wing-body model based on our previous research is constructed with body mass(m_b) $391mg$, a body length (L) of $21.0mm$, wing length (R_{wing}) of $15.2mm$ and mean chord length (c_m) of $4.1mm$. The wing kinematics during hovering is digitized from three synchronized high-speed-cameras in experiments[39], and three angles are defined respect to the stroke plane to describe the kinematics, i.e. the stroke angle, the deviation angle from the stroke plane, and the wing rotational angle. The three angles re defined relative to the stroke-plane (SP) which is constructed by the closest plane that fits the wing-tip-trajectory in a full cycle. In bumblebee hovering, the plane almost coincide

with the horizontal plane, i.e. stroke plane angle (SPA) is 0˚. Stroke angle corresponds to the wing tip sweeping angles on the stroke plane, and elevation angle is the wing tip elevation respect to the stroke plane, furthermore, rotation angle defines the wing rotation around the tip-to-base axis. The morphological and kinematic models are illustrated in Figure 3–2(a)-(c). The morphological and kinematic parameters are summarized in Table 3–1.

The reference velocity is chosen as the mean wingtip velocity and the corresponding Reynolds number are calculated as following (Equation 3–4 & 3–5):

$$u_{ref} = 2\phi_{amp} R_{wing} f \tag{3–4}$$

$$Re = \frac{u_{ref} c_m}{\nu} \tag{3–5}$$

To achieve a trim hovering state, it is crucial to determine the center of mass(CM) position. One typical method is to assume a uniform density distribution, which however, wouldn't always satisfy the equilibrium condition regarding torque. We assume that the CM position lies along the body longitudinal axis. Based on a preliminary simulation of tethered bumblebee, the aerodynamic torque around wing hinge (T_{pivot}) as well as the aerodynamic force F_x^b, F_z^b in body fixed frame can be obtained. Here we assume the vector from wing hinge to body CM being $\vec{r}_{pivot2CM} = [r_x^b, 0, r_z^b]$, with r_z^b prescribed by the geometric model and r_x^b remains to be determined. Hence, the aerodynamic torque around CM can be calculated as Equation 3–6, and the time integral of the aerodynamic torque should be zero, resulting in Equation 3–7, and the CM position can be determined according to Equation 3–8

$$T_{aero} = T_{pivot} + \vec{r}_{pivot2CM} \times [F_x^b, 0, F_z^b]. \tag{3–6}$$

$$\int_0^T T_{aero} dt = \int_0^T T_{pivot} dt - \int_0^T r_x^b F_z^b dt + \int_0^T r_z^b F_x^b dt \tag{3–7}$$

$$r_x^b = \frac{\bar{T}_{pivot} + r_z^b \bar{F}_x^b}{\bar{F}_z^b} \tag{3–8}$$

3.2.4 An intermittent control model

The intermittent control model proposed here posses both the feature of clock-driven control as well as event-driven control, and implemented with a PD model determined by

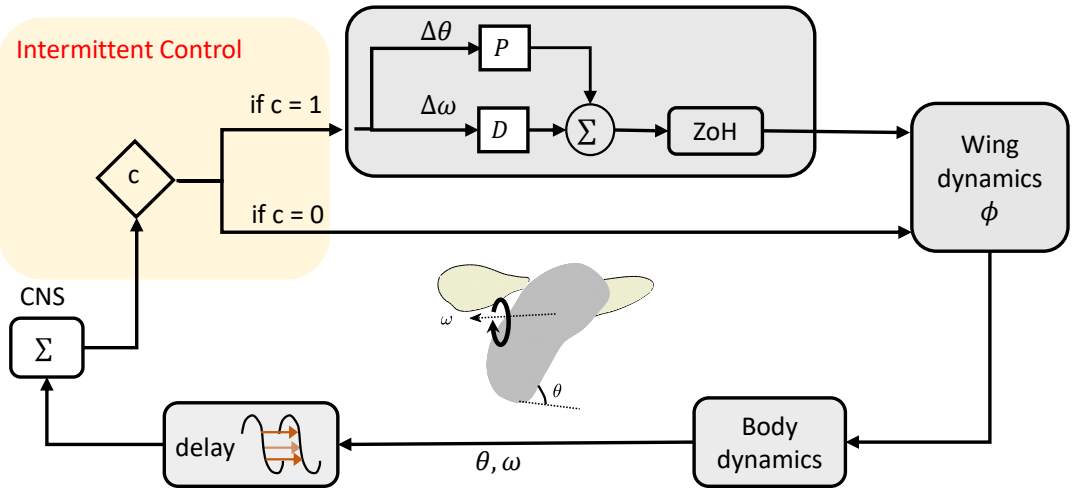

Figure 3–3 Schematic diagram of the intermittent control strategy for pitch angle. The light golden shaded area represents intermittent control decision part, being switched to ON if $c = 1$ else OFF at $c = 0$

certain intermittent conditions. The control diagram of intermittent control is illustrated in Figure 3–3. The clock-driven is represented by an Zero-Order-Hold in the control diagram (Figure 3–3), which describes the fact that with high wing flapping frequency, insects like *Calliphora*'s basalare muscle can only be spiked once at most during each wing stroke. Thus, the strength of control action should also maintain the same during the whole period. And the event-driven control is represented in the light-yellow box in Figure 3–3 that when certain condition is satisfied, the PD control is turned 'ON' while if any of the conditions not met, the system becomes an open-loop system without control (control 'OFF').

According to Dickinson & Balint[11, 91], the biggest steering muscles basalare muscles 1&2 (b1,b2) are spiked intermittently with b1 spiked once in each stroke while b2 spiked once in several strokes. The event-driven control arises from the assumption that if b2 is only spiked when certain conditions met. Since b2 spike is correlated with transient increase in stroke amplitude that last for one wing beat cycle according to[91], and there exists one-to-one correspondence with the spike and muscle twitch in steering muscles, it would be reasonable to directly correlate a single neuron spike with certain wing kinematics alteration hence the aerodynamic force & torque generation. While there exist many steering muscles that may be spiked at the same time, and muscles may not

work independently[11, 91-92], we only mean to pay attention to the bio-inspired intermittent nature. The intermittent nature of the central nervous system has been observed in human quite standing[93] and human related tasks such as the stick-balancing on fingertip[94-95]. And it is found that the intermittent control during a inverted pendulum task is able to compensate for the instability induced by sensory & control delay[94], we intend to investigate how the intermittent control would affect the pitch control stability during bumblebee hovering.

In the pitch control model, two system state variables are introduced: θ, ω representing the body pitch angle and pitch angular velocity, and θ_0, ω_0 denotes the hovering state value, where in bumblebee hovering the equilibrium state pitch angle is 45°[39]. Thus, the deviation from equilibrium can be represented as: $\Delta\theta = \theta - \theta_0$, $\Delta\omega = \omega - \omega_0$. And a time delay of n wing beat cycles is represented as $(t - nT)$.

The clock-driven control is realized through altering wing $\Delta\phi_{mean}$ only once at the start of each wing beat cycle which is determined by the time-delayed feedback state deviations. In bumblebee control, it is reported that the sensory delay is around one to two wing beat cycles[96-97], thus in our model, we also consider the situations with $1 \sim 2T$ delay. The intermittent control diagram is shown in Figure 3–3, with the intermittent conditions such as:

$$\omega_{min} < \Delta\omega(t - nT) < \omega_{max} \tag{3–9a}$$

$$\Delta\theta(t - nT)\Delta\omega(t - nT) < 0 \tag{3–9b}$$

$$\alpha|\Delta\omega(t - nT)nT| < |\Delta\theta(t - nT)| \tag{3–9c}$$

The three intermittent conditions can be interpreted that: when the angular deviation is within certain threshold due to biological constraints (Equation 3–9(a)), and the current body posture is in a restoring direction Equation 3–9(b), and the predicted angle will not overshoot Equation 3–9(c), then the PD control is turned OFF which becomes open-loop control, while if either one of the conditions not met, the PD control will be turned ON, becoming a closed-loop PD control. According to Hedrick et.al[89], there exist certain threshold for angular velocity sensory and control. If angular velocity is beyond the threshold, then it overflows for the sensors and insects & birds will not make further control actions to compensate for the overflow, which forms our basis of Equation 3–9(a). Other two equations are inspired from the intermittent control of inverted-pendulum task[96].

It should be notified that in Equation 3–9(c) we introduced an empirical parameter α in the control conditions so that the OFF range can be constrained and changed. Assume α being 0, then Equation 3–9(c) will always be satisfied, then the number of open-loop cycles will be maximized. Otherwise if $\alpha \sim \infty$, the third condition will not hold, hence the control will degenerate to a delayed PD feedback control. α is chosen 0.02 temporarily in our study to allow for more open-loop cycles, and the sensitivity regarding the empirical parameter will be discussed in later sections.

Regarding the control action in control diagram Figure 3–3, it is known that fruit fly achieves pitching maneuver by shifting the wing front-most position during flapping[30, 78], the fMAV Robobee controls its pitch attitude by adjusting the mean positional angle (ϕ_{mean})[98]. Both methods shifts the center of the pressure forward or backward to induce a pitch up/down torque. Hence, in our bumblebee pitch control model, the control action in pitch is correlated with shifting the ϕ_{mean} which can both generate a pitch torque as well as maintaining the same lift force. The relation between pitch torque and $\Delta\phi_{mean}$ is studied by five CFD simulations with $\Delta\phi_{mean}$ ranging from -10° to 10° as shown in Figure 3–4. And there shows an apparent linear relationship between the $\Delta\phi_{mean}$ and the pitch torque, as Equation 3–10, the K_{action} and C_{action} can be obtained by linear regression method.

$$T_{action} = K_{action}\Delta\phi + C_{action} \tag{3–10}$$

3.2.5 Simplified model for continuous and intermittent control

For insects with swift control response like fruit fly, it takes around 10 wing beat cycles to recover to equilibrium state[29], which takes several days to complete simulating one case in our in-house solver. It requires more computational time to compare the intermittent control and continuous control model. Hence, a simplified model is required for massive cases prediction and comparison. In this section, a simplified model is established based on some assumptions and proved to be reasonable in later sections.

The aerodynamic torque can be decomposed into three components, i.e. the cyclic aerodynamic torque due to the periodic wing flapping motion T_{cyclic}, the extra aerodynamic torque generated by wing kinematics alteration, the damping torque due to body rotation T_{damp} such as Equation 3–11):

$$T_{aero} = T_{cyclic} + T_{action} + T_{damp} \tag{3–11}$$

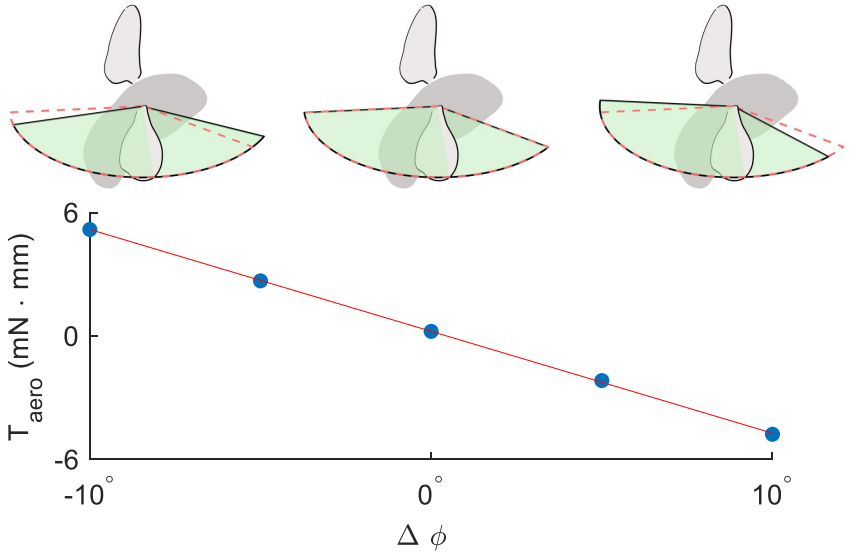

Figure 3–4 Variation in shifted mean stroke angles vs pitch torques. Sectors with red dashed boundaries represent stroke angles in hovering; light green sectors are stroke angles with a shift, $\Delta\phi$. Shifts in positional angle are $-10°, -5°, 0°, 5°, 10°$ fitted by a linear regression (red line) with coefficients of $K_{action} = -0.495mN \cdot mm/deg$, $C_{action} = 0.226mN \cdot mm$, corresponding to pitch torques (blue filled circles).

Here the T_{cyclic} can be obtained from a trim hovering case of bumblebee, and set as periodic prescribed value for our simplified model. And the action torque is determined by the feedback as Equation 3–12 in a way that: action torque is linearly correlated with the summation of pitch angle deviation from equilibrium state with a proportional gain (P), and also linearly correlated with angular velocity deviation with a gain D.

$$T_{action} = P(\theta(t - nT) - \theta_0) + D(\omega(t - nT) - \omega_0) \tag{3–12}$$

According to Equation 3–10 and 3–12, we can obtain a certain discipline for altering the wing kinematics in CFD under the instruction of feedback information (Equation 3–13).

$$\Delta\phi = \frac{P(\theta(t - nT) - \theta_0) + D(\omega(t - nT) - \omega_0) - C_{action}}{K_{action}} \tag{3–13}$$

The damping torque can be approximated by an assumption that the torque is linearly correlated with body pitch angular velocity (Equation 3–14). And we simulated one case with initial angular velocity $180°s^{-1}$, calculated the average damping torque in one cycle to be $\bar{T}_{damp} = -0.337mNmm$. Hence the corresponding non-dimensional damping coefficient $K_{damp}^{dimless} = -30.8294$. Note that the damping coefficient is is a rough

estimation for the damping torque caused by body pitching. If the initial perturbation increased significantly, the linear relationship may not hold, however, under current small perturbation amplitude, it should be safe to assume such linear relationship.

$$T_{damp} = K_{damp}\omega(t) \tag{3–14}$$

Combining the body dynamic Equation 3–3 and the simplified model for aerodynamic solver Equation 3–12 and Equation 3–14, a simplified model to predict the effect of control parameters effect as well as intermittent control effect can be established as the following:

$$I_{yy}\frac{d\omega(t)}{dt} = K_{damp}\omega(t) + P(\theta(t-nT)-\theta_0) + D(\omega(t-nT)-\omega_0) + T_{cyclic} \tag{3–15}$$

The simplified model is solved with delayed-differential-equation method (dde23) in Matlab for high accuracy. In simplified model, the action torque and damping torque can be calculated totally based on the information of former& current state parameters, while in CFD it is computed through the fluid-dynamics coupling process which is very time consuming. However, it should be mentioned that, the simplified model ignored the translation motion induced torque and ignored the coupling effect between translation& rotation, while in CFD simulation all the factors are included. Though with many factors ignored, our simplified is still proved to be a reasonable prediction for the control behavior in later sections.

3.2.6 The control parameters P, D

The control system characteristic equation of a dynamic system with delayed feedback control can be written as Equation 3–16 in the frequency domain, where $C(s), H(s), P(s)$ represent the transfer function of a feedback controller, sensory delay, and open-loop dynamics separately. $\tau_p = \frac{I_{yy}}{K_{damp}}$ is the system open-loop time constants, which represents how fast the system decays. τ_c is the controller constant defined as $\tau_c = \frac{D}{P}$, P is the controller gain, and Δt is the sensory delay.

$$1 + C(s)H(s)P(s) = 0 \tag{3–16}$$

$$C(s) = P(1 + \tau_c s) \tag{3–17}$$

$$H(s) = e^{-\Delta t s} \tag{3–18}$$

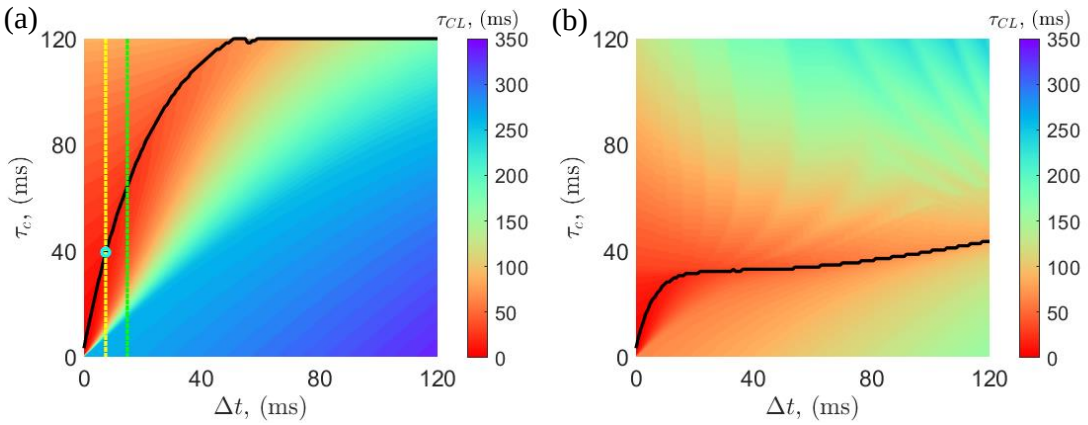

Figure 3–5 The closed-loop time constant of a continuous bumblebee model with PD feedback control. (a) with damping coefficient $K_{damp} = 1.0K_0$, (b) with $K_{damp} = 3.0K_0$. The black-solid line represents the minimum τ_{CL} position, the yellow-dashed line and green dashed line represent a delay of $1T$ and $2T$ respectively.

$$P(s) = \frac{1}{I_{yy}} \frac{1}{s^2 + \frac{1}{\tau_p} s} \tag{3–19}$$

Third order Padé approximation is used to expand the exponential term in $H(s)$ into polynomials so as to conduct preliminary analysis for the control parameters. Root Locus method (rlocus function in MATLAB) is used for calculating the roots (p_i) of the characteristic equation, root with only negative real part represents a damping mode, while positive real part represents a diverging mode, and roots with imaginary part denotes an oscillatory mode. A proper choice of control parameters corresponds to all roots with negative real components, while the most appropriate control parameter correspond to the minimum value of τ_{CL} which represents the closed-loop time constant (Equation 3–20).

$$\tau_{CL} = \tau_{CL}(\Delta t, \tau_c P) = \frac{1}{\min_i(|Re(p_i)|)} \tag{3–20}$$

For different combinations of τ_c and Δt, the resulting closed loop time constant map is illustrated in Figure 3–5. From Figure 3–5(a), the intersection point between the minimum τ_{CL} and the yellow dashed line represent the best choice of $\tau_c \sim 39.46ms$, indicating the non-dimensional $\frac{P}{D} \sim 96.34$. Here the non-dimensional reference feedback gain P is chosen as $P_{ref} = 120$, and the reference D is chosen as $D_{ref} = 1.5$ based on previous τ_c estimation. Moreover,it can also be predicted that with the increase of system damping factor K_{damp}, the tolerance of sensory delay becomes higher,since the high damping factor intrinsically leads to a more robust system.

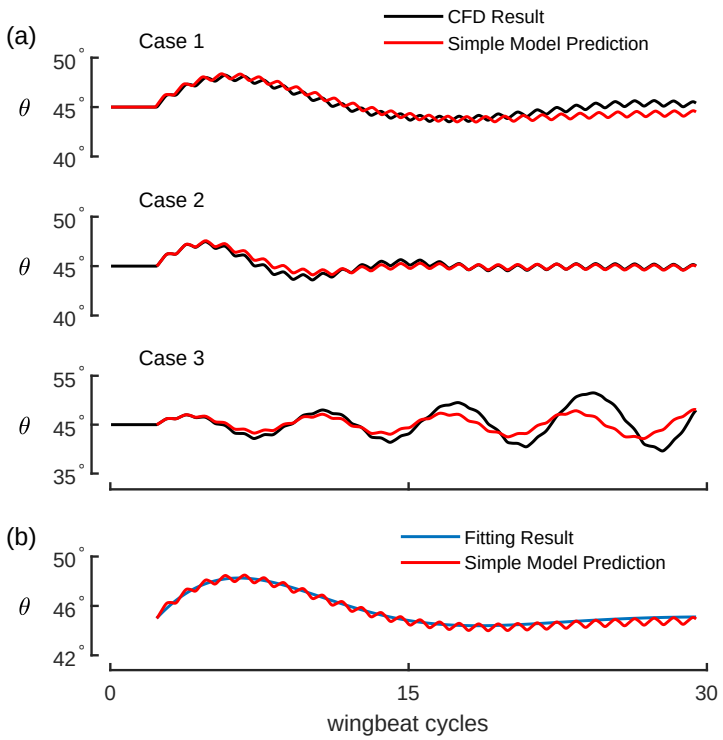

Figure 3–6 (a) CFD validation for simplified continuous model: three cases are with different control parameters, case 1 (P_{ref}, D_{ref}), case 2 ($2P_{ref}$, $2D_{ref}$), case 3 ($4P_{ref}$, $4D_{ref}$), but with the same initial angular velocity perturbation of $\omega_0 = 180^{\circ}s^{-1}$ and 1T delay. Black and red solid lines represent CFD and simplified model-based pitch angle, respectively. (b) Comparison between simple model (red solid as in case 1) and a fitting function (blue solid), $\theta(t) = A_{amp}sin(2\pi t + \psi)e^{\lambda t} + A_0$.

3.2.7 Indices for evaluating control performance

Stabilization robustness is examined in the control parameter space (P, D) for both intermittent control as well as continuous control. The range of (P, D) is chosen to be $P \sim [0.5P_{ref}, 6P_{ref}]$, $P \sim [0.5D_{ref}, 4D_{ref}]$ with an interval of 0.1.Since weak feedback control will require long time for recovering to equilibrium, while too strong control actions will easily lead to overshoot hence oscillatory diverging result, the range of $[0, 0.5P_{ref}]$ $[0, 0.5D_{ref}]$ region are ignored in our study.

The CFD results and simplified model results are plotted for comparison in Figure 3–6 with three combinations of (P, D) control parameters with the same magnitude of initial perturbation. The controlled pitch trajectories shows apparent difference which can be classified into three modes, an over-damping mode resembles Figure 3–6(a), an oscillatory-damping mode of Figure 3–6(b) and oscillatory-diverging mode as Figure 3–

6(c). To quantify the stabilization of control, we composed the following Equation 3–21 which can resemble all the three modes by fitting the four parameters (A_0, A_{amp}, k, λ). Levenberg–Marquardt fitting algorithm is used with proper initial assumption of the four parameters. To ensure a fast converged fitting, an initial guess is applied for the fitting of case ($0.5P_{ref}$, $0.5D_{ref}$), and the parameters which ensure best fit is applied as initial guess for the surrounding cases on the PD checker-board map. As shown in Figure 3–6(d), the Equation 3–21 enables an excellent fitting.

$$\theta(t) = A_0 + A_{amp} sin(2k\pi t + \psi)e^{\lambda t} \tag{3–21}$$

Two indices are chosen for quantifying control stabilization, λ representing the convergence ratio, as well as $max(|\theta(t)-\theta_0|)$ representing the maximum pitch angle deviation from equilibrium. The maximum deviation angle should be small enough to ensure a successful control, since a large deviation of pitch angle will redirect the lift force direction hence leading to stumble. The maximum deviation angle reflects short term stabilization, while the convergence ratio λ reflects long term stabilization. $\lambda > 0$ represents a diverging and unstable result, $\lambda < 0$ ensures a stable converged state, hence, $\lambda = 0$ is used as a threshold for distinguishing the successful control from the failed ones.

3.3 Results & Discussion

3.3.1 Free hovering state of bumblebee

Achieving a trimmed hovering state is essential before applying control models. As described in previous section that the CM is determined through a prescribed simulation to meet the requirement of torque balance. The result of a free flight simulation is shown in Figure 3–2(e,f). The calculated time average of aerodynamic force $\bar{F}_z$ in vertical direction is equal to and $\bar{F}_x$ in horizontal direction is less than 4.0% of bumblebee weight, and the average torque is less than 0.3% of the maximum torque value, indicating a trimmed hovering state.

3.3.2 Validation for simplified model

To prove the effectiveness of the simplified model, three cases are simulated with our CFD solver with 1T delayed PD feedback control with control parameters being: case 1: (P_{ref}, D_{ref}), case 2: 2(P_{ref}, D_{ref}), case 3: 4(P_{ref}, D_{ref}). Case 1 indicate a weak control thus resulting in a slow converging pitch curve with single peak. Case 2 points to

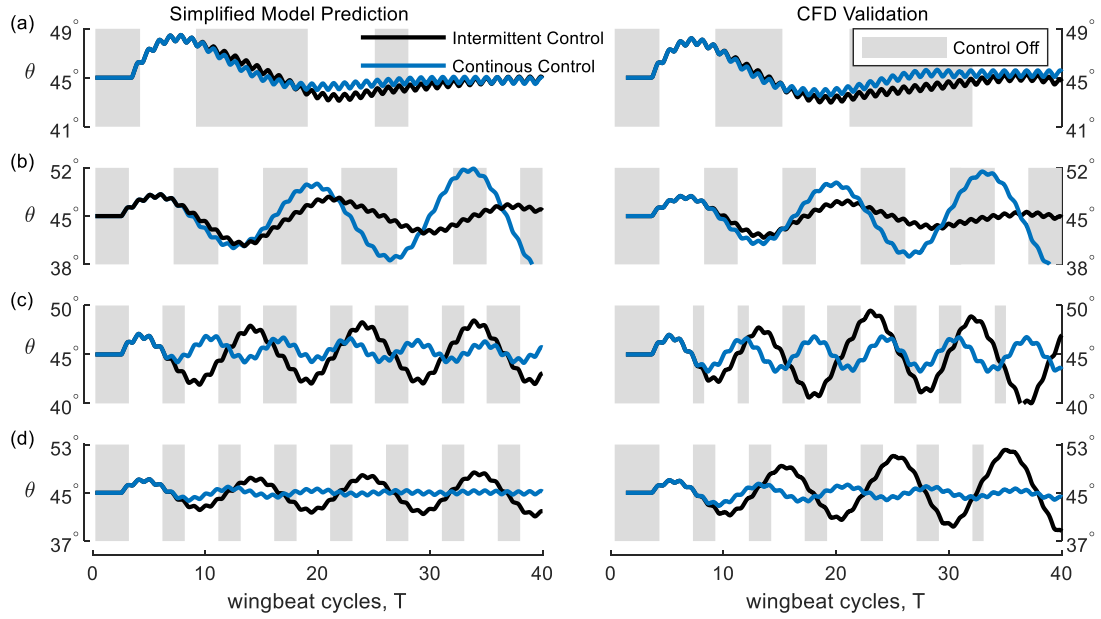

Figure 3–7 Characteristics of flight stabilization in continuous and intermittent control models. Time-varying pitch angle deviations are plotted and compared between intermittent control (black solid line) and continuous PD control (blue solid line) in four cases, (a) with control parameters (P_{ref}, D_{ref}), (b) $(3.33P_{ref}, D_{ref})$, (c)$(P_{ref}, 4D_{ref})$ (d) $(3P_{ref}, 3D_{ref})$, under 1T delay and an initial angular velocity perturbation, $\omega_0 = 180^{\circ}s^{-1}$. Gray shaded areas represent the cycles when control is off based on equations (6)–(8).

a relatively moderate control which results in slight overshoot and rapid damping. Case 3 indicates a failed strong control action which is featured by an oscillatory diverging pitch curve(Figure 3–6(a)). The initial perturbation is an angular velocity perturbation of $\omega_{ini} = 180^{\circ}s^{-1}$ The simplified model results are compared with CFD results in Figure 3–6. The root-mean-square(RMS) of the angle difference between the CFD and the simplified model are 0.58°, 0.27°, 2.06° for three cases separately. The basic trend and the magnitude of the first two cases are well predicted, while the discrepancy in case 3 may arise from the fact that the translational velocity induced aerodynamic torque is not considered in our simplified model, as reported in a computational study of fruit fly[68]. However, the predicted pitch of case 3 still captures the oscillatory diverging behavior.

From three validation cases, it is known that the simplified model can provide reasonable prediction, it can also be proved through some dimensional analysis. As mentioned in Sun[90], the non-dimensional aerodynamic derivative of bumblebee translating horizontally is $M_u = 2.38$. The maximum translation speed can be predicted through

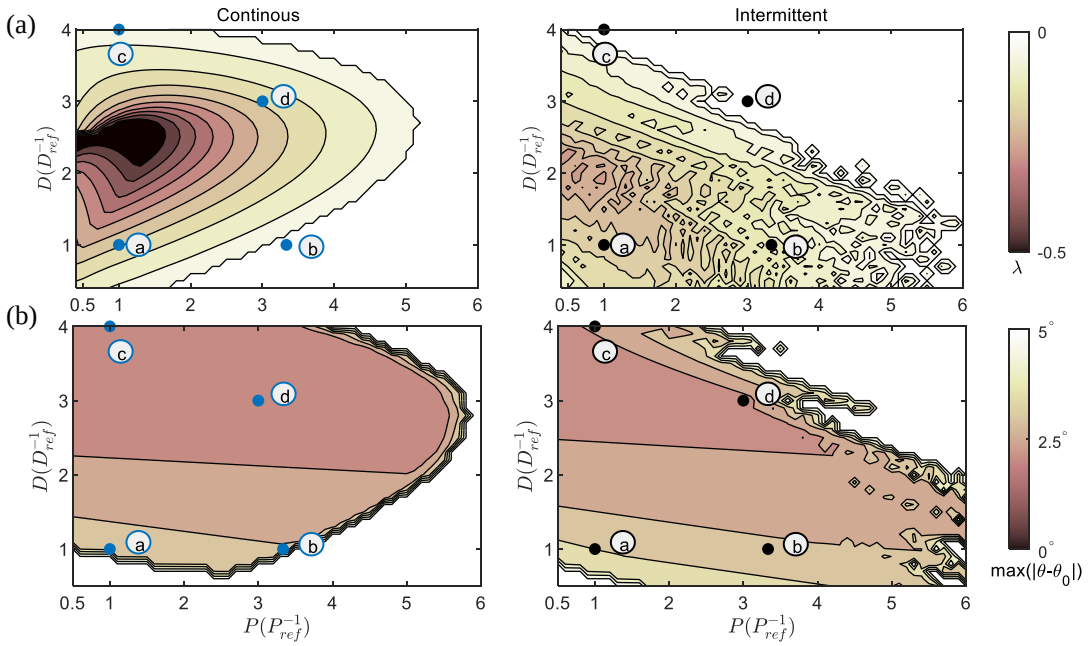

Figure 3–8 Characteristics of flight stabilization in continuous and intermittent control models.(a) Contours of convergence ratio λ in terms of PD control parameters in comparison between continuous (left) and intermittent (right) control strategies among the four cases in Figure 3–7 (a)–(d). Note that the white regions with $\lambda > 0$ point to diverged controls. (b) Contours of the maximum deviation angle, $max(|\theta - \theta_0|)$ under perturbation in terms of PD control parameters in comparison between continuous (left) and intermittent (right) control strategies among the four cases, with the unsuccessful controls having deviation angle larger than 5˚ (white region).

$v_x = \int_{0T}^{10T} sin\theta g dt \approx \frac{1}{2} sin\theta g 10T$. With θ assumes to be around 5˚, the non-dimensional aerodynamic torque induced by translation velocity is in the order of $10^{-2} \sim 10^{-3}$, while the action torque due to pitch deviation is in the order of 10^{-1}. Thus, action torque is dominants the pitch results with seldom influence from translation motion. In diverging cases as case 3 in Figure 3–6, the state variable deviation is larger even over 5˚, making the translation motion effect in-negligible, whereas, the diverging trend is still well captured by our simplified model.

3.3.3 The stabilization robustness comparison between intermittent and continuous control

The comparison between the simplified model and CFD result, as well as the prediction and corresponding validation results are shown in Figure 3–7 & 3–8. The stabi-

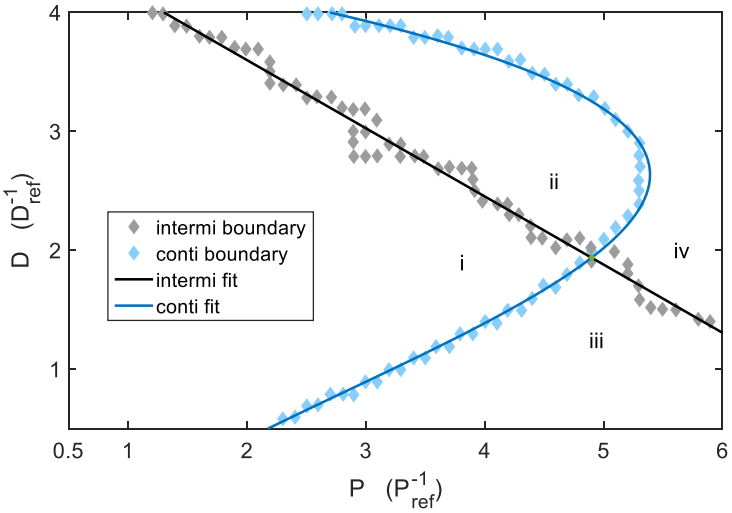

Figure 3–9 Convergence boundaries of intermittent and continuous control models at $\lambda = 0$ of Figure 3–8(a). Model-based results are marked with dots while fitted by a linear regression, $D = -0.5733P + 4.7469$ for the intermittent model, and a third-order polynomial, $P = -0.2115D^3 + 0.5157D^2 + 1.6893D + 1.2297$ for continuous one, respectively (PD are nondimensionalized). The intersection point $P = 4.902$, $D = 1.939$. There exist 4 zones, i, ii, iii, iv, with an intersection of $P = 4.902$, $D = 1.939$.

lization robustness of bumblebee pitch control is investigated by applying different combinations of control parameters (control parameter sensitivity analysis) from a range of $(0.5, 6)P_{ref}$, $(0.5, 4)D_{ref}$, with an interval of $0.1P_{ref}$, $0.1D_{ref}$ separately. Hence in total 1925(55×35) cases are simulated with simplified model. The empirical parameter $\alpha = 0.02$ to allow for more open-loop controls. The initial angular velocity perturbation is $\omega_{ini} = 180^{\circ}s^{-1}$, and the pitch control results are fitted with Equation 3–21 with proper initial conditions, and the resulting convergence ratio λ and maximum pitch deviation $max(|\theta(t) - \theta_0|)$ are plotted and compared in Figure 3–8 (a)(b). Within 1925 cases, four representatives are chosen for validation marked as ⓐ,ⓑ,ⓒ,ⓓ as in sub-figures (a)-(d). The validation cases locate around the boundaries of the convergence threshold value ($\lambda = 0$) to cover a broad range of control parameters. The validations shows that the simplified model is a reasonable prediction for the controlled results.

From the convergence ratio map comparison between intermittent control and continuous control, it is apparent that there exist four typical zones represented by i, ii, iii, iv as in Figure 3–9. The four zones are based on the boundaries of the convergence ratio map in Figure 3–8(a). In particular, i denotes the common robust region overlap be-

tween intermittent control and continuous control, while ii denotes an angular-velocity-dominant region since ii locates in large D region, and iii denotes an angular-dominant region where P feedback dominants the control results. iv is a region that the stabilization of both intermittent control and continuous control cannot be achieved. Intermittent control apparently outperforms continuous control in the angular-dominant region with a representative case ⓑ, however continuous control wins over intermittent control in angular-velocity-dominant region iv, and case ⓓ is as an representation. The pitch angle deviation contour (Figure 3–8(b)) can approximately cover the robust region in convergence ratio separately, thus the results are consistent.

The reason that intermittent control can outperform continuous control in angular-dominant region is that: with large P, the even small angle deviation can lead to large control action which is further amplified by the sensory delay, thus, with intermittent conditions turning off the control actions from time to time, the overshooting trend is modified to be converging. The branch point between intermittent control and continuous control locates one to two cycles after the first pitch peak is achieved (Figure 3–7(b)), and the feedback of pitch deviation is large due to sensory delay, hence a strong control action is induced in continuous control due to large P and easily leading to overshoot. However, the feedback of intermittent control is with $\Delta\theta(t-nT)\Delta\omega(t-nT) < 0$, therefore control is 'OFF', and pitch is dominated by damping. In the angular-velocity-dominant region, the sensitivity regarding angular velocity is increased thus resulting in smaller pitch peak during the first few cycles (Figure 3–7(d)), while the strong control action induced by large P and D will cause larger pitch angular velocity where without high sensitivity regarding angular velocity a successful control cannot be achieved. To prevent system from overshoot, either reducing the cycles of control actions or obtaining higher sensitivity regarding angular velocity can both help, and intermittent control outperforms in iii region through inhibiting the control, while continuous control outperforms in ii region through the latter way by obtaining a large angular velocity gain D.

3.3.4 Sensitivity analysis regarding sensory delay

The sensory delay of bumblebee is estimated to be around 1∼2 wing beat cycles[96-97]. While only 1T delay is assumed in previous section, in this section, 2T delay is considered for comparison between intermittent control and continuous control. The convergence maps of two control models with initial angular perturbation $\omega_{ini} = 180^{\circ}s^{-1}$

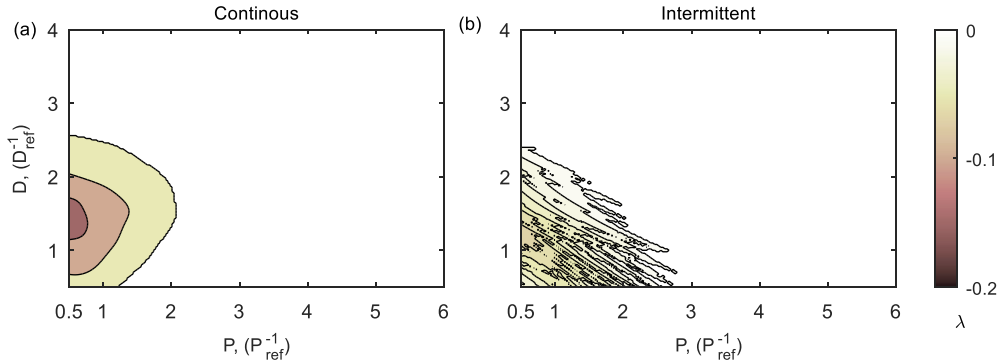

Figure 3–10 Contours of convergence ratio λ in terms of PD control parameters in comparison between continuous (a) and intermittent (b) control strategies with 2T delay and initial angular velocity disturbance, $\omega_{ini} = 180^{\circ}s^{-1}$, obtained from simplified model.

are depicted in Figure 3–10. Rather than focusing on the short-term pitch deviation, it's more significant to investigate the long tern convergence ratio.

From Figure 3–10 it is apparent that the robust region shrinks significantly with the increase of sensory delay compared with Figure 3–8. This is consistent with the Figure 3–5 that with the increase of sensory delay (Δt) the closed-loop time constant basically increases compared with short delay region which indicates that the equilibrium state requires longer time to be achieved, thus the stabilization robust region should also shrink.

3.3.5 Sensitivity analysis regarding initial perturbation amplitude

How intermittent/continuous control respond to the change of initial perturbation is investigated in this section. The perturbation amplitude is changed from 0.5, 1, to 2 times the original amplitude $\omega_{ini} = 180^{\circ}s^{-1}$. To study the effect of initial perturbation amplitude change in angular dominant region, the control parameters are chosen to be $(3.33P_{ref}, D_{ref})$. The results from simplified model are illustrated in Figure 3–11, where for all three amplitudes the intermittent control outperforms continuous case. The intermittent control with almost half of all the cycles to be open-loops is still able to result in satisfactory converging results, while in continuous control three cases all result in oscillatory non-converging pitch curve. $360^{\circ}s^{-1}$ is still small perturbation compared with the angular velocity which can be achieved by stalk-eyed fly or fruit fly ($\sim 1700^{\circ}s^{-1}$) or that of hawk moth ($\sim 800^{\circ}s^{-1}$)[89]. Therefore, it can be concluded that in small perturbation region, intermittent control outperforms continuous control in angular dominant region.

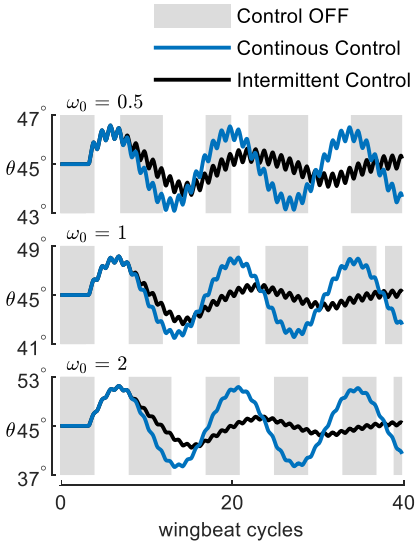

Figure 3–11 Effects of initial disturbance amplitude on stabilization robustness: intermittent control(black solid line) and continuous control (blue solid line) with 1T delay and initial disturbance amplitude $\omega_{ini} = 90^{\circ}s^{-1}, 180^{\circ}s^{-1}, 360^{\circ}s^{-1}$ separately.

When perturbation becomes larger, usually nonlinear control behavior arises, which is out of the scope of current assumption that bumblebee adopts simple PD control.

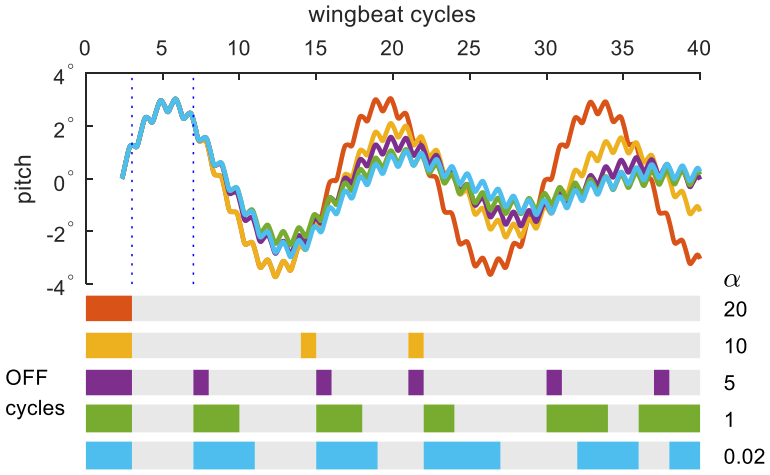

Figure 3–12 α effects on pitch angle control with $(3.33P_{ref}, D_{ref})$,and α ranging from 0.02 to 20. Color shades (red, yellow, purple, green and blue) represent the intervals of OFF control corresponding to the pitch curves.Initial angular velocity perturbation is $\omega_{ini} = 180^{\circ}s^{-1}$.

3.3.6 Sensitivity analysis regarding α

The empirical parameter defined above alternate the control system between open-loop cycles and closed-loop cycles. Hence the change of α will greatly change the system response towards disturbances. From above sections it's known that intermittent control with certain conditions can enhance the stabilization robustness in angular-dominant region. To determine whether this merit is highly related with α or not, a sensitivity analysis regarding α is conducted with control parameter combination $(3.33P_{ref}, 1.0D_{ref})$. The α ranges from 0.02 to 20 which covers both the intermittent and continuous control. When $\alpha = 0.02$, as shown in Figure 3–12 the number of open-loop cycles is maximized, while $\alpha = 20$ corresponds to continuous control with no open-loop cycles during control. And from the upper panel of Figure 3–12, it can be seen that with the increase of α the controlled pitch curve gradually converge to continuous control result with an oscillating pitching. Except for α being 20, all the other cases shows an obvious trend of converging which indicate a better performance over continuous control.

Our results show that the advantage of intermittent control in angular-dominant region is preserved even when α ranges from several overs orders of magnitude from 0.02 to 20. And the feature that α can change the control behavior give us a hint that by adjusting the α in angular and angular-dominant region, the control system is able to obtain both the stabilized region in angular-dominant zone as well as in angular-velocity dominant zone with α in the following Equation 3–22, where k_0 represents the slope of the intersection point of intermittent control and continuous control robust region boundaries in Figure 3–9.

$$\alpha = \begin{cases} \infty & if \frac{D}{P} > k_0 \\ 0.02 & if \frac{D}{P} \leq k_0 \end{cases} \tag{3–22}$$

The intermittent control model we proposed shows adaptive benefit regarding stabilization robustness simply by adjusting α without any change in wing-body morphology. The stabilization robust region can extend to the summation of all robust region of each α, while how this can be implemented in insect control system remains to be discussed.Furthermore, it should be notified that even though the basalare muscle (b1, b2) spikes pattern provide us with a perspective of possible existence of intermittent control, the direct evidence of correlation between spike and control reaction remains to be found.

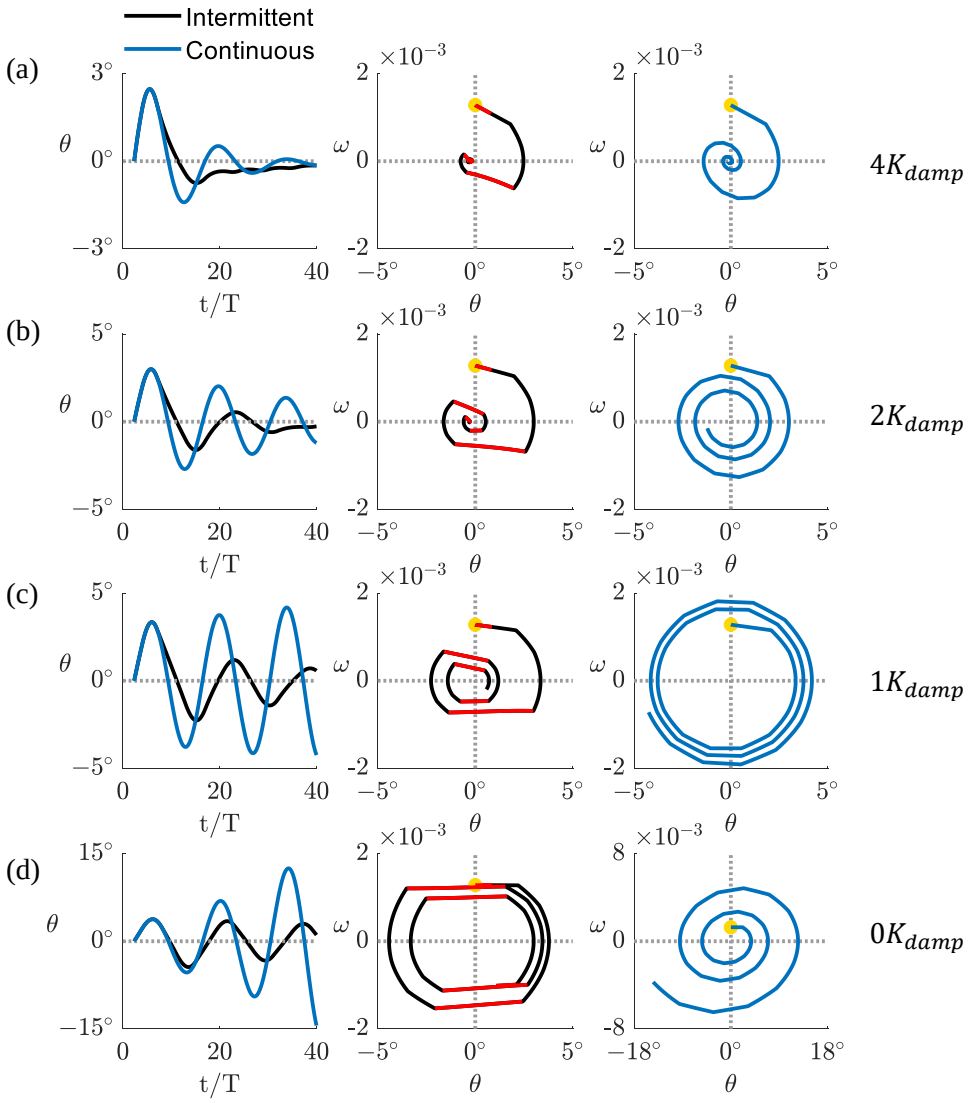

Figure 3–13 Time history of pitch angle and phase portrait via K_{damp} in 40 wingbeat cycles of intermittent (black solid line) and continuous control (blue solid line) with control parameters of $(3.33P_{ref}, D_{ref})$. In the phase portraits, the intermittent control OFF phase is marked with red solid line and the starting point is marked as a yellow-coloured filled circle in phase portrait. K_{damp} are set to be: (a)$4K_{damp}$,(b)$2K_{damp}$,(c)$1K_{damp}$ and (d) $0K_{damp}$. Note that, to get a clearer phase portrait, T_{cylic} is not taken into account in the phase portraits so as to ensure an apparent converging trajectory. The yellow point marks the initial state.

3.3.7 Sensitivity analysis regarding K_{damp}

To show that the benefit of intermittent control is not highly dependent on system parameters, the system damping parameter K_{damp} is inspected on as an example in Figure 3–13 with control parameter combination ($3.33P_{ref}$, D_{ref}). The damping coefficient is changed from zero to four times the original system damping coefficient to see how K_{damp} affects the control results. Phase portrait is adopted in illustrating the ON, OFF control in Figure 3–13 in the middle panel. Note that the cyclic oscillation T_{cyclic} is eliminated here to give a clearer phase portrait, thus Figure 3–13 (c) pitch curve is a bit different from the case with T_{cyclic} in Figure 3–11. With the increase of damping coefficient, the pitch curve converges faster which is consistent with the result in Figure 3–5 that when damping coefficient is increased for three times, the allowable range for successful control τ_c extended to the small ratio region, i.e. $\frac{D}{P}$ is allowed to be smaller to ensure a successful control.

The OFF controls in intermittent control correspond to a short red straight line in the phase portrait of Figure 3–13, the damping coefficient is reflected on the slope of the straight line segment that with higher damping coefficient the slope is steeper hence converges faster to the equilibrium point. When there exist no damping, the phase portrait in state space is unstable and diverging for continuous control. The existence of damping coefficient ensures a asymptotically stable result for intermittent control. While in delayed PD feedback control, the phase portrait winds its way around equilibrium point, and easily diverging for both $0K_{damp}$ and $1K_{damp}$, intermittent OFF loops shortens the path towards equilibrium hence give better results than continuous control for all four cases. Therefore, it can be concluded that intermittent control's benefit in angular dominant region is preserved with damping coefficient changed within certain region. For bumblebee roll& yaw control, the damping dominated by flapping-counter-torque indicates a larger K_{damp}. Because the possible extension of intermittent control in large damping region, the merit of intermittent control may also be applied to roll and yaw which is our future task to explore.

3.3.8 Other intermittent conditions

Bang-bang control is another typical intermittent control method which is widely applied in home appliances such as the air-conditioner. Bang-Bang & Bang-off-Bang control can be treated as a highly simplified version of intermittent control, which nor-

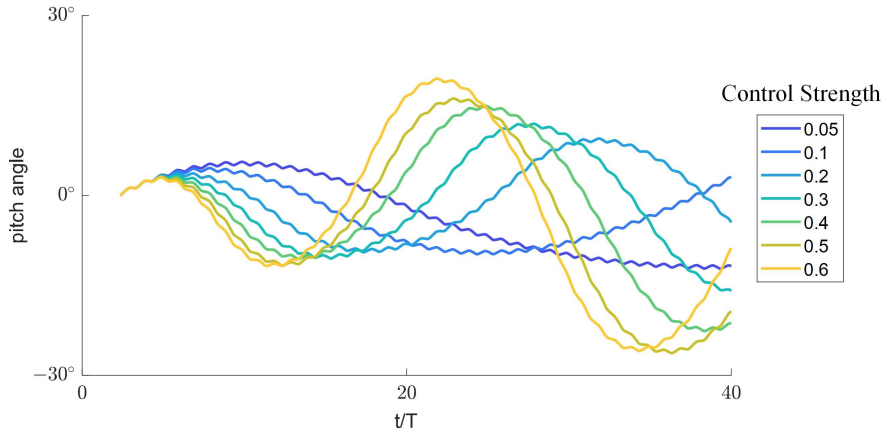

Figure 3–14 Pitch curves under Bang-Bang control with same initial angular perturbation $\omega_0 = 180^{\circ}s^{-1}$ and one-cycle delay. Non-dimensional control strengths range from 0.05 to 0.6. All the control curves are diverging with the maximum deviation angles much greater than those by the PD based intermittent control method.

mally works via an action change between limited states (usually two states), as often seen being utilized in temperature control. This control strategy is also proposed for airfoil's roll control, yet the control duration lasts around 1.2 second for control action[99]. While the Bang-Bang control relies on a slow state change characteristic, easily leading to an oscillatory behavior, the intermittent strategy/system proposed here is sensitive to angle deviation, easily getting diverged due to weak damping in pitching direction. Things even get worse when it comes to time-delayed Bang-Bang control, which is obviously lacking robustness. As shown below, a possible Bang-Bang condition is proposed as in Equation 3–23, no control action was found working successfully in terms of flight stabilization (Figure 3–14). On the other hand, there may exist a possibility that the Bang-Bang control could work under other conditions, which needs to be explored in future.

$$\begin{cases} \Delta\theta(t-nT) < -0.5^{\circ} & control\ action + \\ -0.5^{\circ} \leq \Delta\theta(t-nT) \leq 0.5^{\circ} & control\ action\ 0 \\ \Delta\theta(t-nT) > 0.5^{\circ} & control\ action - \end{cases} \tag{3–23}$$

The intermittent control conditions in Equation 3–9 and Bang-bang conditions belong to a type of sliding-mode-control method with certain physical meaning, where the sliding mode control achieves equilibrium even in unstable systems with proper switching conditions for control.

3.4 Concluding Remarks

In the current study, we proposed an intermittent control model inspired by the intermittent spiking characteristic in insect steering muscle $b1, b2$, which is implemented with a PD model with open-loops determined by certain conditions. We showed that compared with the continuous model in conventional study, intermittent control outperforms continuous ones in angular-dominant region, which is independent of sensory delay, initial perturbation amplitude within certain range. And intermittent control shows adaptive benefit in stabilizing the body posture by adjusting the empirical parameter α. Hence, the intermittent control model provides a possible explanation for insects' robust control, which is possibly able to unlock the interplay between the external mechanical system and the internal control system. While more biological evidence proving the direct correlation of muscle spike and wing kinematic alteration still needs to be find. To note that the intermittent condition proposed in this study is just one alternative, other intermittent conditions such as the bang-bang control or intermittent control with system-matched hold remains to be explored. Furthermore, our study may provide a novel bio-inspired design for a robust flapping-micro-air-vehicle control system.

Chapter 4 The kinematic intelligence of the beetle upright takeoff

4.1 Introduction

Takeoff is the first step for insect to take to the air. A force larger than the gravity is needed for the body acceleration during the takeoff either through extra leg thrust[100-101], increased wingbeat frequency and/or larger stroking amplitude[13, 102]. Ground proximity is common in landing and takeoff. A few researches have been done on takeoff flights to study the ground effect such as the fruit fly[103], and proved that the ground effect is negligible compared with gravity. Whereas, the leg thrust on the contrary, plays an important role in the body acceleration or body posture adjustment. It is found that leg thrust takes up more than 90 percent of the total vertical force while wing is mainly used for generating pitch down torque to maintain body pitch posture in fruit fly[101], and the leg thrust is capable of adjusting body pitch posture in mosquitoes[100].

Insect can takeoff from many types of free surfaces, horizontal vertical and even inverted ones such as the houseflies. In natural environments, backward takeoff from branch is also a common phenomenon[104]. Damselfly and dragonfly perform upright backward takeoff by force-vectoring mechanism[104] since the stroke plane varies little[105]. The takeoff initial posture could be very different from the target state, which involves a smart coordination of body and wing kinematics in the successive flight. A large change in body posture during takeoff may share similar wing/body modulation with the escape maneuver[7-8, 14]. Escape maneuver may give some in-depth insight into the functional limits of animal locomotion capacity[8]. Maneuverability can be limited by several factors: the muscle mechanical power, the neural delay and the intrinsic morphology related parameters. It is known that the limitation of fruit fly maneuverability is the neural delay, while the muscle mechanical power limits the performance of hummingbird[26]. Though the voluntary takeoff flight may be far from touching the functional limits, it may shed some light upon the common wing/body modulation pattern.

In our experiment, the beetles take off with an almost upright body posture with back facing the target. Beetles have two pairs of wings:the elytron and hindwings where the hindwings are usually covered under elytron hence they are also called inner wings and

outter wings separately. Plenty of studies concentrate on the beetle hovering and forward flight kinematics especially the effect of elytra as well as the flexible wing effects on the aerodynamics[106-108]. Some beetles fly with the elytra closed, others flap the elytra along with the hindwings. It is known that the elytron is capable generating some lift force in forward flight or hovering, while still small compared with the lift generated by hindwings[108-109]. How elytra affect the maneuver of a beetle is seldomly discussed. Moreover, the ground takeoff of the rhinoceros beetle and potato beetle are studied and found that rhino-beetle takeoff without jumping[110] while legs may have some liftoff effect in potato beetles[111]. Both the studies concentrate on the ground takeoff, but in our study, we focus on the beetle upright takeoff from branch which hasn't been paid attention to. In this study, in order to understand the takeoff dynamics, we used two high speed cameras to record and reconstruct the wing body kinematics. And the corresponding CFD model is built to study the aerodynamics during takeoff. We intend to reveal how insects coordinate the wing and body kinematics in a vertical takeoff.

4.2 Methods

4.2.1 Experimental setup

Green chafer (*Anomala albopilosa*) sourced from wild in Chiba University (Japan) by ultraviolet light trap were used in our experiment. A flight chamber with cross-sectional dimension of 1m×1m and length of 2m which is sufficient for the aerobatic maneuver was adopted for the takeoff flight from branch.

Green chafers were filmed using two Photron high speed cameras with frame rate 1500 frame per second (fps), and shutter speed $\frac{1}{1000}s$. The recording was started manually by a remote trigger as a green chafer takes off from branch, the sequence of flapping preparation and body acceleration is captured until body locates four to five wing length away from the takeoff position (out of the camera view). No artificial markers are attached to insects which also ensures minimum external perturbation, while the head and tail points as well as wing & elytron hinge points serve as markers to determine insect posture. The experimental setup is illustrated in Figure 4–1. The UV light is used as a target which can attract insects and facilitates them to take off. To extract the wing kinematics during taking off, hindwing is regarded as single solid flat plate, and the forewing (elytron) which possess a 3D structure is digitized and regarded as non-deformable. Thus, the wing/ elytra kinematics can be described with three angles rotating relative to the hinge points,

realized through shape fitting.

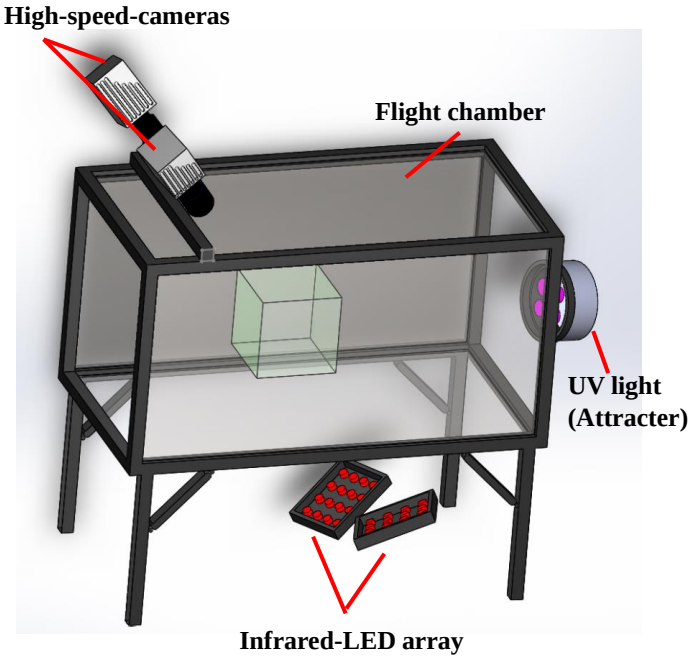

Figure 4–1 The SolidWorks representation for the experimental setup for beetle taking off flight. Two high-speed-cameras Photron are used, and a ultra-violet light is positioned in the front of the chamber to attract the beetles, and two infrared-LED lights are positioned opposite to the direction of high-speed cameras. The green chamber represent the effective flight sequence region.

Table 4–1 The parameters of a green chafer model

Insect	$f(Hz)$	$c_m(mm)$	R^{hind}_{wing}	R^{fore}_{elytra}	L_{body}	Φ_{amp}	$U_{ref}(m/s)$	Re
Green Chafer	69.26	8.53	21.97	13.5	20.39	181.82°	9.66	5492

4.2.2 The beetle parameters

The beetle body mass is taken as an average of 17 individuals which is 855.22mg. A realistic wing shape is used in our CFD simulation with hindwing length being 21.97mm, and the elytra length being 13.5mm. The morphological parameters are summarized in Table 4–1. Based on uniform density distribution assumption of body, the body moment of inertia is calculated to be 5.871×10^3 $mgmm^2$ (I_{xx}) around the body longitudinal axis, 2.0×10^4 $mgmm^2$ around body pitching axis (I_{yy}), and 2.19×10^4 $mgmm^2$ around z axis

(I_{zz}). The resulting mean wingtip velocity is 9.66m/s and the resulting Reynolds number during takeoff is around 5492.

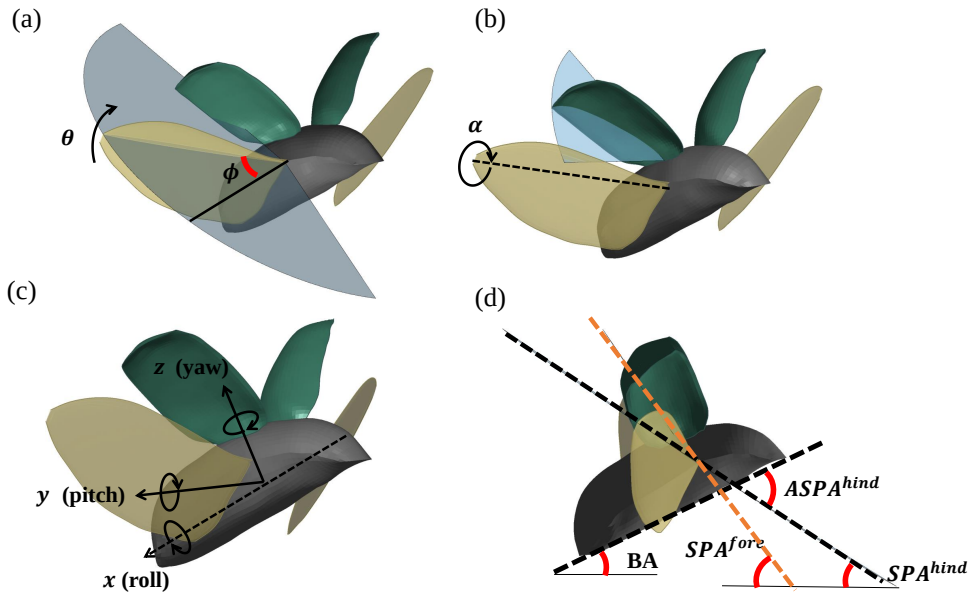

Figure 4–2 The wing-body geometric model of beetle and the corresponding anatomical stroke plane angle (ASPA) for elytron and wings separately.(a,b) The wing and/or elytron angle definition relative to the stroke planes. (c) The body frame coordinates and the corresponding angles to describe body posture. (d)The definition of ASPA, and body angle (BA) as well as stroke plane angle(SPA). The stroke plane of wing is represented by the black-dash line passing wing tip, and the stroke plane of elytron is represented by the orange-dashed line passing elytron tip.

4.2.3 Body & wing kinematics definition

To extract the wing kinematics during taking off, hindwing is regarded as single solid flat plate, and the fore-wing (elytron) which posse a 3D structure is digitized and regarded as non-deformable (Figure 4–3). Thus, the wing & elytron kinematics can be described with three angles rotating relative to the hinge points, realized through shape fitting(Figure 4–4). (Detailed procedures can be found in Appendix A.4) The body kinematics are defined by three angles in an order of yaw-pitch-roll relative to the ground frame to describe the current body posture, however, when it comes to the body angle change, the angles are defined relative to the body initial posture to reflect the angle change better (Figure 4–2 (c)). The wing kinematics are defined by three angles relative to the stroke plane (SP): wing positional angle (ϕ), elevation angle (θ) and feathering

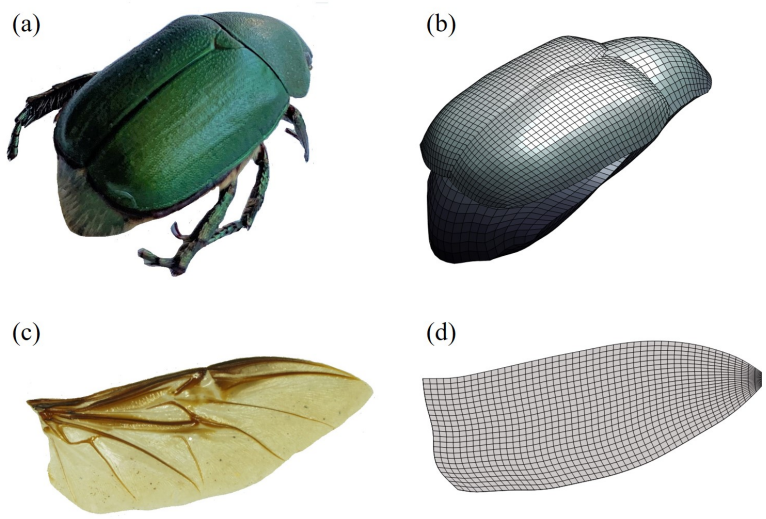

Figure 4–3 (a,c)The green chafer and the wing morphology, (b,d) the corresponding inner layer of grid used in computation.

angle (α). Figure 4–2 gives an illustration of the geometric model of green chafer with a body, two elytra (fore wings) and two hindwings based on realistic shape.

The body angular velocity can be expressed as Equation 4–1

$$\vec{\omega} = \vec{z}_0 \frac{dyaw}{dt} + \vec{y}_1 \frac{dpitch}{dt} + \vec{x}_3 \frac{droll}{dt} \tag{4–1}$$

where the $x_0 y_0 z_0$ represent initial posture frame, $x_3 y_3 z_3$ represents the final frame rotated in an order of yaw-pitch-roll. The angular velocity in final body frame can be expressed as(Equation 4–2):

$$\vec{\omega} = \begin{bmatrix} -sin(pitch)\frac{dyaw}{dt} + \frac{droll}{dt} \\ cos(pitch)sin(roll)\frac{dyaw}{dt} + cos(roll)\frac{dpitch}{dt} \\ cos(pitch)cos(roll)\frac{dyaw}{dt} - sin(roll)\frac{dpitch}{dt} \end{bmatrix} \tag{4–2}$$

4.2.4 The fluid dynamics solver

Our in-house flight solver is a fortified Finite-Volume-Method-based Navier Stock solver with dynamically moving multi-blocks and overset-grid system[52]. The geometric models of body elytron and wing grids are generated according to the measured shapes. The grid numbers are 41x41x15 for elytron, 45x45x15 for body, 45x51x15 for hind-wing and 104x104x84 for the background grid. The details of the grids are shown in

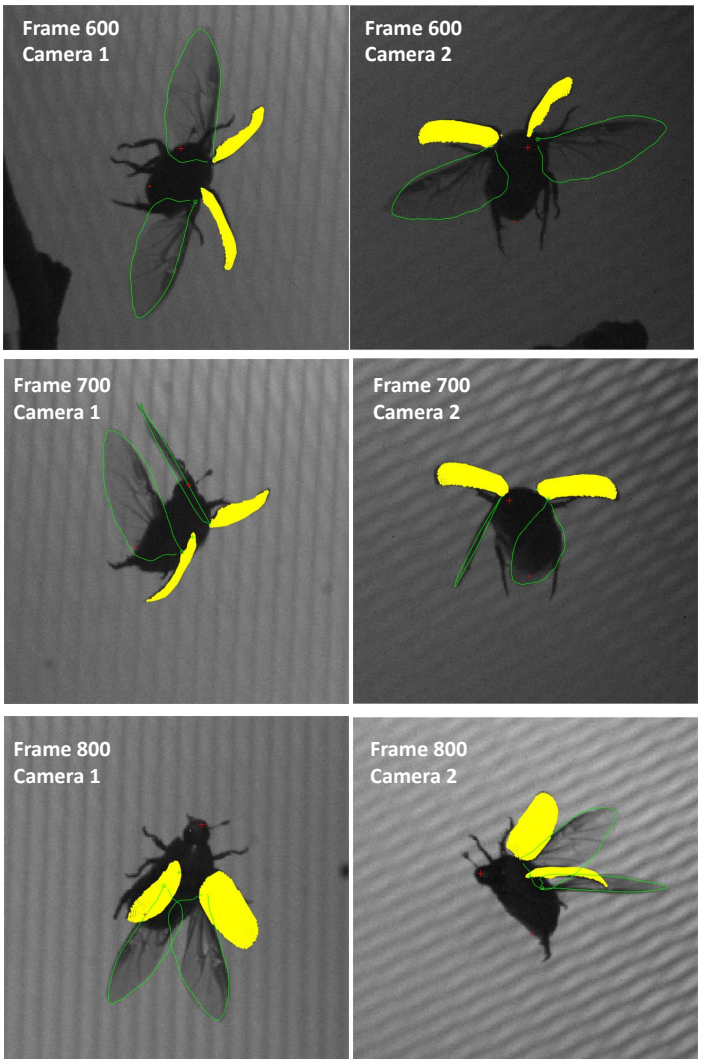

Figure 4–4 The shape fitting of elytra and hindwings examples at from two camera views simultaneously and at different frames. The insect centroid of body is always placed in the center of the image

Figure 4–5. To avoid the nonphysical overlap between fore & hind wing grid, two models are established for simulation: body-wing model (excluded the elytra), the other one body-elytron model (excluded the hindwings). To note that the interaction between elytra and hindwings are ignored in this study. The CM position of insect model travels in a prescribed trajectory measured from experiment, as well as the wing kinematics in the simulation, and the corresponding aerodynamic forces and torques can be obtained.

The Reynolds number in the flow solver is defined as Equation 4–4 where the U_{ref} (Equation 4–3) represent the average wingtip velocity and ν is the kinematic viscosity of

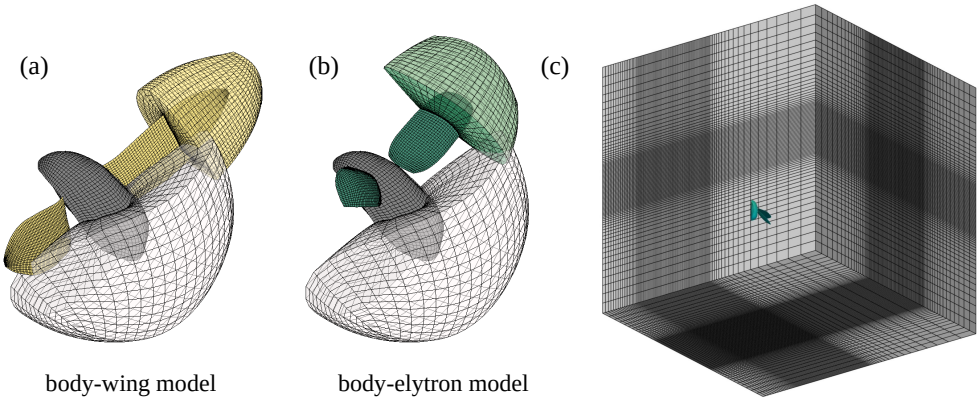

Figure 4–5 The computational grid illustration of the background, hindwing elytron and body (a) the body-wing model which excluded the elytra. (b) the body-elytron model excluding hindwings.(c) is a perspective of the assembled grid in simulation.

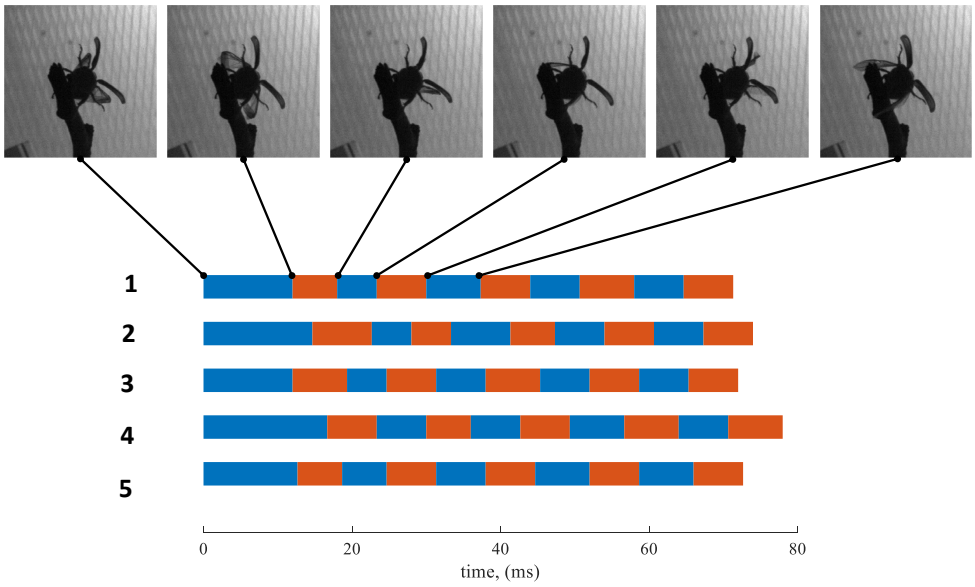

Figure 4–6 The takeoff preparation time segmentation of five different takeoff sequences. The flight sequences are aligned according to the starting point of the first downstroke with half folded wing. Blue region denotes the downstroke period, and the orange region denotes the upstroke period. The upper panel gives an example of the hindwing & elytra position during taking off in the first three wingbeat cycles.

air ($1.5 \times 10^{-5} m^2 s^{-1}$).

$$U_{ref} = 2\Phi_{amp} R_{wing}^{hind} f \tag{4–3}$$

$$Re = \frac{U_{ref} c_m}{\nu} \tag{4–4}$$

4.3 Results & Discussions

4.3.1 The takeoff preparation

With the elytra open and hindwing elevated, the flight sequence starts with a downstroke which lasts $10 \sim 20ms$ and then an upstroke which almost reaches the normal flapping speed as a slow forward flight. The following up/down strokes aim at extending the hindwing by inertial effect as well as the bio-fluid within vein structure, which is also called as the wing expansion phase[111]. Then the wing is fully extended after around 3 wingbeat cycles as shown in Figure 4–6. Apart from the duration of the first downstroke, the following up/downstrokes have similar duration, probably due to the thorax resonance oscillation after the first muscle twitch in the first downstroke. And the leg-detach from the branch are often observed to be around the 4^{th} to the 5^{th} wingbeat cycle, which is close to the non-jumping takeoff of the rhinoceros beetle[110].

4.3.2 The body kinematics during takeoff

Green chafer clings on a branch with the target ultraviolet light on behind during a typical taking off. Soon after their legs are detached from branch, wing flaps asymmetrically leading to a large rolling torque that initiate the body rolling up to more than 100 degrees while other angles changes are small relative to the initial posture as shown in Figure 4–7. The detailed body kinematics are illustrated in Figure 4–8 for 8 flight sequences, including the roll pitch yaw and body trajectories. The body roll pitch yaw angles relative to the initial body posture are plotted in Figure 4–7. The roll angle change is the largest ($\sim 120^\circ$) compared with the other two angles ($\sim 40^\circ$). Beetle ' s body longitudinal axis is almost vertical to the ground at initial instant, with the back against the target light. When stimulated by the UV light, beetle adjusts the body pitch and yaw angles to tilt the body longitudinal axis towards the target light, in the meanwhile body rolls around the longitudinal axis to face the target light. According to Figure 4–9, the main velocity component v_y seldom decreases during the whole flight sequence, indicating an effective transition

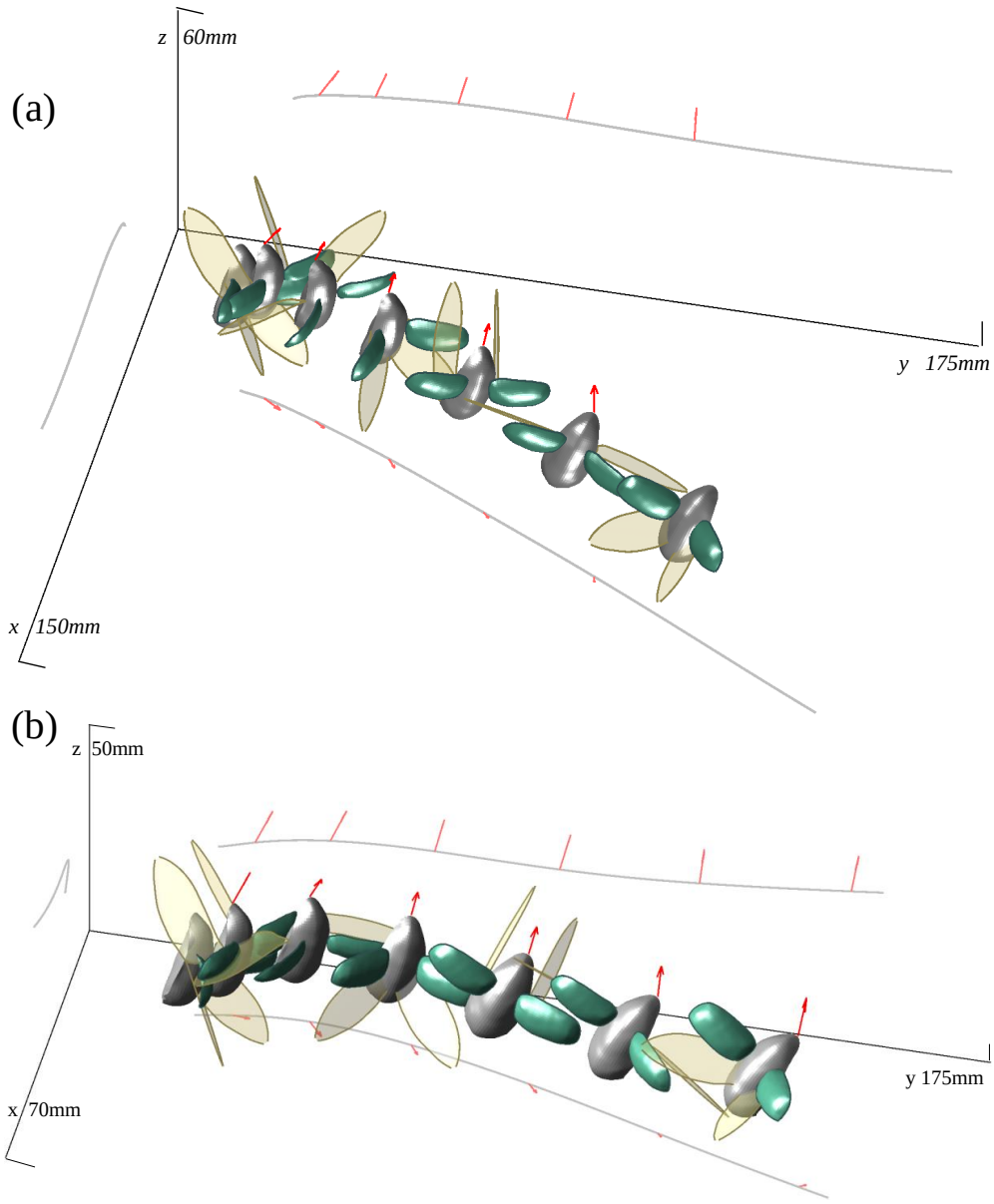

Figure 4–7 Sequential sketches of two different takeoff trajectories. The projections of CM position are represented with gray lines, and the cyclic average of aerodynamic forces are illustrated with red arrows originating from head point. Sub-figures (a)(b) correspond to the data 6 and data 7 in Figure 4–8 separately.

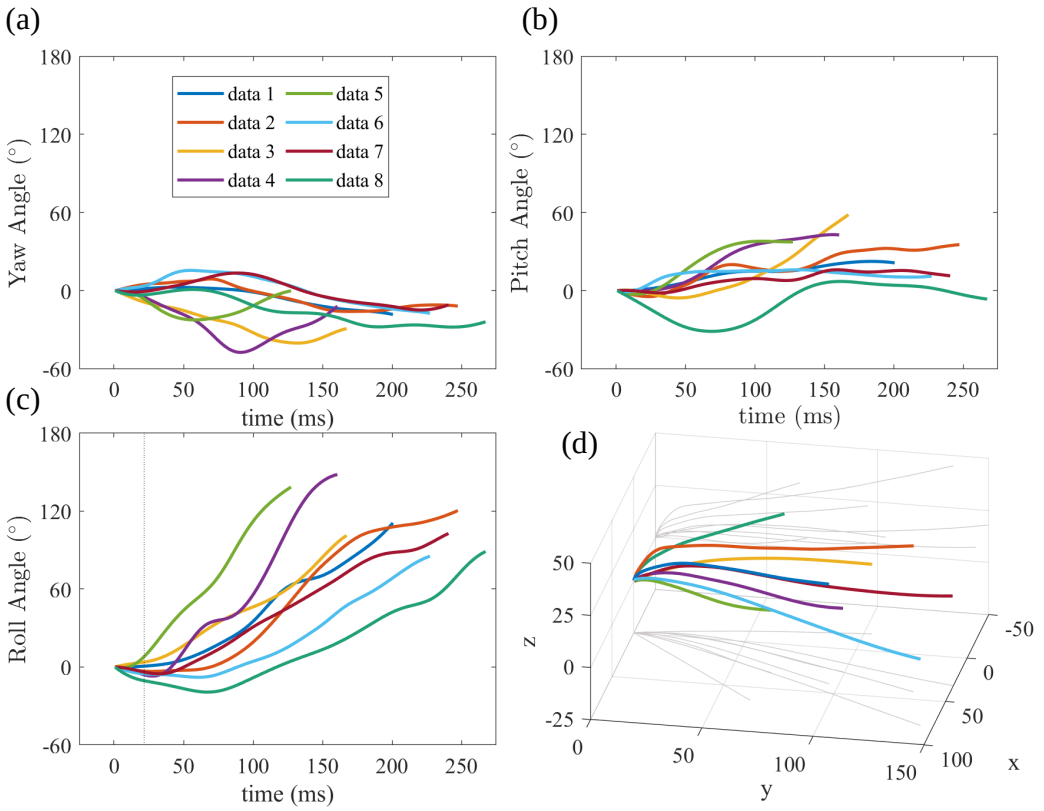

Figure 4–8 (a)(b)(c) represent the body yaw, pitch, roll angles relative to the initial body posture during takeoff respectively. And the corresponding CM positions relative to the initial point are plotted in (d) with their projections denoted in grey lines. The data are digitized 1.5 wingbeat cycle before legs are seen detached from the branch, the time of detach is marked as a black dotted line in (c).

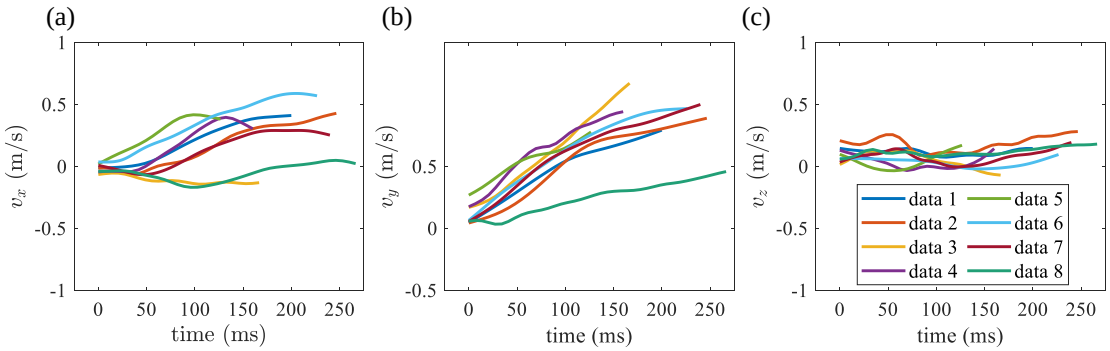

Figure 4–9 The body translational velocities in xyz directions during takeoff.

of the momentum. The body kinematics ensures a smooth transition between the initial backward and final forward posture which resembles the hummingbird escape pitch-and-roll maneuver[8, 14] only that the pitch angle of beetle is small because the takeoff is a relatively slow process, and it does not overshoot. The roll dominant takeoff can not only reorient the flight direction, but also preserves the translational momentum without a significant loss.

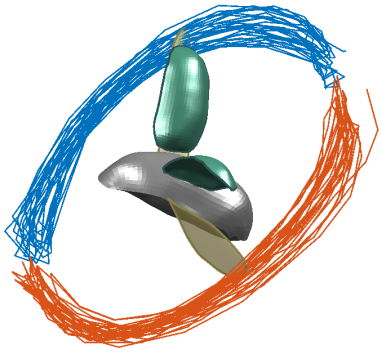

Figure 4–10 A representative of the measured wingtip trajectories of left wing (red) and right wing (blue) in body frame during takeoff (data 6).

4.3.3 The effects of leg thrust

The body velocities in Figure 4–9 are very small at initial instant since legs are still attached to the branch. Leg thrust leads to a small initial backward and vertical velocity. The main velocity component is along the y axis directing away from the start point, which gradually accelerate to around 1m/s in 200ms due to aerodynamic force component in the y direction. Though leg thrust may contribute to small initial body translational velocity, the thrust induced torque is very small and may not benefit for the roll dominant takeoff as can be seen in Figure 4–8(c). The turning point of roll lies somewhere between 30 50ms when legs are observed to be detached from the branch except for data 5, indicating the rolling torque is dominated by aerodynamic torque instead of leg thrust induced torque. Data 5 flight sequence starts from different initial body posture from other datasets, in other datasets insects cling vertically on a branch with the back facing the UV light while in data 5 insect faces the target light with its side. Though with different initial body posture, the takeoff sequences still share similar characteristic in three body angles.

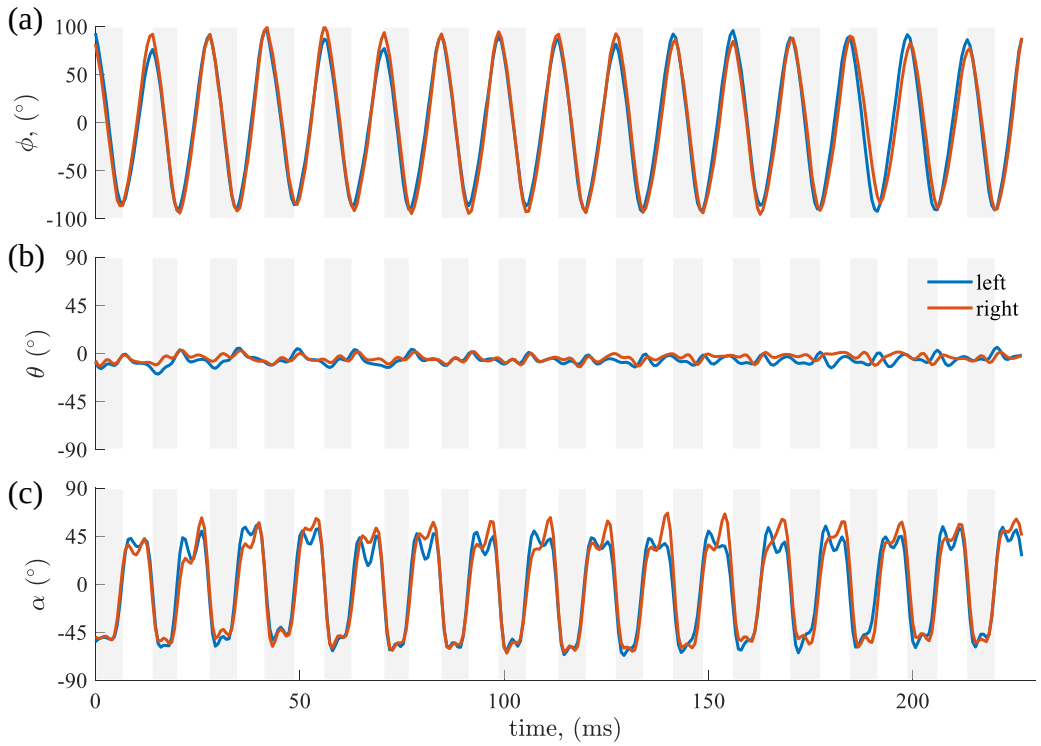

Figure 4–11 The wing kinematics during taking off sequence of data 6 (Figure 4–8) ϕ, θ, α represent the positional angle around x axis, the elevation angle around z axis and feathering angle around y axis relative to the stroke plane separately. Down strokes are patched in grey.

4.3.4 Wing kinematics in takeoff control

The anatomical stroke plane angle (ASPA) of fore wing and hindwing during takeoff is almost fixed ($ASPA^{hind} = 58.0^{\circ}$) throughout the whole flight sequence even though with such big variation in flight pattern as well as body posture as shown in Figure 4–10, which may indicate a biological constraint of green chafer. Whereas, a hawk moth is able to change the ASPA in pitch maneuver[112]. The detailed wing kinematics are digitized for data 6 (Figure 4–11), where the hindwing ASPA is fitted to be 58.0° and the elytra ASPA is 80.6°. The wing stroke amplitude is around 180° during takeoff, similar to that of the rhinoceros beetles[106, 108]. The feathering angle amplitude is smaller in the first few cycles i.e., larger geometric angle of attack, thus the aerodynamic force should be higher which is further proved in Figure 11. Since green chafer takeoff is asymmetric, leading to asymmetric wing kinematics especially for positional angle ($\Delta\phi \sim 15^{\circ}$) and feathering angle ($\Delta\alpha \sim 20^{\circ}$). The elevation angle change is relatively small, since the

wing tip trajectory does not deviate much from the stroke plane as shown in Figure 4–8.

As a comparison, the beetle forward flight with velocity $1.2m/s$ is also digitized. The elytra and wing kinematics are in Figure 4–12. The hindwing flapping amplitude is over 4 times the amplitude of elytron, and the stroke reversal of hindwing almost coincide with that of elytron (Figure 4–12). The body pitch during forward flight is 28.9° and the stroke plane angle is 29.1° for hindwing and 51.7° for elytron, resulting in an ASPA of 59.0° for hindwing and 80.6° for elytron. Compared with ASPA fitted in takeoff flight, it can be found that there is seldom difference in ASPA of the hindwings. The wing beat frequency of slow forward flight ($v = 1.2m/s$) is 69.26Hz, and the average frequency of the takeoff sequence is 70.3Hz. Because the wing beat frequencies of forward flight and takeoff are from different individuals, there may exist small difference. It can be concluded that the wing beat frequency in slow forward flight and takeoff flight does not have much difference. The wing beat frequency of the former half (7 wing beat cycles) is averaged to 70.47Hz, while the latter half is averaged to 70.0Hz. Hence it may indicate a relatively faster wing beat frequency soon after leg detached from branch than the later wing beats. The wing stroke amplitude as well as the feathering angle amplitude does not have significant difference with that of the average of takeoff flights, though the amplitudes are changed from cycle to cycle.

The opened elytron which would not restrain the wing flapping is probably one of the reasons that the wings flap at large amplitude almost 180° compared with the closed elytra beetles.

4.3.5 The aerodynamics during takeoff

4.3.5.1 Aerodynamic Forces

The aerodynamic forces and torque calculated from CFD solver are plotted in Figure 4–13 and Figure 4–14. The body motion is prescribed as the measured data, as well as the hindwing motion. It should be notified that since a rigid wing is assumed, there will exist some non-physical overlap between the elytra and hindwing. Two simulations are conducted for a body-wing model and body-elytron model as shown in Figure 4–5, intending to consider the aerodynamic drag induced torque around body roll axis. As for the effect of elytra on lift, the elytra can only produce lift of less than 1% of the body weight in beetle *Allomyrina dichotoma* in a quasi-static study[109], and the force generated by elytra in rhinoceros beetle (*Trypoxylus dichotomus*) is found to be negligible in hovering[106].

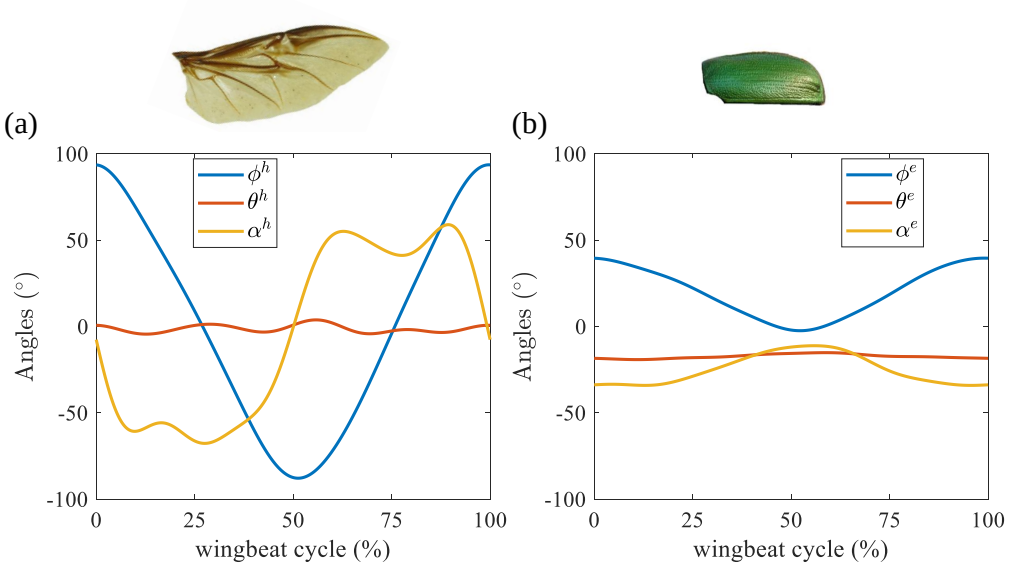

Figure 4–12 The hindwing and elytron kinematics during forward flight of green chafer at a speed of 1.2m/s.

Thus, even if elytra are eliminated, it should not lead to significant difference since the translational speed during the takeoff sequence is around or less than 1m/s which is close to a hover state at such slow advance ratio. The body kinematic is prescribed as data 6, as well as the hindwing kinematics. Since the elytron flapping amplitude is small as shown in Figure 4–12, and the stroke reversal is almost at the same time as that of hindwing, we applied cyclic periodic wing kinematics as in Figure 4–12(b) in the body-elytron model simulation, whereas the body CM still follows the trajectory of data 6.

It can be seen in Figure 4–13(a) that even with large change in body posture, the beetle is still able to maintain a relatively high lift force to support the body where the average lift force in each wing beat cycle only varies from 0.8Mg ∼1.2Mg, thus the vertical position during taking off does not descend much before insect becomes properly adjusted for a forward flight. In a helicopter model, the aerodynamic force is always perpendicular to the wing stroke plane. The beetle is quite different from the helicopter model, though with roll angle change up to 150 degrees, the total aerodynamic force is almost vertical in every wing beat cycle with only slight side/backward projection for the backward flight acceleration as can be seen in Figure 4–7.

A large proportion of the lift force contributes from the upstroke in the first few cycles during taking off as can be seen in Figure 4–13. During the first 2-3 cycles, hind-

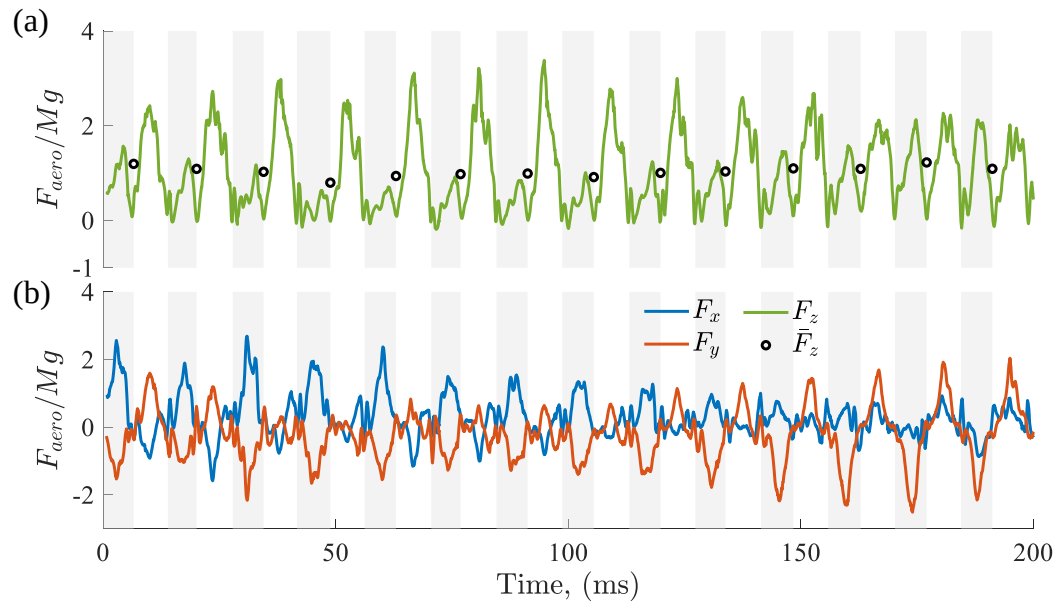

Figure 4–13 The aerodynamic force in ground frame of flight sequence data 6 with prescribed body motion and prescribed wing kinematics as in Figure 4–11. The forces are scaled by the average gravity of a green chafer. (a) the aerodynamic lift force in z direction and the cyclic average $\bar{F}_z$. Down strokes are patched in grey color. (b) the aerodynamic force projected in x and y directions are plotted in blue and red solid line respectively.

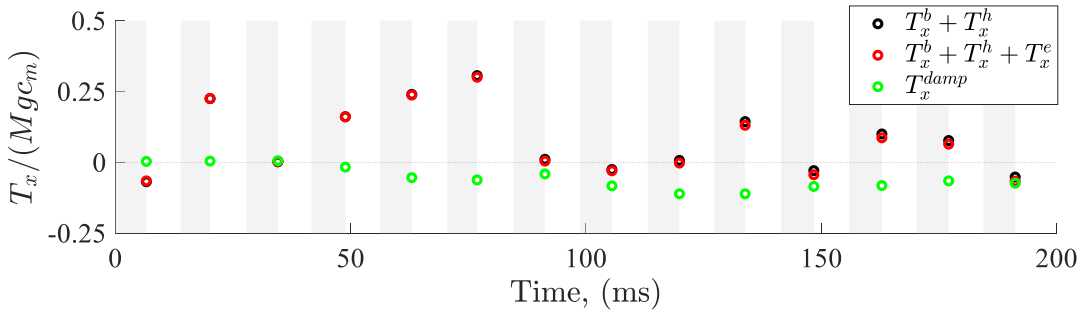

Figure 4–14 The cyclic average aerodynamic torque of body-wing model in body frame of flight sequence data 6 scaled by the multiplication of gravity and mean chord length. (Black circles) T_x^b,T_x^h,T_x^e represent the aerodynamic torque generated by body, hindwings and elytra separately. The red circles represents the resultant torque induced by body fore&hind wings. Green circles represent the aerodynamic damping torque in the case of prescribed body kinematics and symmetric wing kinematics as forward flight.

wing stroke plane is almost vertical with the normal vector of the stroke plane orienting backward (Figure 4–7), hence during the down-stroke wing translates from a downward position to upward position, contributing few lift forces (Figure 4–13). When the body is well posed during the 10-14 cycles, lift force generated by the upstroke is almost equal to that of down-stroke. This phenomenon is similar to the backward flight of a dragonfly where most of the lift force is also contributed from the upstroke[104]. There is a small horizontal component of the aerodynamic force which accelerates the body in the backward direction, drifting away from the branch (Figure 4–13, Figure 4–13).

4.3.5.2 Aerodynamic roll torque

The resultant torque of elytra, fore wing and body during takeoff is plotted in Figure 4–14 as the red circles. It can be found that except for the last few cycles when body translational velocity reaches 1m/s, the aerodynamic torque generated by elytra around x axis is minor. Even in the last few cycles, the magnitude of T_x is only of magnitude $0.01Mgc_m$, which can be neglected.

The aerodynamic torque around body longitudinal axis is averaged for each wing beat cycle in Figure 4–14 since the instantaneous aerodynamic torque is much larger than the cyclic average while it is the average which determines the roll of body. The roll accelerating phase is during the $4 \sim 6^{th}$ wing beat cycles (Figure 4–14), which coincides well with data 6 in Figure 4–8 that the turning points locates around 4-5th cycles. It can be found that the aerodynamic torque around rolling axis is relatively small compared with a reference torque Mgc_m. The average torque in 14 wing beat cycles is $0.07Mgc_m$ calculated from the CFD result of the aerodynamic torque around body longitudinal axis (Figure 4–14). According to the simplified roll dynamic equation $I_{xx}\frac{d\omega}{dt} = T_x$, the roll angle of 10 cycles is estimated to be roll $\frac{1}{2}\frac{T_x}{I_{xx}}\Delta t^2 \sim O(10^2)$ through dimensional analysis. Here the T_x is the resultant torque of insect active control torque as well as the damping induced one. Meanwhile the roll angle of data 6 is around 120 degrees in 10 wing beat cycles which proves our simulation to be in good agreement with the experimental data. The taking off process is relatively slow compared with the evasive maneuver of hummingbird which can generate a torque of magnitude $0.3MgR_{wing}$ and achieve an alteration of heading to the opposite direction within 2 3 wing beat cycles[8, 14], yet similar to that of fruit fly bank turn which generate average torque magnitude of approximately $0.03 \sim 0.05MgR_{wing}$[6, 113].

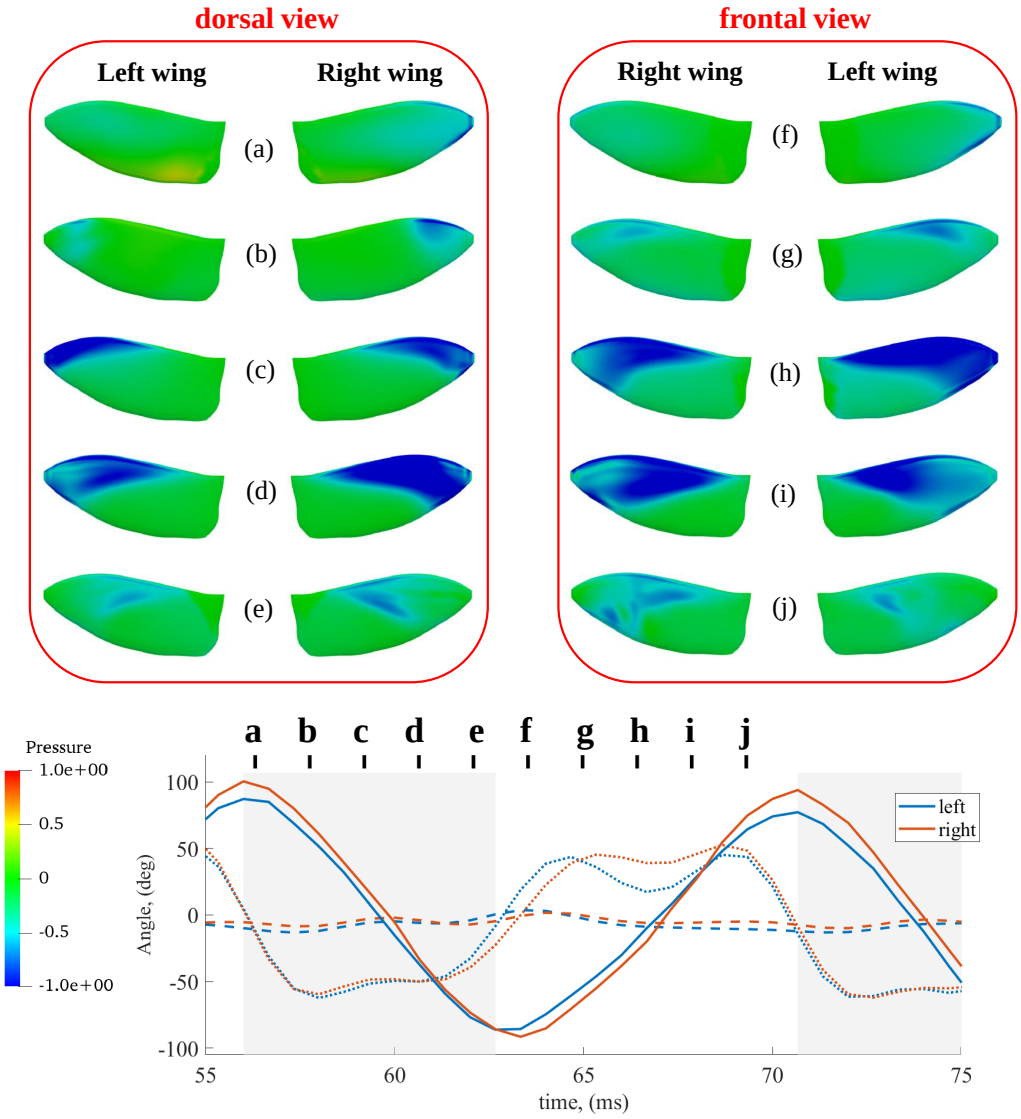

Figure 4–15 The pressure distribution on beetle wings in a wing beat cycle. The wing kinematics is a segment of Figure 4–11 The sub-figures on the upper panel correspond to the time instant marked in the lower panel.

To quantify the maneuverability of green chafer, several time constants are analyzed for the simplified roll dynamic equation. If aerodynamic damping of roll dominates, the beetle would need to generate positive roll torque continuously in order to overcome the viscous induced drag, or the rotational velocity would quickly dissipate to zero. An extra case with prescribed body dynamics as data 6 and symmetric wing kinematics is simulated to compute the aerodynamic damping torque, and the cyclic averaged results are shown in Figure 4–14 (green markers). In the case of beetle takeoff flight with symmet-

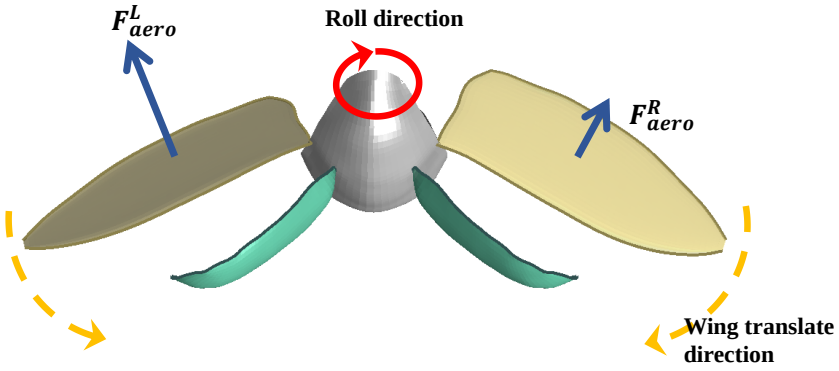

Figure 4–16 An illustration of the rolling torque generation during beetle takeoff.

ric wing kinematics, the averaged aerodynamic damping torque is $6.34mNmm$ at average angular velocity of $17.5rad/s$, hence $b_{damp} = \bar{T}_x^{damp}/\bar{\omega} = 3.6 \times 10^{-7} Nms/rad$(Figure 4–14). The open-loop time constant τ_p calculated as Equation 4–5[8]. It takes around $1 \sim 2$ cycles to achieve a desired angular velocity, hence the corresponding closed-loop time constant $\tau_{CL} = t_{63\%} \sim 15ms$.

$$\tau_p = \frac{I_{xx}}{b_{damp}} = 0.0164s \tag{4–5}$$

The active maneuvering time constant(τ_a) is $5.7ms$ on average for a time sequence of $50ms \sim 100ms$ (Equation 4–6[8]), it can even be shorter as $3.8ms$ if the average torque is as large as the peak torque magnitude in Figure 4–14.

$$\tau_a = \frac{\omega_m(1 - e^{-1})}{T_m/I_{xx}} \tag{4–6}$$

Therefore, $\tau_p \sim \tau_{CL} > \tau_a$, which hint for active maneuver dominant while the insect choose a relatively slow way to realize the takeoff maneuver though it could be faster.

The pressure distribution on both wings are plotted in Figure 4–15, which gives a more straightforward view of the torque generation. The rolling torque is generated due to the asymmetric wing kinematics according to Figure 4–16. Most of the rolling torque is generated during $50ms \sim 100ms$ as shown in Figure 4–14 when roll angular velocity is still small, during which time sequence the average inner wing feathering angle ($\bar{\alpha}_R$) of upstroke is larger than that of the outer wing ($\bar{\alpha}_L$), indicating a smaller attack angle in the inner wing (Figure 4–15(h,i)). Thus, during upstroke, outer wing experience larger force

as illustrated in Figure 4–16 which leads to a positive roll torque around body longitudinal axis. Another reason for the positive roll torque is that ϕ^R_{amp} is slightly larger than ϕ^L_{amp} in time sequence $50ms \sim 100ms$ which leads to a faster translating speed of inner wing (right wing) in down stroke therefore a positive roll torque is generated (Figure 4–15 (d)). While during $150ms \sim 200ms$, the body translates at a speed of approximately 1m/s (Figure 4–9) with $10^4 deg/s$ roll angular velocity (Figure 4–8), thus the aerodynamic damping as well as the inflow speed makes it hard to interpret the aerodynamic torque simply from the wing kinematics.

4.4 Limitation of this work

Due to the confined camera view, body maneuver is still in the half-way before it goes out of the camera view, hence the body deceleration phase is not recorded. To obtain the full sequence, more cameras are needed, or the cameras can be relocated to obtain larger view at the sacrifice of some wing resolution.

In the CFD simulation, wing is regarded as rigid plate, while the wing deformation during upstroke is large. The simulation of the Rhinoceros beetle *Trypoxylus dichotomus*[106] indicates that the aerodynamic force and power only differ slightly in rigid wing model compared with twisted model during hovering, in our research, the beetle body translational velocity reaches around 1m/s at the end. Though the advance ratio is still small, the deformation of flexible wing caused by inflow and asymmetric wing kinematics need further consideration in our future study. Furthermore, the interaction between elytra and hindwings is neglected to avoid wing elytron overlap, which however will not happen in the case of flexible folding wing.

4.5 Concluding Remarks

In this study, we conducted beetle takeoff experiments and reconstructed the flight data. Beetles take off from a vertical posture in a roll-dominant way with the target light in the dorsal position, which lasts around 10 wing beat cycles. Two CFD models are constructed to investigate the hindwing and the elytron effect separately. It is found that during taking off flight, the change of pitch and yaw angles relative to the initial posture is subtle, while the most significant change happens in roll angle which can vary up to 150 degrees. Even with such significant change in body angle, beetle is still able to generate enough lift force close to the gravity force. Asymmetric hindwing kinematics make

significant contribution to the roll torque while seldom influence from the elytra. The maneuverability of beetle is further investigated by comparing the open-loop constant and active control constant as well as the close-loop time constant. It is found that though beetle is capable of generating a roll torque much larger than the damping torque, the takeoff is still realized in a slow way. The roll-dominant takeoff shows the kinematic intelligence which is capable of re-orienting the head position in short time without significant loss of translational momentum.

Chapter 5 Concluding remarks and future works

5.1 Concluding remarks

Insects have long evolved in the morphological and kinematic perspective to realize both robust and agile flight.

On the wing morphology perspective, it is found that the realistic wing-body-mass-ratios in the three insect models can suppress the body pitch oscillation to a minimized level at a very low cost of mechanical power based on simulation results. A scaling law is further derived to correlate the WBMR with flapping-wing kinematics of stroke amplitude (Φ), flapping frequency (f), and wing length (R) in terms of $\Phi R f^2$, which matches well with measurements and, thus, implies that the WBMR-based body pitch minimization may be a universal mechanism in hovering insects. The realistic WBMR likely offers a novel solution to resolve the trade-off between body-dynamics-based aerodynamic performance and power consumption. Our results indicate that the WBMR plays a crucial role in optimization of flapping-wing dynamics, which may be useful as novel morphological intelligence for the biomimetic design of insect- and bird-sized flapping micro-aerial vehicles.

On the insect control perspective, it is found that the intermittent control can achieve an angular-dominant flight control, whereas the conventional continuous control model corresponds to an angular-velocity-dominant one. Given the biological constraints in sensorimotor neurobiology and musculoskeletal mechanics, the intermittent control strategy was examined capable of enhancing the stabilization robustness in terms of sensory latency, stroke derivation, spike interval, and damping strength. Our results indicate that the intermittent control strategy is likely a sophisticated flight control mechanism in insect flights.

Furthermore, based on the results of beetle takeoff, it is found that beetle start with an upright position and perform a roll-dominant takeoff which shares similar kinematic intelligence as the hummingbird evasive maneuver. The coordination between wing and body kinematics allows the beetle quickly re-orient the heading and lead to a smooth transition between the initial and final body posture without significant loss of translational momentum.

5.2 Future works

The intermittent model mentioned in Chapter 2 is though proved to be potentially beneficial for hovering stabilization, only one possible intermittent condition is investigated for bumblebee pitch stabilization. Further studies can be extended to body roll and pitch control with other plausible intermittent conditions with other insect models to see whether the benefit is widely applicable.

Due to limited resolution of beetle takeoff flight, the body kinematics is smoothed within a wing beat cycle. A zoom-in and artificial markers may ensure more precise observation of the body kinematic change and less post-process in digitizing. And a zoom-out of the camera view is able to provide a full flight sequence of taking off to better reflect the rolling initiation and cessation. In the meanwhile, current deep learning tools[45-46] would be a good try to deal with many long sequence flight videos to provide more flight data which remains to be explored.

Till now, the majority of our study focused on the intelligence of individual flight behavior. The birds flocking behavior has been investigated on[114] which inspired researchers to solve the congestion in a smart way[115], yet few concentrate on the insects. The investigation of insect group behavior requires a large amount of material as well as computational resources whereas meaningful to investigate. How insects avoid collision in a large group can straightforwardly reflect the flight maneuverability and may also reveal their functional limits in flight, and may also proved inspiration for the future flapping Micro-Air-Vehicle design.

Appendix A Appendix

A.1 The summarized morphological & kinematic parameters

Table A–1 A summarization of the morphological and kinematic parameters of different species. (Figure 2–1). The data of butterflies are obtained from Dudley Robert[57], and bats& birds data are from Berg, C and Rayner[59]

Species	frequency(Hz)	$\varepsilon(\%)$	Species	frequency(Hz)	$\varepsilon(\%)$
Butterfly [1]	12.4	5.4	Bird 1	2.64	7.81
Butterfly [2]	9.5	5.5	Bird 2	4.90	6.83
Butterfly [3]	12	6.9	Bird 3	4.48	8.10
Butterfly [4]	13.7	7.3	Bird 4	3.19	9.40
Butterfly [5]	11.7	6.5	Bird 5	17.8	3.03
Butterfly [6]	8.9	5.3	Bird 6	3.50	7.41
Butterfly [7]	9.1	5.9	Bird 7	9.43	5.04
Butterfly [8]	10.7	5.6	Bird 8	9.40	4.50
Butterfly [9]	10.7	4.8	Bird 9	6.71	7.67
Butterfly [10]	13.9	5.1	Bird 10	9.35	5.59
Butterfly [11]	13.3	5.0	Bird 11	16.1	4.60
Butterfly [12]	6.4	10.3	Bird 12	8.55	5.59
Butterfly [13]	6.9	9.5	Bird 13	10.0	5.01
Butterfly [14]	9.6	9.9	Bird 14	17.3	5.53
Butterfly [15]	13.7	6.5	Bird 15	27.4	4.34
Bat [1]	13.9	5.60	Bird 16	11.3	6.37
Bat [2]	10.0	5.62	Bird 17	3.97	8.77

Table A–2 Morphological and Kinematic Parameters of Figure 2–7. The hawk moth data are from Willmot A.P.[58] and Yao et. al.[56], and some diptera data are from Ennos A.R.[54-55]

Species	$\Phi(rad)$	$f(Hz)$	$R(m)\times 10^3$	$(\Phi R f^2)^{-1}\times 10^3$	$\varepsilon(\%)$
Bumblebee [1]	2.024	155	13.2	1.56	0.26
Bumblebee [2]	2.433	145.1	15.0	1.30	0.18
Bumblebee [3]	2.094	152	14.1	1.47	0.24
Bumblebee [4]	2.286	140	14.1	1.58	0.29

Continuation of Table A–1

Species	$\Phi(rad)$	$f(Hz)$	$R(m)\times 10^3$	$(\Phi R f^2)^{-1}\times 10^3$	$\varepsilon(\%)$
Hummingbird hawk moth	2.007	70	20.2	5.03	2.44
Hawk moth [1]	1.997	26.1	48.5	15.16	3.15
Hawk moth [2]	2.119	26.3	51.9	13.15	3.07
Hawk moth [3]	1.975	25.4	52.1	15.06	2.35
Fruit fly [1]	2.620	240	3.0	2.21	0.12
Fruit fly [2]	2.618	254	2.02	2.93	0.12
Hover fly [1]	1.501	183	11.5	1.73	0.38
Hover fly [2]	1.710	172	10.8	1.83	0.36
Hover fly [3]	1.570	160	9.3	2.67	0.64
Hover fly [4]	1.658	159	9.3	2.57	0.64
Hover fly [5]	1.152	141	10	4.37	0.75
Crane fly [1]	1.954	59	16.8	8.75	0.96
Crane fly [2]	2.146	45.5	12.7	17.72	2.24
Crane fly [3]	2.094	58	17.4	8.16	1.21
Hawthorn fly [1]	2.435	100	11.2	3.67	0.34
Hawthorn fly [2]	2.408	130	9.4	2.61	0.56
Blue bottle fly	2.618	117	9.2	3.03	0.38
Ladybird	3.089	53.9	11.2	9.95	1.47
Drone fly	1.902	157	11.4	1.87	0.78
Honeybee	2.286	197	9.8	1.15	0.25
Hummingbird	2.566	50	44	3.50	3.90

A.2 The scaling between wing mass and total mass

From Figure A–1, it can be found that there exist apparent correlation between wing and body mass. It is reasonable to understand through some dimensional analysis since $m_b \sim k_1 R^3$, while $m_w \sim k_2 R^3$, thus $log m_b \sim k_3 log m_w$ exhibiting linear relationship. As wing& body mass become smaller(insect group), there exists more variety of possible combination of wing and body mass, which is probably due to the different flapping characteristics in kinematics. Birds, bats and butterflies share similar wing kinematics, while insects like fruit fly, bumblebee or thrips wingtip trajectory shows to be figure of eight and even with greater elevation change in thrips. Among these insects, bumblebee shows relatively low m_w compared with the body mass, which also indicates a large wing loading.

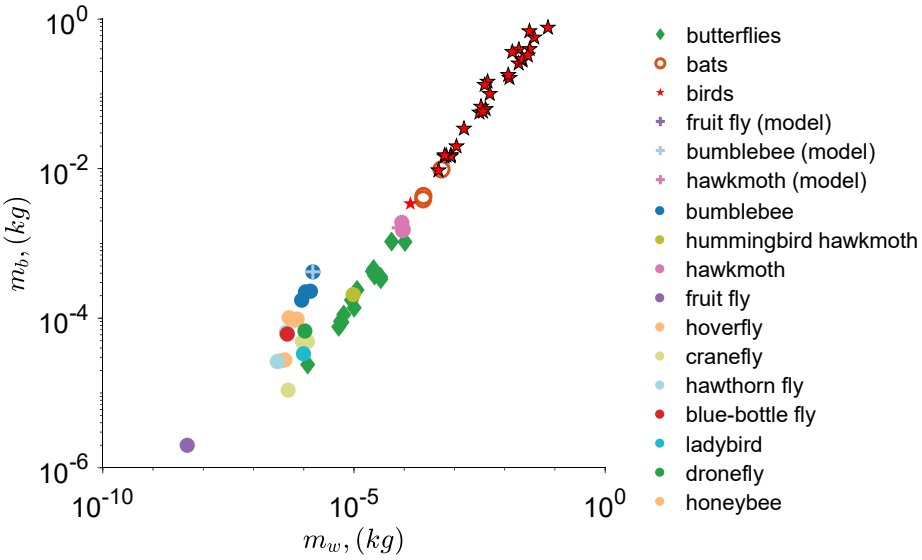

Figure A–1 The relationship between mass of wing pair and total mass of different insect species even includes humming bird. The data are obtained from[2, 54-56, 58]

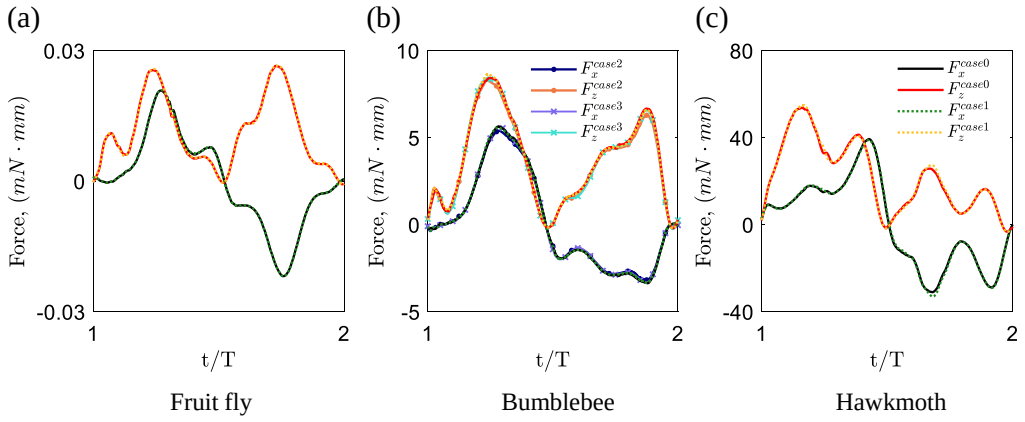

Figure A–2 Grid verification results for three insect species. Case 0&1 are simulated for fruit fly and hawk moth models, and Case 0,1,2,3 are simulated for bumblebee model to verify the independence of time step as well as grid under current condition.

A.3 Fluid Solver Self-consistency and verification

A.3.1 CFD verification

An extensive study on grid dependency is conducted for all three models of hawk moth (Re = 6300) bumblebee (Re = 1613) as well as fruit fly (Re = 134). For the case of bumblebee, we tested four cases. Case 0: wing grid $37\times33\times11$, body grid $37\times39\times19$, background grid $92\times84\times68$ with time step $\frac{1}{1000}T$. Case 1: wing grid $37\times33\times11$, body grid $37\times39\times19$, background grid $132\times124\times108$ with time step $\frac{1}{1000}T$. Case 2: wing grid $73\times65\times11$, body grid $37\times39\times19$, background grid $92\times84\times68$ with time step $\frac{1}{2000}T$. Case 3: wing grid $37\times33\times21$, body grid $37\times39\times19$, background grid $92\times84\times68$ with time step $\frac{1}{2000}T$. For the case of hawk moth, Case 0: wing grid $37\times33\times11$, body grid $37\times39\times9$, background grid $92\times84\times68$ with time step $\frac{1}{2000}T$. For fruit fly case 0: wing grid $33\times35\times13$, body grid $33\times33\times9$, background grid $92\times84\times68$ with time step $\frac{1}{2000}T$. The background grid increased to $132\times124\times108$ for case 1 of both fruit fly and hawk moth models for grid verification. The calculated aerodynamic force projection in x and z directions are plotted in Figure A–2, obviously show seldom difference for the cases.

A.3.2 Wing thickness effect on aerodynamic performance in fruit fly

To verify that the result is not affected by wing thickness in our model, a fruit fly wing with different thickness is simulated (Figure A–3), and the aerodynamic force components are compared in Figure A–4. The difference between the two wing thicknesses is a margin, indicating that the small change in wing thickness will not affect the overall conclusion in this study.

A.4 The beetle takeoff video digitization method

A.4.1 Camera calibration

Two cameras are used in the tracking process with angle difference of around 30˚ to allow for larger region that can be covered by both cameras. The cameras are calibrated using a rigid calibration board with certain marker pattern. There exists a transformation matrix (**H**) between the three-dimensional coordinate in ground frame and the two-dimensional coordinate in image frame, which is composed of the intrinsic camera matrix and the extrinsic matrix (rotation and translation) due to the relative position of

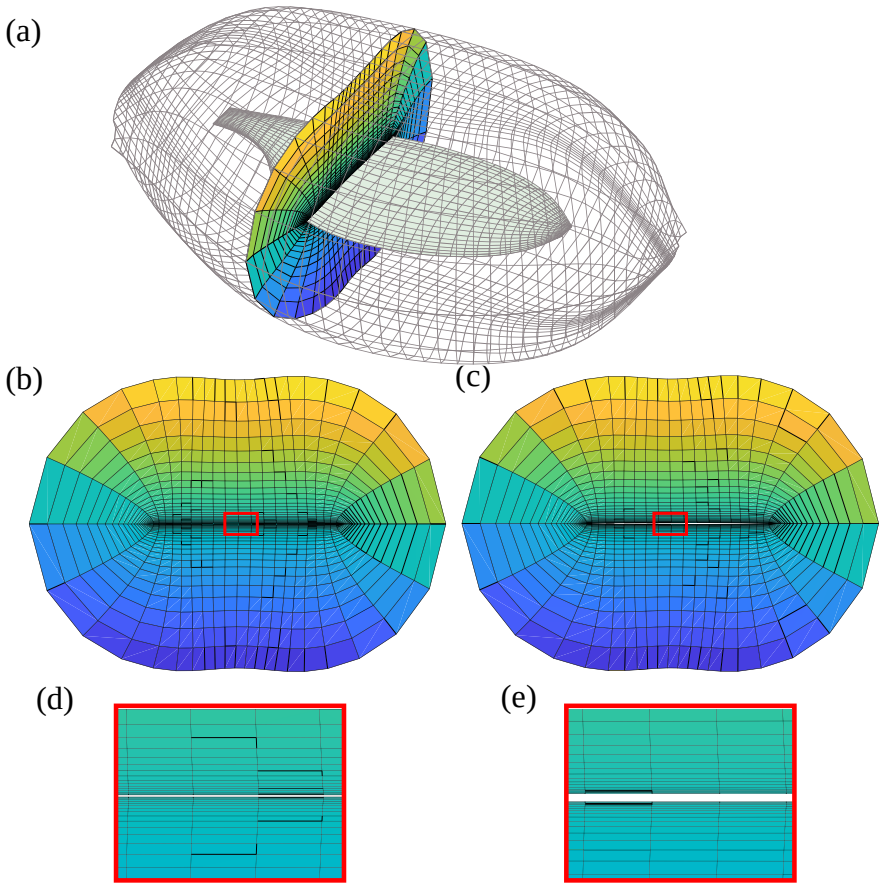

Figure A–3 Perspective (a), (b) ($h_s = 0.0017c_m$), (c)($h_s = 0.008c_m$) and close-up views (d)($h_s = 0.0017c_m$), (e)($h_s = 0.008c_m$) of a fruit fly wing grid.

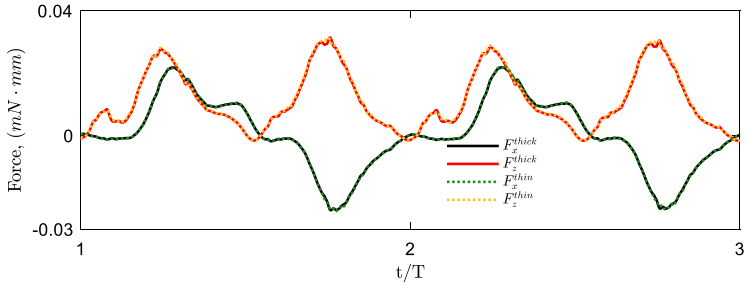

Figure A–4 The aerodynamic force components of a fruit fly model with a thin wing with mean wing thickness $h_s^{thin} = 0.0017c_m$ and a thick wing $h_s^{thick} = 0.008c_m$.

pixel frame and the ground frame. The intrinsic and extrinsic parameters of camera including the focal length, distortion parameters etc. are obtained through minimizing the error between marker pixel coordinates on images and the corresponding pixel coordinate in projection transformation.

A.4.2 The shape extraction of body and elytron

One specimen is marked with lines for digitization as in Figure A–6. Two camera views are used for digitizing the shape of the elytron after calibration. To generate structured grid, the outline of the elytron is obtained at first, based on the outline a plane (xy plane), structured grid can be generated through hyperbolic interpolation. The z coordinate can be interpolated through projecting the digitized points onto the grid in xy plane and then smoothed. And finally based on the inner layer grid, we can generate outer layers. Similar method is also used for body shape digitization and obtaining the body structured inner and outer grid. Therefore, the shape of body and elytron can be obtained even without the use of 3D scanner. An illustration of the body and elytron inner and outer layers of grids are shown in Figure 4–5. To note that, because no artificial marker is attached to insect during voluntary take off, hence the digitization may include some bias in human tracking based on the silhouettes and texture. As mentioned in the study of auto tracking[43], it is hard to estimate the body roll angle of *Drosophila* due to the near-cylindrical body shape. Though the body shape of beetle looks like a half sphere, the method of shape fitting may still introduce some error. However, the elytra hinge as well as wing hinge points serve as natural markers to narrow down the digitization error since the relative position between head/tail point and the hinge points are fixed in body fixed frame. Furthermore, the fact that our digitization results are proven to be in well correspondence with the experimental phenomenon in later sections further verified our digitization.

A.4.3 Wing & body kinematics digitization

The wing kinematics can be described by three angles relative to the stroke plane: the stroke angle (ϕ) projected in the stroke plane, the elevation angle(θ) representing the vector of wingtip to base that elevate above/below the stroke plane, and rotation angle (α) of wing rotating around the wing tip to base axis. The rotation matrix that projects the

vector from wing frame to body frame can be expressed as the following (Equation A–1).

$$E_{wing2body} = R_y(\frac{\pi}{2} - \beta)R_x(\alpha)R_z(\theta)R_y(\alpha) \tag{A–1}$$

$$E_{wing2body} = R_y(\frac{\pi}{2} - \beta)E_{wing2SP} \tag{A–2}$$

Here β is the anatomical stroke plane angle(ASPA) which defines the relative position of the stroke plane to the body frame. β can be calculated by fitting a plane to the wing-tip trajectories in body frame.

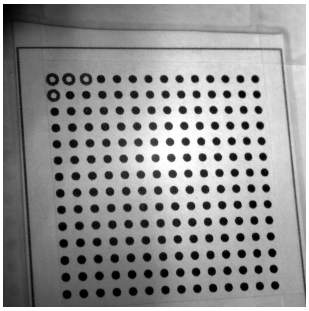

Figure A–5 An example of calibration grid in one camera view.

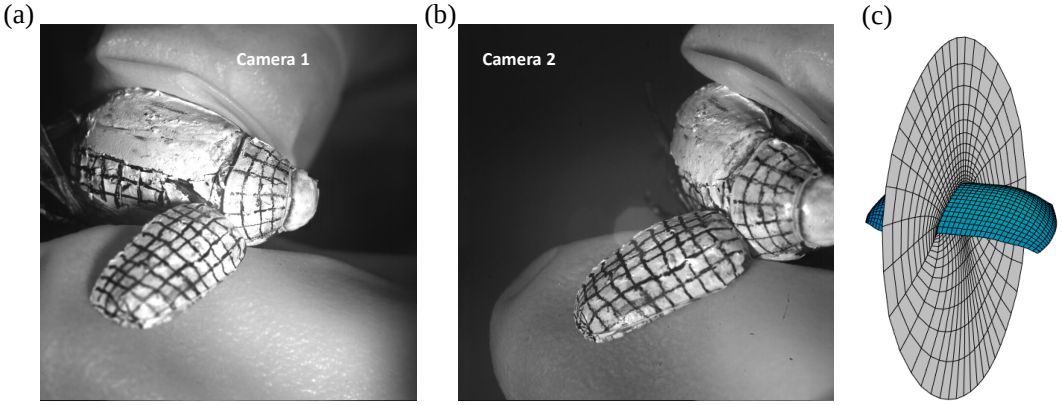

Figure A–6 Perspective views of elytron from two cameras at the same time instant (a,b) two camera views (c) The inner layer grid of beetle elytron, and a perspective of the outter layers.

Once the wing base to tip vector $\vec{R}_{b2t}$ is obtained in stroke plane frame, the vector of wing base to tip in wing fixed frame is $R_{wing}[0;1;0]$, and the transformation between the two vectors can be expressed as:

$$\vec{R}_{b2t}^{SPframe} = E_{wing2SP}L_{wing}\begin{bmatrix}0\\1\\0\end{bmatrix} \tag{A–3}$$

Hence we can obtain Equation A–4,A–5

$$\theta = arcsin(\frac{-\vec{R}_{b2t}^{SPframe}(1)}{L_{wing}}) \tag{A–4}$$

$$\phi = arctan(\frac{\vec{R}_{b2t}^{SPframe}(2)}{\vec{R}_{b2t}^{SPframe}(3)}) \tag{A–5}$$

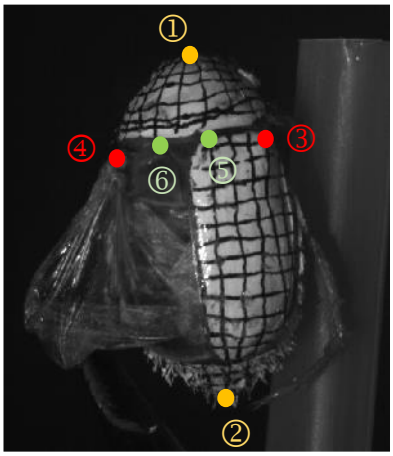

Figure A–7 Six points that used for body posture definition:① is the head point, point ② is the tail point, point ③④ are the hind wing hinge points, point ⑤, ⑥ represent the elytra hinge points.

Another point which doesn't locate on the wing base to tip line is needed to calculate the wing rotation angle α. However, sometimes the wing doesn't have apparent marker apart from the base and tip points, it is difficult to digitize the wing rotation angle. Whereas, if the wing shape is known beforehand, and the wing base and tip points are digitized, the wing rotation angle can be obtained through shape fitting. By changing the α until the projection of the wing contour shows best match with the pictures in two camera views, the resulting value is defined as α.

Body kinematics need to be digitized before wing kinematics, since all coordinates in ground frame needed to be projected into body frame to conduct analysis for wing kinematics digitization. The transformation matrix from body frame to ground frame is as Equation A–6 where the three angles yaw, pitch, roll defined relative to z, y, x axis respectively.

$$E_{b2g} = R_z(yaw)R_y(pitch)R_x(roll) \tag{A–6}$$

The points digitized on body are: the head point, the tail point and two wing hinge points. The hind wing hinge points sometimes are not very apparent due to the existence of elytron, and also because of the large body rotation angle. When body rolls to the side, only one side of the wing hinge is visible, therefore to increase the accuracy, we use the base points of elytron as a reference. The relative position of the six points in Figure A–7 are fixed, hence with certain points digitized, other points can be determined through adjusting the body angles to get the best fit.

Bibliography

[1] Liu H, Kolomenskiy D, Nakata T, et al. Unsteady bio-fluid dynamics in flying and swimming[J]. Acta Mechanica Sinica, 2017, 33(4): 663-684.

[2] Liu H, Aono H. Size effects on insect hovering aerodynamics: an integrated computational study[J]. Bioinspiration & Biomimetics, 2009, 4(1): 015002. DOI: https://doi.org/10.1088/1748-3182/4/1/015002.

[3] Han J S, Han J H. A contralateral wing stabilizes a hovering hawkmoth under a lateral gust[J]. Scientific reports, 2019, 9(1): 1-13.

[4] Ravi S, Crall J D, Fisher A, et al. Rolling with the flow: bumblebees flying in unsteady wakes[J]. Journal of Experimental Biology, 2013, 216(22): 4299-4309.

[5] Crall J, Chang J, Oppenheimer R, et al. Foraging in an unsteady world: bumblebee flight performance in field-realistic turbulence[J]. Interface Focus, 2017, 7(1): 20160086.

[6] Muijres F T, Elzinga M J, Melis J M, et al. Flies evade looming targets by executing rapid visually directed banked turns[J]. Science, 2014, 344(6180): 172-177.

[7] Sapir N, Dudley R. Backward flight in hummingbirds employs unique kinematic adjustments and entails low metabolic cost[J]. Journal of Experimental Biology, 2012, 215(20): 3603-3611.

[8] Cheng B, Tobalske B W, Powers D R, et al. Flight mechanics and control of escape manoeuvres in hummingbirds. II. Aerodynamic force production, flight control and performance limitations[J]. Journal of Experimental Biology, 2016, 219(22): 3532-3543.

[9] Ellington C P, Van Den Berg C, Willmott A P, et al. Leading-edge vortices in insect flight[J]. Nature, 1996, 384(6610): 626-630.

[10] Lentink D, Dickinson M H. Rotational accelerations stabilize leading edge vortices on revolving fly wings[J]. Journal of Experimental Biology, 2009, 212(16): 2705-2719.

[11] Balint C N, Dickinson M H. The correlation between wing kinematics and steering muscle activity in the blowfly Calliphora vicina[J]. Journal of experimental biology, 2001, 204(24): 4213-4226.

[12] Tu M, Dickinson M. The control of wing kinematics by two steering muscles of the blowfly (Calliphora vicina)[J]. Journal of Comparative Physiology A, 1996, 178(6): 813-830. DOI: https://doi.org/10.1007/BF00225830.

[13] Dickinson M H, Muijres F T. The aerodynamics and control of free flight manoeuvres in Drosophila[J]. Philosophical Transactions of the Royal Society B: Biological Sciences, 2016, 371(1704): 20150388.

[14] Cheng B, Tobalske B W, Powers D R, et al. Flight mechanics and control of escape manoeuvres in hummingbirds. I. Flight kinematics[J]. Journal of Experimental Biology, 2016, 219(22): 3518-3531.

[15] Deora T, Gundiah N, Sane S P. Mechanics of the thorax in flies[J]. Journal of Experimental Biology, 2017, 220(8): 1382-1395.

[16] Walker S M, Schwyn D A, Mokso R, et al. In vivo time-resolved microtomography reveals the mechanics of the blowfly flight motor[J]. PLoS Biol, 2014, 12(3): e1001823.

[17] Ando N, Kanzaki R. Flexibility and control of thorax deformation during hawkmoth flight[J]. Biology letters, 2016, 12(1): 20150733.

[18] King M J, Buchmann S L, Spangler H. Activity of asynchronous flight muscle from two bee families during sonication (buzzing).[J]. Journal of Experimental Biology, 1996, 199(10): 2317-2321.

[19] Sherman A, Dickinson M H. Summation of visual and mechanosensory feedback in Drosophila flight control[J]. Journal of experimental biology, 2004, 207(1): 133-142.

[20] Chittka L, Williams N, Rasmussen H, et al. Navigation without vision: bumblebee orientation in complete darkness[J]. Proceedings of the Royal Society of London. Series B: Biological Sciences, 1999, 266(1414): 45-50.

[21] Sane S P, Dieudonné A, Willis M A, et al. Antennal mechanosensors mediate flight control in moths[J]. Science, 2007, 315(5813): 863-866.

[22] Dickerson B H, Aldworth Z N, Daniel T L. Control of moth flight posture is mediated by wing mechanosensory feedback[J]. Journal of Experimental Biology, 2014, 217(13): 2301-2308.

[23] Sutton G P, Clarke D, Morley E L, et al. Mechanosensory hairs in bumblebees (Bombus terrestris) detect weak electric fields[J]. Proceedings of the National Academy of Sciences, 2016, 113(26): 7261-7265.

[24] Trimarchi J R, Murphey R. The shaking-B2 Mutation Disrupts Electrical Synapses in a Flight Circuit in AdultDrosophila[J]. Journal of Neuroscience, 1997, 17(12): 4700-4710.

[25] Elzinga M J, Dickson W B, Dickinson M H. The influence of sensory delay on the yaw dynamics of a flapping insect[J]. Journal of The Royal Society Interface, 2012, 9(72): 1685-1696.

[26] Liu P, Cheng B. Limitations of rotational manoeuvrability in insects and hummingbirds: evaluating the effects of neuro-biomechanical delays and muscle mechanical power[J]. Journal of the Royal Society Interface, 2017, 14(132): 20170068.

[27] Land M F, Collett T. Chasing behaviour of houseflies (Fannia canicularis)[J]. Journal of comparative physiology, 1974, 89(4): 331-357.

[28] Beatus T, Guckenheimer J M, Cohen I. Controlling roll perturbations in fruit flies[J]. Journal of The Royal Society Interface, 2015, 12(105): 20150075. DOI: http://dx.doi.org/10.1098/rsif.2015.0075.

[29] Ristroph L, Bergou A J, Ristroph G, et al. Discovering the flight autostabilizer of fruit flies by inducing aerial stumbles[J]. Proceedings of the National Academy of Sciences, 2010, 107(11): 4820-4824. DOI: https://doi.org/10.1073/pnas.1000615107.

[30] Ristroph L, Ristroph G, Morozova S, et al. Active and passive stabilization of body pitch in insect flight[J]. Journal of The Royal Society Interface, 2013, 10(85): 20130237. DOI: http://dx.doi.org/10.1098/rsif.2013.0237.

[31] Cheng B, Deng X, Hedrick T L. The mechanics and control of pitching manoeuvres in a freely flying hawkmoth (Manduca sexta)[J]. Journal of Experimental Biology, 2011, 214(24): 4092-4106.

[32] Hedrick T L, Daniel T. Flight control in the hawkmoth Manduca sexta: the inverse problem of hovering[J]. Journal of Experimental Biology, 2006, 209(16): 3114-3130.

[33] Ma K Y, Chirarattananon P, Fuller S B, et al. Controlled flight of a biologically inspired, insect-scale robot[J]. Science, 2013, 340(6132): 603-607.

[34] Chen Y, Zhao H, Mao J, et al. Controlled flight of a microrobot powered by soft artificial muscles[J]. Nature, 2019, 575(7782): 324-329.

[35] Graule M, Chirarattananon P, Fuller S, et al. Perching and takeoff of a robotic insect on overhangs using switchable electrostatic adhesion[J]. Science, 2016, 352(6288): 978-982.

[36] Willmott A P, Ellington C P. The mechanics of flight in the hawkmoth Manduca sexta. I. Kinematics of hovering and forward flight.[J/OL]. Journal of Experimental Biology, 1997, 200(21): 2705-2722. eprint: https://journals.biologists.com/jeb/article-pdf/200/21/2705/1233826/2705.pdf. https://doi.org/10.1242/jeb.200.21.2705. DOI: 10.1242/jeb.200.21.2705.

[37] Cheng B, Deng X, Hedrick T L. The mechanics and control of pitching manoeuvres in a freely flying hawkmoth (Manduca sexta)[J/OL]. Journal of Experimental Biology, 2011, 214(24): 4092-4106. eprint: https://journals.biologists.com/jeb/article-pdf/214/24/4092/1278169/4092.pdf. https://doi.org/10.1242/jeb.062760. DOI: 10.1242/jeb.062760.

[38] Nguyen Q V, Park H C, Goo N S, et al. Characteristics of a Beetle's Free Flight and a Flapping-Wing System that Mimics Beetle Flight[J/OL]. Journal of Bionic Engineering, 2010, 7(1): 77-86. https://www.sciencedirect.com/science/article/pii/S1672652909601955. DOI: https://doi.org/10.1016/S1672-6529(09)60195-5.

[39] Kolomenskiy D, Ravi S, Xu R, et al. The dynamics of passive feathering rotation in hovering flight of bumblebees[J/OL]. Journal of Fluids and Structures, 2019, 91: 102628. https://www.sciencedirect.com/science/article/pii/S088997461830714X. DOI: https://doi.org/10.1016/j.jfluidstructs.2019.03.021.

[40] Nasir N, Mat S. An automated visual tracking measurement for quantifying wing and body motion of free-flying houseflies[J]. Measurement, 2019, 143: 267-275.

[41] Moeslund T B, Hilton A, Krüger V. A survey of advances in vision-based human motion capture and analysis[J]. Computer vision and image understanding, 2006, 104(2-3): 90-126.

[42] Ristroph L, Berman G J, Bergou A J, et al. Automated hull reconstruction motion tracking (HRMT) applied to sideways maneuvers of free-flying insects[J]. Journal of Experimental Biology, 2009, 212(9): 1324-1335.

[43] Fontaine E I, Zabala F, Dickinson M H, et al. Wing and body motion during flight initiation in Drosophila revealed by automated visual tracking[J]. Journal of Experimental Biology, 2009, 212(9): 1307-1323.

[44] Hedrick T L. Software techniques for two-and three-dimensional kinematic measurements of biological and biomimetic systems[J]. Bioinspiration & biomimetics, 2008, 3(3): 034001.

[45] Mathis A, Mamidanna P, Cury K M, et al. DeepLabCut: markerless pose estimation of user-defined body parts with deep learning[J]. Nature neuroscience, 2018, 21(9): 1281-1289.

[46] Cao Z, Hidalgo G, Simon T, et al. OpenPose: realtime multi-person 2D pose estimation using Part Affinity Fields[J]. IEEE transactions on pattern analysis and machine intelligence, 2019, 43(1): 172-186.

[47] Whitney J P, Wood R J. Aeromechanics of passive rotation in flapping flight[J]. Journal of fluid mechanics, 2010, 660: 197.

[48] Dickinson M H, Lehmann F O, Sane S P. Wing rotation and the aerodynamic basis of insect flight[J]. Science, 1999, 284(5422): 1954-1960.

[49] Wood R J, Cho K, Hoffman K. A novel multi-axis force sensor for microrobotics applications[J]. Smart materials and structures, 2009, 18(12): 125002.

[50] Graetzel C F, Fry S N, Beyeler F, et al. Real-time microforce sensors and high speed vision system for insect flight control analysis[C]. in: Experimental Robotics. 2008: 451-460.

[51] Nakata T, Liu H, Bomphrey R J. A CFD-informed quasi-steady model of flapping-wing aerodynamics[J]. Journal of fluid mechanics, 2015, 783: 323-343.

[52] Liu H. Integrated modeling of insect flight: From morphology, kinematics to aerodynamics[J]. Journal of Computational Physics, 2009, 228(2): 439-459. DOI: http://dx.doi.org/10.1016/j.jcp.2008.09.020.

[53] Maeda M, Gao N, Nishihashi N, et al. A free-flight simulation of insect flapping flight[J]. Journal of Aero Aqua Bio-mechanisms, 2010, 1(1): 71-79. DOI: https://doi.org/10.5226/jabmech.1.71.

[54] Ennos A R. Inertial and aerodynamic torques on the wings of Diptera in flight[J]. Journal of Experimental Biology, 1989, 142(1): 87-95.

[55] Ellington C P. The aerodynamics of hovering insect flight. II. Morphological parameters[J]. Philosophical Transactions of the Royal Society of London. B, Biological Sciences, 1984, 305(1122): 17-40.

[56] Yao J, Yeo K. Free hovering of hummingbird hawkmoth and effects of wing mass and wing elevation[J]. Computers & Fluids, 2019, 186: 99-127. DOI: https://doi.org/10.1016/j.compfluid.2019.04.007.

[57] Dudley R. Biomechanics of flight in neotropical butterflies: morphometrics and kinematics[J]. Journal of Experimental Biology, 1990, 150(1): 37-53.

[58] Willmott A P, Ellington C P. The mechanics of flight in the hawkmoth Manduca sexta. I. Kinematics of hovering and forward flight[J]. Journal of experimental Biology, 1997, 200(21): 2705-2722.

[59] Berg C, Rayner J. The moment of inertia of bird wings and the inertial power requirement for flapping flight[J]. Journal of experimental biology, 1995, 198(8): 1655-1664.

[60] Fei Y H J, Yang J T. Importance of body rotation during the flight of a butterfly[J]. Physical Review E, 2016, 93(3): 033124.

[61] Suzuki K, Okada I, Yoshino M. Effect of wing mass on the free flight of a butterfly-like model using immersed boundary–lattice Boltzmann simulations[J]. Journal of Fluid Mechanics, 2019, 877: 614-647.

[62] Nan Y, Peng B, Chen Y, et al. Can scalable design of wings for flapping wing micro air vehicle be inspired by natural flyers?[J]. International Journal of Aerospace Engineering, 2018, 2018.

[63] Dirks J H, Taylor D. Veins improve fracture toughness of insect wings[J]. PloS one, 2012, 7(8): e43411.

[64] Song Z, Tong J, Yan Y, et al. Effects of microfluid in the veins of the deployable hindwings of the Asian ladybeetle on flight performance[J]. Computers in biology and medicine, 2020, 121: 103817.

[65] Yin B, Luo H. Effect of wing inertia on hovering performance of flexible flapping wings[J]. Physics of Fluids, 2010, 22(11): 111902.

[66] Nakata T, Liu H. Aerodynamic performance of a hovering hawkmoth with flexible wings: a computational approach[J]. Proceedings of the Royal Society B: Biological Sciences, 2012, 279(1729): 722-731.

[67] Ueyama K, Kolomenskiy D, Ravi S, et al. Aerodynamic performance of bumblebees with flexible wing hinges[C]. in: Proceedings of The 31st International Congress on High-speed Imaging and Photonics. 2016.

[68] Gao N, Aono H, Liu H. Perturbation analysis of 6DoF flight dynamics and passive dynamic stability of hovering fruit fly Drosophila melanogaster[J/OL]. Journal of Theoretical Biology, 2011, 270(1): 98-111. http://www.sciencedirect.com/science/article/pii/S0022519310006077. DOI: http://dx.doi.org/10.1016/j.jtbi.2010.11.022.

[69] Kolomenskiy D, Ravi S, Xu R, et al. Wing morphology and inertial properties of bumblebees[J]. Journal of Aero Aqua Bio-mechanisms, 2019, 8(1): 41-47. DOI: https://doi.org/10.5226/jabmech.8.41.

[70] Usherwood J R, Ellington C P. The aerodynamics of revolving wings I. Model hawkmoth wings[J]. Journal of Experimental biology, 2002, 205(11): 1547-1564.

[71] Sun M, Wang J, Xiong Y. Dynamic flight stability of hovering insects[J]. Acta Mechanica Sinica, 2007, 23(3): 231-246.

[72] Mao S, Gang D. Lift and power requirements of hovering insect flight[J]. Acta Mechanica Sinica, 2003, 19(5): 458-469.

[73] Ma K Y, Chirarattananon P, Fuller S B, et al. Controlled flight of a biologically inspired, insect-scale robot[J]. Science, 2013, 340(6132): 603-607. DOI: http://dx.doi.org/10.1126/science.1231806.

[74] Liu H, Ravi S, Kolomenskiy D, et al. Biomechanics and biomimetics in insect-inspired flight systems[J]. Philosophical Transactions of the Royal Society B: Biological Sciences, 2016, 371(1704): 20150390. DOI: http://dx.doi.org/10.1098/rstb.2015.0390.

[75] Balint C N, Dickinson M H. Neuromuscular control of aerodynamic forces and moments in the blowfly, Calliphora vicina[J/OL]. Journal of Experimental Biology, 2004, 207(22): 3813-3838. eprint: https://journals.biologists.com/jeb/article-pdf/207/22/3813/1250204/3813.pdf. https://doi.org/10.1242/jeb.01229. DOI: 10.1242/jeb.01229.

[76] Dickinson M H, Muijres F T. The aerodynamics and control of free flight manoeuvres in Drosophila[J/OL]. Philos Trans R Soc Lond B Biol Sci, 2016, 371(1704). https://www.ncbi.nlm.nih.gov/pubmed/27528778. DOI: http://dx.doi.org/10.1098/rstb.2015.0388.

[77] Roth E, Reiser M B, Dickinson M H, et al. A task-level model for optomotor yaw regulation in Drosophila melanogaster: a frequency-domain system identification approach[C]. in: 2012 IEEE 51st IEEE Conference on Decision and Control (CDC). 2012: 3721-3726.

[78] Whitehead S C, Beatus T, Canale L, et al. Pitch perfect: how fruit flies control their body pitch angle[J]. Journal of Experimental Biology, 2015, 218(21): 3508-3519. DOI: http://dx.doi.org/10.1242/jeb.122622.

[79] Lehmann F, Götz K. Activation phase ensures kinematic efficacy in flight-steering muscles of Drosophila melanogaster[J]. Journal of comparative physiology A, 1996, 179(3): 311-322.

[80] Dickinson M H. The initiation and control of rapid flight maneuvers in fruit flies[J]. Integrative and comparative biology, 2005, 45(2): 274-281.

[81] Dickinson M H, Tu M S. The function of dipteran flight muscle[J]. Comparative Biochemistry and Physiology Part A: Physiology, 1997, 116(3): 223-238.

[82] Tu M, Dickinson M. Modulation of negative work output from a steering muscle of the blowfly Calliphora vicina[J]. Journal of Experimental Biology, 1994, 192(1): 207-224.

[83] Hedenström A. How insect flight steering muscles work[J]. PLoS Biol, 2014, 12(3): e1001822.

[84] Loram I D, Gollee H, Lakie M, et al. Human control of an inverted pendulum: is continuous control necessary? Is intermittent control effective? Is intermittent control physiological?[J]. The Journal of physiology, 2011, 589(2): 307-324.

[85] Zhang X, Liu H. A three-axis PD control model for bumblebee hovering stabilization[J]. Journal of Bionic Engineering, 2018, 15(3): 494-504.

[86] Skorupski P, Chittka L. Differences in photoreceptor processing speed for chromatic and achromatic vision in the bumblebee, Bombus terrestris[J]. Journal of Neuroscience, 2010, 30(11): 3896-3903.

[87] Tanaka K, Kawachi K. Response characteristics of visual altitude control system in Bombus terrestris[J]. Journal of experimental biology, 2006, 209(22): 4533-4545.

[88] Bottaro A, Yasutake Y, Nomura T, et al. Bounded stability of the quiet standing posture: an intermittent control model[J]. Human movement science, 2008, 27(3): 473-495.

[89] Hedrick T L, Cheng B, Deng X. Wingbeat time and the scaling of passive rotational damping in flapping flight[J]. Science, 2009, 324(5924): 252-255. DOI: http://dx.doi.org/10.1126/science.1168431.

[90] Sun M, Xiong Y. Dynamic flight stability of a hovering bumblebee[J]. Journal of experimental biology, 2005, 208(3): 447-459. DOI: http://dx.doi.org/10.1242/jeb.01407.

[91] Dickinson M H, Tu M S. The function of dipteran flight muscle[J]. Comparative Biochemistry and Physiology Part A: Physiology, 1997, 116(3): 223-238. DOI: https://doi.org/10.1016/S0300-9629(96)00162-4.

[92] Lindsay T, Sustar A, Dickinson M. The function and organization of the motor system controlling flight maneuvers in flies[J]. Current Biology, 2017, 27(3): 345-358. DOI: http://dx.doi.org/10.1016/j.cub.2016.12.018.

[93] Gawthrop P, Loram I, Gollee H, et al. Intermittent control models of human standing: similarities and differences[J]. Biological cybernetics, 2014, 108(2): 159-168. DOI: http://dx.doi.org/10.1007/s00422-014-0587-5.

[94] Yoshikawa N, Suzuki Y, Kiyono K, et al. Intermittent feedback-control strategy for stabilizing inverted pendulum on manually controlled cart as analogy to human stick balancing[J]. Frontiers in computational neuroscience, 2016, 10: 34. DOI: http://dx.doi.org/10.3389/fncom.2016.00034.

[95] Loram I D, Gollee H, Lakie M, et al. Human control of an inverted pendulum: is continuous control necessary? Is intermittent control effective? Is intermittent control physiological?[J]. The Journal of physiology, 2011, 589(2): 307-324. DOI: http://dx.doi.org/10.1113/jphysiol.2010.194712.

[96] Tanaka K, Kawachi K. Response characteristics of visual altitude control system in Bombus terrestris[J]. Journal of experimental biology, 2006, 209(22): 4533-4545. DOI: http://dx.doi.org/10.1242/jeb.02552.

[97] Skorupski P, Chittka L. Differences in photoreceptor processing speed for chromatic and achromatic vision in the bumblebee, Bombus terrestris[J]. Journal of Neuroscience, 2010, 30(11): 3896-3903. DOI: http://dx.doi.org/10.1523/JNEUROSCI.5700-09.2010.

[98] Ma K Y, Chirarattananon P, Fuller S B, et al. Controlled flight of a biologically inspired, insect-scale robot[J]. Science, 2013, 340(6132): 603-607. DOI: http://dx.doi.org/10.1126/science.1231806.

[99] Wei Q, Niu Z, Chen B, et al. Bang-bang control applied in airfoil roll control with plasma actuators[J]. Journal of aircraft, 2013, 50(2): 670-677.

[100] Van Veen W G, van Leeuwen J L, Muijres F T. Malaria mosquitoes use leg push-off forces to control body pitch during take-off[J]. Journal of Experimental Zoology Part A: Ecological and Integrative Physiology, 2020, 333(1): 38-49.

[101] Chen M W, Sun M. Wing/body kinematics measurement and force and moment analyses of the takeoff flight of fruitflies[J]. Acta Mechanica Sinica, 2014, 30(4): 495-506.

[102] Dickinson M H. The initiation and control of rapid flight maneuvers in fruit flies[J]. Integrative and comparative biology, 2005, 45(2): 274-281. DOI: https://doi.org/10.1093/icb/45.2.274.

[103] Kolomenskiy D, Maeda M, Engels T, et al. Aerodynamic ground effect in fruitfly sized insect takeoff[J]. PLoS one, 2016, 11(3): e0152072.

[104] Bode-Oke A T, Zeyghami S, Dong H. Flying in reverse: kinematics and aerodynamics of a dragonfly in backward free flight[J]. Journal of The Royal Society Interface, 2018, 15(143): 20180102.

[105] Wakeling J, Ellington C. Dragonfly flight. II. Velocities, accelerations and kinematics of flapping flight.[J]. Journal of experimental biology, 1997, 200(3): 557-582.

[106] Oh S, Lee B, Park H, et al. A numerical and theoretical study of the aerodynamic performance of a hovering rhinoceros beetle (Trypoxylus dichotomus)[J]. Journal of Fluid Mechanics, 2020, 885.

[107] Nguyen Q V, Park H C, Goo N S, et al. Characteristics of a beetle's free flight and a flapping-wing system that mimics beetle flight[J]. Journal of Bionic Engineering, 2010, 7(1): 77-86.

[108] Le T Q, Van Truong T, Tran H T, et al. How could beetle ' s elytra support their own weight during forward flight?[J]. Journal of Bionic Engineering, 2014, 11(4): 529-540.

[109] Sitorus P E, Park H C, Byun D, et al. The role of elytra in beetle flight: I. Generation of quasi-static aerodynamic forces[J]. Journal of Bionic Engineering, 2010, 7(4): 354-363.

[110] Van Truong T, Le T Q, Park H C, et al. Non-jumping take off performance in beetle flight (rhinoceros beetle Trypoxylus dichotomus)[J]. Journal of Bionic Engineering, 2014, 11(1): 61-71.

[111] Boiteau G. Flight takeoff behavior of Colorado potato beetle[J]. The Canadian Entomologist, 2002, 134(2): 229-240.

[112] Cheng B, Deng X, Hedrick T L. The mechanics and control of pitching manoeuvres in a freely flying hawkmoth (Manduca sexta)[J]. Journal of Experimental Biology, 2011, 214(24): 4092-4106.

[113] Muijres F T, Elzinga M J, Iwasaki N A, et al. Body saccades of Drosophila consist of stereotyped banked turns[J]. Journal of Experimental Biology, 2015, 218(6): 864-875. DOI: http://dx.doi.org/10.1242/jeb.114280.

[114] Emlen J T. Flocking behavior in birds[J]. The Auk, 1952, 69(2): 160-170.

[115] Antoniou P, Pitsillides A, Engelbrecht A, et al. Mimicking the bird flocking behavior for controlling congestion in sensor networks[C]. in: 2010 3rd International Symposium on Applied Sciences in Biomedical and Communication Technologies (ISABEL 2010). 2010: 1-7.